

# Magnetolectric composite ceramics of barium titanate and cobalt-iron compounds

Dissertation

zur Erlangung des Doktorgrades  
der Naturwissenschaften (Dr. rer. nat.)

der

Naturwissenschaftlichen Fakultät II  
Chemie, Physik und Mathematik

der Martin-Luther-Universität  
Halle-Wittenberg,

vorgelegt von

M.Sc. Till Walther  
geboren am 23. Februar 1986 in Stendal

Erstgutachter: Prof. Dr. Stefan Ebbinghaus (Halle)  
Zweitgutachter: Prof. Dr. Holger Kohlmann (Leipzig)

Datum der Verteidigung: 06. Juni 2018

# Contents

1. Introduction .....	1
2. Theory .....	4
2.1. Barium titanate .....	4
2.2. Ferrite spinels .....	4
2.3. Composites of barium titanate and ferrite spinels .....	7
2.4. Measuring the magnetoelectric effect .....	8
3. Experimental part .....	11
3.1. Preparations .....	11
3.1.1. Mixed oxide method for ferrite spinels .....	12
3.1.2. Polyol method for ferrite spinels .....	12
3.1.3. Preparation of palmitic acid capped ferrite spinels .....	13
3.2. Characterizations .....	13
3.2.1. X-ray diffraction.....	13
3.2.2. Thermogravimetric analyses .....	13
3.2.3. Electron microscopy.....	13
3.2.4. Magnetic properties.....	13
3.2.5. Direct magnetoelectric voltage coefficient $\alpha_{ME}$ .....	14
3.2.6. Calibration of the $H_{AC}$ field for magnetoelectric measurements.....	16
4. Results and discussion.....	19
4.1. Ferrite spinels prepared by mixed oxide method .....	19
4.2. Ferrite spinels prepared by polyol mediated synthesis.....	22
4.2.1. Introduction to polyol synthesis .....	22
4.2.2. Characterization of the polyol prepared ferrite spinel powders .....	22
4.2.3. Magnetic properties of polyol prepared ferrite spinel powders .....	27
4.3. Functionalized cobalt and nickel ferrite spinels.....	33
4.3.1. Surface modification of nanoparticles.....	33

4.3.2. Characterization of the palmitic acid capped cobalt and nickel ferrites.....	33
4.3.3. Catalytic properties in the oxygen evolution and reduction reaction.....	37
4.4. Composites of $\text{CoFe}_2\text{O}_4$ and $\text{BaTiO}_3$ with 2-2 connectivity .....	39
4.5. Composites of $\text{CoFe}_2\text{O}_4$ and $\text{BaTiO}_3$ with 0-3 connectivity .....	41
4.6. Composites of $\text{Co}_{1/3}\text{Fe}_{2/3}$ and $\text{BaTiO}_3$ with 0-3 connectivity .....	44
5. Summary .....	46
6. References .....	47
Appendix .....	52
<b>A1</b> $\text{BaTiO}_3\text{-CoFe}_2\text{O}_4\text{-BaTiO}_3$ trilayer composite thin films prepared by chemical solution deposition .....	53
<b>A2</b> Hysteretic magnetoelectric behavior of $\text{CoFe}_2\text{O}_4\text{-BaTiO}_3$ composites prepared by reductive sintering and reoxidation .....	61
<b>A3</b> Novel magnetoelectric composites of cobalt iron alloy and barium titanate.....	70
List of publications.....	77
Articles in peer reviewed journals.....	77
Reports .....	78
Posters .....	79
Danksagung.....	80
Lebenslauf .....	81
Erklärung an Eides statt.....	82

## 1. Introduction

A material possessing at least two ferroic order phenomena like ferroelectricity, ferromagnetism and ferroelasticity is called multiferroic. A coupling between these orders leads to fascinating possibilities. Most interestingly is to directly influence either the magnetization  $M$  by application of an electric field  $E$  and/or the electric polarization  $P$  by a magnetic field  $H$ . This specific phenomenon is called the magnetoelectric effect and accordingly, these kind of materials are denoted as magnetoelectrics. A prominent depiction of the relations between ferroic orders is shown in Figure 1. The coexistence of polarization and magnetization promises innovative concepts for devices like transducers, actuators or advanced storage media.[1]

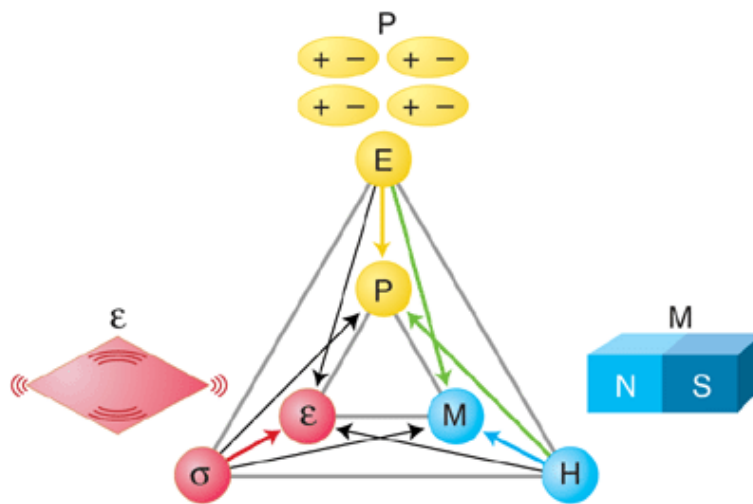


Figure 1: Scheme of multiferroic interactions between ferroelectricity, ferromagnetism and ferroelasticity.[2]

Historically, the research on multiferroics started with single phase materials, i.e. compounds that exhibit two or more ferroic order phenomena in the same phase. Unfortunately, there are only few compounds with useful electric and magnetic properties especially close to room temperature. One reason for this is that the cations of typical ferroelectrics possess empty or completely filled  $d$  orbitals while magnetic ordering requires unpaired electrons in these orbitals. Additionally, the observed magnetoelectric couplings in single phase materials are very weak.[3]

A variety of mechanisms for the occurrence of magnetoelectricity are known. In  $\text{BiFeO}_3$  for example, a single phase magnetoelectric with perovskite structure, ferroelectricity and magnetism originate from different metal ions. The magnetic properties arise from the 3d-electrons of the  $\text{Fe}^{3+}$  ions and the ferroelectric properties from the lone 6s electron pair of the  $\text{Bi}^{3+}$  ions. Unfortunately, the coupling between the two ferroic properties is quite weak. Another

possibility to generate magnetoelectricity in single phase materials is to induce a polarization by strain in a material that possesses suitable magnetic properties.[4] A detailed review for single phase magnetoelectric mechanisms and materials was published by Dong et al. [5].

To overcome the rareness and shortcomings of single phase magnetoelectrics, the first magnetoelectric composite was introduced in the 1970s by Van den Boomgaard et al. and Van Run et al. in two publications.[6,7] They described the quinary system Fe-Co-Ba-Ti-O that, when solidified in the eutectic composition, forms the two phases  $\text{CoFe}_2\text{O}_4$  and  $\text{BaTiO}_3$ . The combination of these two compounds results in a composite with superior magnetoelectric properties.  $\text{CoFe}_2\text{O}_4$  is a hard ferrimagnetic ferrite spinel and  $\text{BaTiO}_3$  is a well-known ferroelectric perovskite. Both, the ferrimagnetic and ferroelectric Curie temperatures of the two oxides, are well above room temperature. Hence, this system attracted a lot of research interest over the last decades, especially in the last ten years. Until today, many more compounds were found to be suitable for magnetoelectric composites but still most of them consist of ferrite spinels combined with perovskites.[8]

In magnetoelectric composites the maximization of the coupling between the two ferroic orders is always one of the main challenges to obtain a high magnetoelectric effect. Based on the concepts of Newnham et al.[9], several connectivities between the two phases have been investigated. The majority of the reported composites possess 0-3 and 2-2 connectivities, meaning either separated particles in a matrix or alternately layered structures.[10] A scheme of these two connectivities is depicted in Figure 2.

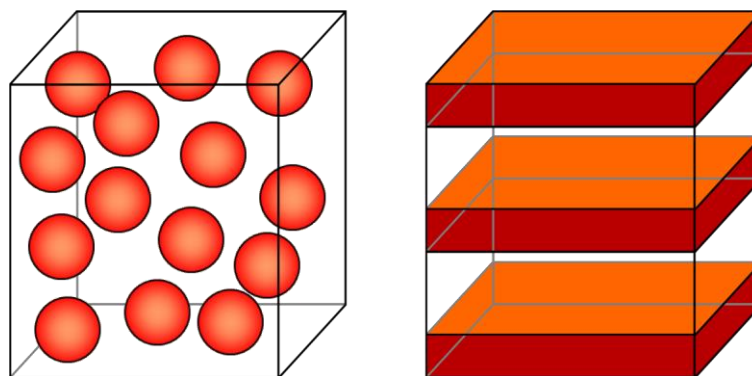


Figure 2: Mainly investigated connectivities for magnetoelectric composites.

Left: 0-3; right 2-2.

Although the  $\text{CoFe}_2\text{O}_4 - \text{BaTiO}_3$  system has been under investigation since four decades, the theoretically predicted high magnetoelectric coefficients of several  $\text{V Oe}^{-1} \text{cm}^{-1}$  [11] have not yet been achieved experimentally. The reported  $\alpha_{\text{ME}}$  values range from a few  $\mu\text{V Oe}^{-1} \text{cm}^{-1}$  to several  $\text{mV Oe}^{-1} \text{cm}^{-1}$ . [1,8,12] Usually, this discrepancy is explained by an insufficient interface that can be caused by chemical reactions, lattice mismatches and thermally induced stress because of high sintering temperatures. Additionally, using high fractions of the magnetic phase leads to leakage currents as the resistivity of the magnetic material usually is rather low. Hence, electric poling of such composites is difficult. [13]

The aim of the present work was to prepare nanoparticles of ferrite spinels and barium titanate by soft chemistry methods. The usefulness of the obtained powders as educts for sintered magnetoelectric composites and the resulting magnetoelectric properties were to be investigated. The obtained composites have been investigated and characterized by various methods in order to clarify their structural, morphological, dielectrical, magnetic and magnetoelectric properties.

## 2. Theory

### 2.1. Barium titanate

Barium titanate ( $\text{BaTiO}_3$ ) crystallizes in the perovskite structure. In the cubic modification the  $\text{Ba}^{2+}$  ions are located on the corners, the  $\text{Ti}^{4+}$  ions in the center and the  $\text{O}^{2-}$  ions in the middle of the faces of a cube. The oxygen ions build an octahedron around the titan ions and a cuboctahedron around the barium ions. In its cubic modification  $\text{BaTiO}_3$  is a pyroelectric material. This modification is stable above the transition temperature  $T_C = 125\text{ }^\circ\text{C}$ . Upon cooling below this Curie temperature, the material undergoes a transition into the tetragonal phase. In this modification the c-axis is slightly elongated and the  $\text{Ti}^{4+}$  position is shifted along the c-axis off-center. So are the oxygen atoms, which are shifted in the opposite direction as depicted in Figure 3. Because of this shift, the tetragonal phase is polarizable and switchable in an electric field. This leads to extraordinary dielectric, ferroelectric and piezoelectric properties. Barium titanate is therefore used e.g. as capacitor and energy storage devices. Upon doping,  $\text{BaTiO}_3$  can also be used as semiconductor, thermistors and in piezoelectric devices.[14,15]

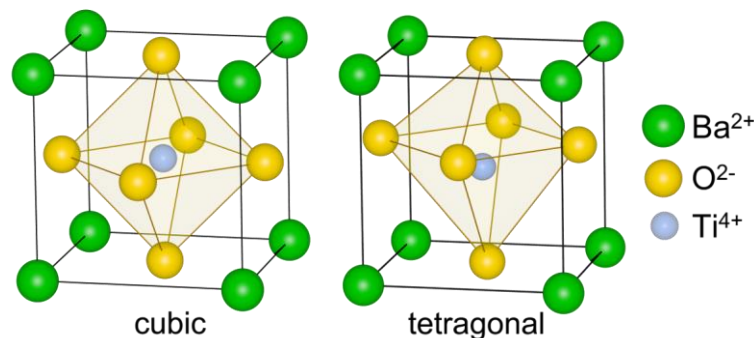


Figure 3: Unit cells of  $\text{BaTiO}_3$  in the cubic and tetragonal modification. The tetragonal distortion is exaggerated.

### 2.2. Ferrite spinels

Ferrite spinels possess the formula  $\text{MFe}_2\text{O}_4$  with M being a bivalent metal cation, often of the 3d series.

In the spinel structure, oxygen atoms form a face centered cubic (fcc) lattice with tetrahedral and octahedral sites. In a normal spinel, like  $\text{MgAl}_2\text{O}_4$ , one quarter of the tetrahedral sites is occupied by the bivalent metal ions and half of the octahedral sites are occupied by the trivalent metal ions, as shown in Figure 4. In inverse spinels the bivalent metal ions are positioned on octahedral sites and half of the trivalent metal ions take tetrahedral positions.[16] An example for an inverse ferrite spinel is nickel ferrite,  $\text{NiFe}_2\text{O}_4$ .

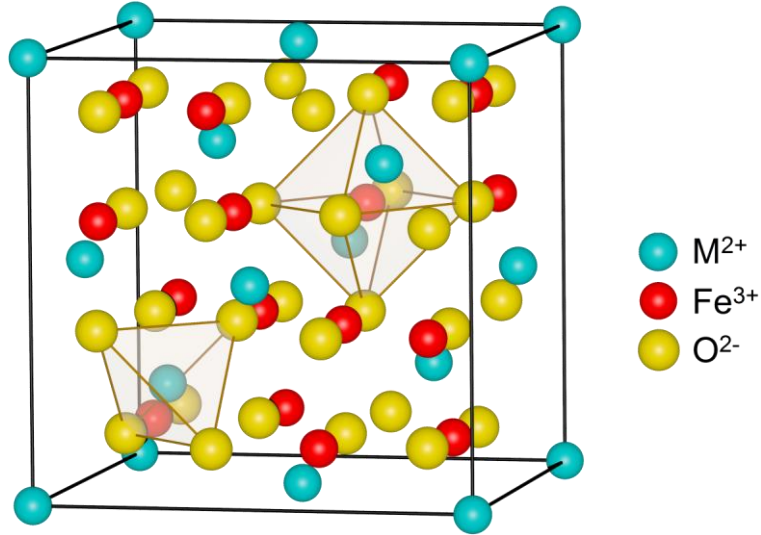
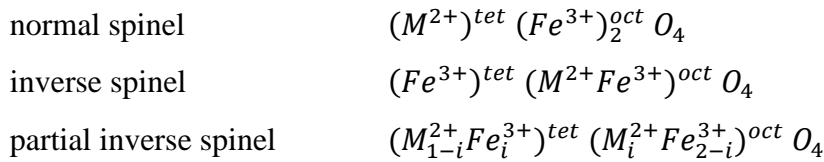


Figure 4: Unit cell of a normal ferrite spinel.

Many ferrite spinels crystallize in a partially inverse structure. To describe the degree of cationic ordering, the inversion parameter  $i$  can be used with  $i = 0$  for normal spinels and  $i = 1$  for complete inverse spinels. The general formulas for normal, inverse and partial inverse ferrite spinels are as follows:



The inversion parameter depends on the chemical composition and often also on the preparation conditions of the spinel. For example, in  $CoFe_2O_4$  the inversion parameter  $i$  can vary from 0.7 – 0.8.[17] An overview of typical inversion parameters of the ferrite spinels prepared in this work is listed in Table 1.

Because of the high spin configuration of the  $d^5$   $Fe^{3+}$  ions, ferrite spinels possess at least one kind of paramagnetic ions. Depending on the electron configuration of the  $M^{2+}$  ion, an additional paramagnetic species can be present. Octahedral and tetrahedral sites form two distinct magnetic sublattices. The paramagnetic ions of the two sublattices couple antiferromagnetic resulting in a ferromagnetic coupling within both sublattices. Thus, a net magnetization can result, whose strength is dependent on the occupancy of the lattice sites by  $M^{2+}$  and  $Fe^{3+}$  ions as well as the electronic configuration of the  $M^{2+}$  ions.[16]

Exceptions from this normal magnetic structure can occur if the ions on the tetrahedral sites are diamagnetic. Normally,  $M_{tet}-O-M_{oct}$  superexchanges between the tetrahedral and octahedral



coordinated ions lead to the antiferromagnetic coupling between the two sublattices. If the tetrahedral lattice is occupied by diamagnetic ions,  $M_{oct}-O-O-M_{oct}$  super-superexchanges between the paramagnetic ions in the octahedral sites can become dominant and may lead to an antiferromagnetic coupling in the octahedral lattice.[18] This explains why the normal spinel ( $i \approx 0$ )  $ZnFe_2O_4$  possesses a saturation magnetization close to zero.  $MgFe_2O_4$ , although it contains the diamagnetic  $Mg^{2+}$  ion, fits into the normal magnetic model, because it is partially inverse ( $i = 0.7 - 0.9$ ) and the tetrahedral sites are predominantly occupied by  $Fe^{3+}$  ions. Hence, the  $Fe^{3+}_{tet}-O-Fe^{3+}_{oct}$  superexchange stabilizes the antiferromagnetic coupling between the tetrahedral and octahedral sublattices.

The theoretical saturation magnetization of ferrite spinels can be calculated with the spin-only approach. For an ion the theoretical magnetization is:

$$\mu_{ion} = g \cdot S \cdot \mu_B \quad [19]$$

with the Landé factor  $g$ , the spin  $S$  and the Bohr magneton  $\mu_B$ . With  $g = 2$  for electrons and  $n$  being the amount of unpaired electrons in the ion, the formula reduces to

$$\mu_{ion} = n \cdot \mu_B$$

In a ferrite spinel, the net magnetization is the difference between the magnetization of the octahedral and the tetrahedral sublattice:

$$\mu_{theor} = \mu_{oct} - \mu_{tet}$$

Taking the inversion parameter into consideration, and  $n_{Fe^{3+}} = 5$ , the final formula is given as:

$$\mu_{theor} = \{[i \cdot n_{M^{2+}} + 5(2 - i)]_{oct} - [(1 - i) \cdot n_{M^{2+}} + 5i]_{tet}\} \cdot \mu_B$$

In the case of an almost normal ferrite spinel ( $i \leq 0.3$ ) with diamagnetic  $M^{2+}$  ions, e.g.  $ZnFe_2O_4$ , the formula changes, because of the different coupling of the sublattices as explained above. In this case, only the magnetization of the  $Fe^{3+}$  ions on the tetrahedral sites have to be considered due to the antiferromagnetic coupling of the  $Fe^{3+}$  ions on the octahedral sites.

$$\mu_{theor} = n_{Fe^{3+}_{tet}} \cdot \mu_B = i \cdot n_{Fe^{3+}} \cdot \mu_B = i \cdot 5\mu_B$$

One has to keep in mind that the theoretical  $\mu_{theor}$  values are only an estimation that works best for single crystals at 0 K. The experimentally determined values can differ distinctly, especially when the particles are very small and additional effects, such as superparamagnetism, occur.

Calculated  $\mu_{theor}$  values for the used ferrite spinels are listed in Table 1.

Table 1: Ferrite spinels used in this work with inversion parameters with  $M_S$  values taken from literature and corresponding calculated theoretical saturation magnetizations.

Compound	Inversion Parameter	$M_S \mu_{\text{theor}}$	$M_S$ from literature
CoFe <sub>2</sub> O <sub>4</sub>	0.7 – 0.8 [17]	3.8 – 4.2 $\mu_B$	3.5 $\mu_B$ [20]
NiFe <sub>2</sub> O <sub>4</sub>	1.0 [21,22]	2 $\mu_B$	2.6 $\mu_B$ [20]
MnFe <sub>2</sub> O <sub>4</sub>	0.2 – 0.6 [22–25]	5 $\mu_B$	4.1 $\mu_B$ [20]
MgFe <sub>2</sub> O <sub>4</sub>	0.7 – 0.9 [26]	1 – 3 $\mu_B$	1.4 – 1.6 $\mu_B$ [20,27]
ZnFe <sub>2</sub> O <sub>4</sub>	0.0 – 0.3 [28,29]	0 – 1.5 $\mu_B$	0 $\mu_B$ [20]
CuFe <sub>2</sub> O <sub>4</sub>	0.8 – 1.0 [22,30,31]	1 – 2.6 $\mu_B$	0.8 – 2.1 $\mu_B$ [32,33]

### 2.3. Composites of barium titanate and ferrite spinels

As mentioned in the introduction, the history of multiferroic and magnetoelectric BaTiO<sub>3</sub> – MFe<sub>2</sub>O<sub>4</sub> composites reaches back to the works of van Run et al. and van den Boomgaard et al. in the 1970s.[6,7,34–37] Since then, a multitude of studies concerning BaTiO<sub>3</sub> and ferrite spinels have been published. Over the time, a variety of systems were developed and investigated. For example there are many publications on 2-2 composites: BaTiO<sub>3</sub> in combination with CoFe<sub>2</sub>O<sub>4</sub> [38], NiFe<sub>2</sub>O<sub>4</sub> [39], Ni<sub>0.4</sub>Zn<sub>0.6</sub>Fe<sub>2</sub>O<sub>4</sub> [40], Fe<sub>3</sub>O<sub>4</sub> [41] and many more especially with other perovskites as ferroelectric phase[42]. A lot of work has also been done on 0-3 composites: BaTiO<sub>3</sub> mainly in combination with CoFe<sub>2</sub>O<sub>4</sub> [43–45] but also NiFe<sub>2</sub>O<sub>4</sub> [46,47] and some mixed ferrites, e.g. Co<sub>0.6</sub>Zn<sub>0.4</sub>Fe<sub>1.7</sub>Mn<sub>0.3</sub>O<sub>4</sub>, CuFe<sub>1.6</sub>Cr<sub>0.4</sub>O<sub>4</sub> and Ni<sub>0.7</sub>Zn<sub>0.3</sub>Fe<sub>2</sub>O<sub>4</sub> [48–50].

The magnetoelectric effect in BaTiO<sub>3</sub> – CoFe<sub>2</sub>O<sub>4</sub> composites is based on the strain mediated mechanism. When a magnetic field  $H$  is applied to the composites, the CoFe<sub>2</sub>O<sub>4</sub> particles change shape because of magnetostriction. The resulting strain  $\varepsilon$  induces a stress  $\sigma$  onto the BaTiO<sub>3</sub> particles. Because of their piezoelectric properties, an electrical polarization  $P$  results and in turn a voltage can be measured. The corresponding coefficient  $\alpha_{ME}^{H \rightarrow P}$  is called the direct magnetoelectric coefficient.

According to Nan et al., the direct magnetoelectric effect can be described as the product of the magnetostriction (piezomagnetic respectively magnetic-mechanical effect) in the ferromagnetic phase and the piezoelectric effect (mechanical-electrical effect) in the ferroelectric phase.[11]

$$\text{Magnetoelectric effect} = \frac{\text{magnetic}}{\text{mechanical}} \times \frac{\text{mechanical}}{\text{electrical}}$$

This mechanism also works in the opposite direction, i.e. when an electric field  $E$  is applied it induces strain  $\varepsilon$  in the piezoelectric phase, which then applies a stress  $\sigma$  on the magnetostrictive phase and yields a change in its magnetization  $M$ . In this case, the coefficient  $\alpha_{ME}^{E \rightarrow M}$  is called the converse magnetoelectric coefficient. In Figure 5, the pathway of such a coupling is shown schematically.

Thus, magnetostrictive and piezoelectric properties of the phases and their coupling through the interfaces are essential for the magnetoelectric effect in composites.

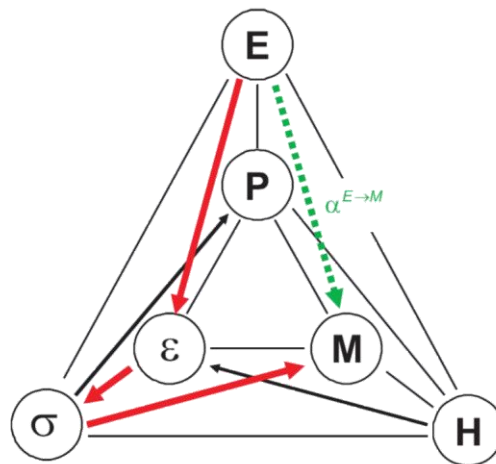


Figure 5: Schematic pathway (red) of the strain mediated coupling, yielding the converse magnetoelectric coefficient  $\alpha_{ME}^{E \rightarrow M}$  (green). Edited from [51].

#### 2.4. Measuring the magnetoelectric effect

A variety of experimental methods have been developed to measure the occurrence of magnetolectricity and to determine the different magnetoelectric coefficients. These techniques usually include the application of a magnetic or electric field combined with a measurement of polarization, voltage or magnetization, respectively. In principle, many detection systems can be used e.g. vibrating sample magnetometers (VSM), superconductive quantum interference devices (SQUID), determination of the magneto-optic Kerr effect (MOKE) and various force microscopy setups. A very good review about magnetoelectric measuring techniques was published by Lupascu et al.[51]

To measure the direct magnetoelectric coefficient, three methods are used typically.[52]

In a static method, the contacted sample is placed in a magnetic DC field. The magnetoelectric measurements are performed by measuring the accumulated voltage that develops across the sample as function of the applied magnetic field. For this method the samples have to be poled electrically and magnetically prior to the measurement.[53]

Another magnetoelectric measurement technique is the quasi-static method. In this approach, charge is recorded as a function of time at zero magnetic field, initially. Followed by a linear increase of the field to a given value, for example 20 kOe. The field is then kept constant for a specific time and subsequently, the field is decreased linearly to zero. Over the complete time the generated charge is measured. With this procedure the data can be corrected for natural drifts.[54]

In the dynamic method, the magnetoelectric voltage is measured with an applied magnetic AC field additional to the DC field.[55] With this method the values of AC ME voltage are measured in contrast to the static and quasi-static methods where the DC ME charges or voltages are measured. One advantage of the dynamic approach is the possibility to measure the phase shift of the signal and hence a separation of the measured voltage into magnetoelectric and induction parts is possible. Additionally, because the signal in this method has a defined frequency and can be measured by a lock-in technique, the noise is dramatically reduced.[56]

In this work, a custom made setup based on the AC transport (ACT) measuring option of a Quantum Design PPMS was used to determine the direct magnetoelectric voltage coefficient  $\alpha_{ME}$  ( $H \rightarrow P$ ). The setup is inspired by the dynamic measurement method [55,56]. It takes advantage of the built-in frequency generator and amplifying and detecting systems of the ACT option. Normally, the ACT option uses two pairs of contacts for a four point resistance setup, allowing different types of electrical transport measurements. The current connections pass a known current through the sample and the voltage connections are used to measure the occurring voltage drop. The current source is used as reference signal for the amplifier of the measuring voltage signal. This is called a lock-in amplifying system.

For our magnetoelectric measurements, the current source of the ACT option is used to pass a known AC current through a solenoid that is mounted on the sample holder and thus applies a defined alternating magnetic field  $H_{AC}$  on the sample. A picture of the sample holder is shown in Figure 6. The voltage detector of the ACT option is connected to the sample and the magnetoelectrical induced voltage is measured. The lock-in amplifier allows the determination of in-phase and out-of-phase parts of the measured voltage and thus, a differentiation between ME-voltage ( $U_{ME}$ , in-phase with  $H_{AC}$ ) and electromagnetically induced voltage ( $90^\circ$  phase shift) is possible.  $\alpha_{ME}$  can be calculated as  $\alpha_{ME} = U_{ME}/H_{AC} \cdot h$  with  $h$  being the sample height. A magnetic DC field can be applied by the superconducting electromagnet of the PPMS and the temperature can be varied from 2K to 400K. A scheme of the setup is shown in Figure 7.

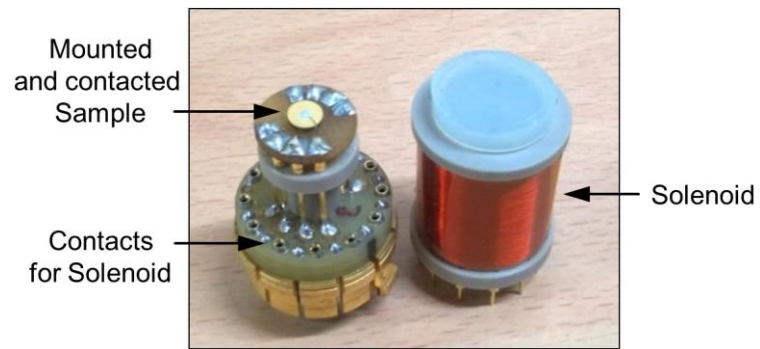


Figure 6: Picture of the sample holder for magnetolectric measurements.

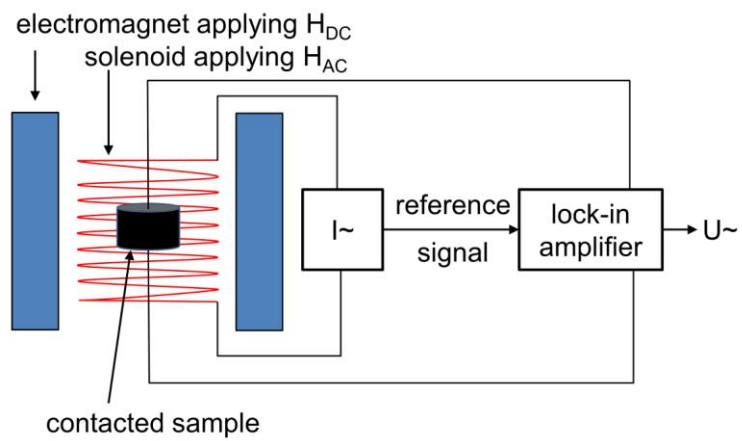


Figure 7: Scheme of the magnetolectric measurement setup.

### 3. Experimental part

In the following chapters, mainly unpublished results are described. Additional preparations and characterizations were published in the according articles, see chapters 4.4. – 4.6. and appendix: A1[57], A2[58] and A3[59].

#### 3.1. Preparations

The chemicals that were used for the described preparations are listed in Table 2.

Table 2: Used chemicals.

Compound	Company	Purity
Fe <sub>2</sub> O <sub>3</sub>	Sigma Aldrich	≥99%
Co <sub>3</sub> O <sub>4</sub>	Alfa Aesar	99.7%
MgO	Sigma Aldrich	≥99%
NiO	Alfa Aesar	78.5% Ni
MnCO <sub>3</sub>	VEB Laborchemie Apolda	p.a.
CuO	VEB Berlin Chemie	p.a.
ZnO	VEB Laborchemie Apolda	p.a.
Fe(NO <sub>3</sub> ) <sub>3</sub> ·9H <sub>2</sub> O	Sigma Aldrich	≥98%
Co(NO <sub>3</sub> ) <sub>2</sub> ·6H <sub>2</sub> O	Carl Roth	≥98%
Ni(NO <sub>3</sub> ) <sub>2</sub> ·6H <sub>2</sub> O	VEB Laborchemie Apolda	p.a.
Cu(NO <sub>3</sub> ) <sub>2</sub> ·2.5H <sub>2</sub> O	Alfa Aesar	≥98%
Mg(NO <sub>3</sub> ) <sub>2</sub> ·6H <sub>2</sub> O	Alfa Aesar	≥98%
Mn(NO <sub>3</sub> ) <sub>2</sub> ·4H <sub>2</sub> O	Sigma Aldrich	≥97%
Zn(NO <sub>3</sub> ) <sub>2</sub> ·6H <sub>2</sub> O	Acros	98%
Ba(OH) <sub>2</sub> ·8H <sub>2</sub> O	Fluka	p.a.
titanium isopropoxide	Alfa Aesar	≥97%
diethylene glycol	Carl Roth	≥99%
palmitic acid	VEB Laborchemie Apolda	purum
NaOH	Grüssing	99%

### 3.1.1. Mixed oxide method for ferrite spinels

The classical solid state method was used to prepare the following ferrite spinels:



To synthesize the ferrite spinels, stoichiometric amounts of the corresponding starting material for  $M^{2+}$  were mixed with  $Fe_2O_3$  (10 mmol) in isopropyl alcohol and ground in an agate mortar until an optically homogeneous paste formed. The mixture was dried in air and transferred into an aluminum oxide crucible. Calcination for 24 h at an elevated temperature led to the formation of the desired ferrite spinel. The used starting materials and calcination conditions for the different compounds are listed in Table 3.

Table 3: Calcination conditions and starting materials for ferrite spinels prepared by mixed oxide method.

<b>Compound</b>	<b>Starting material <math>M^{2+}</math></b>	<b>Calcination temperature</b>	<b>Remarks</b>
$CoFe_2O_4$	$Co_3O_4$	1100 °C	
$NiFe_2O_4$	NiO	1100 °C	
$MnFe_2O_4$	$MnCO_3$	1250 °C	calcined under $N_2$
$MgFe_2O_4$	MgO	1250 °C	
$ZnFe_2O_4$	ZnO	1000 °C	
$CuFe_2O_4$	CuO	900 °C, 72 h	CuO impurities

### 3.1.2. Polyol method for ferrite spinels

The different ferrite spinel powders of  $MFe_2O_4$ , with  $M = \text{Co, Ni, Mn, Mg, Zn}$  and  $\text{Cu}$ , were synthesized using the same route for all samples as described in the following.

$Fe(NO_3)_3 \cdot 9H_2O$  (20 mmol) and the corresponding metal nitrate  $M(NO_3)_2 \cdot xH_2O$  (10 mmol) were dissolved in deionized water (6 ml). Diethylene glycol (250 ml) and NaOH (80 mmol) were added to the solution and the apparatus was flushed with argon. The mixture was heated to the boiling point (~160 °C) and kept under reflux for one hour. Eventually, brown gases ( $NO_x$ ) evolved from the reaction mixture. After cooling to room temperature, acetone (250 ml) was added and the precipitate was centrifuged, washed with acetone three times and dried at air.

### 3.1.3. Preparation of palmitic acid capped ferrite spinels

A series of  $\text{Co}_x\text{Ni}_{(1-x)}\text{Fe}_2\text{O}_4$  ferrites with  $x = 1$  to  $0$  ( $\Delta x = 0.1$ ) capped with palmitic acid was prepared as follows.

$\text{Fe}(\text{NO}_3)_3 \cdot 9\text{H}_2\text{O}$  (20 mmol) and the respective amounts of  $\text{Co}(\text{NO}_3)_2 \cdot 6\text{H}_2\text{O}$  and  $\text{Ni}(\text{NO}_3)_2 \cdot 6\text{H}_2\text{O}$  (10 mmol in total) were dissolved in deionized water (6 ml). Diethylene glycol (250 ml) and NaOH (80 mmol) were added to the solution and the apparatus was flushed with argon. The mixture was heated to the boiling point ( $\sim 160$  °C) and kept under reflux for an hour. Eventually, brown gases evolve from the reaction mixture. After the mixture stopped boiling, palmitic acid (20 mmol) was added under vigorous stirring while the mixture was still hot. The flask was then allowed to cool to room temperature. A gel formed and was dissolved by the addition of isopropyl alcohol (250 ml). The product was filtered off and washed three times each with isopropyl alcohol and water. The samples were obtained as brown fluffy powders.

## **3.2. Characterizations**

### 3.2.1. X-ray diffraction

X-ray diffraction patterns were recorded at room temperature on a Bruker D8 Advance diffractometer operating with  $\text{CuK}\alpha$  radiation.

### 3.2.2. Thermogravimetric analyses

Thermogravimetric measurements in flowing synthetic air or forming gas (10%  $\text{H}_2$ ) (flow rate  $40 \text{ ml min}^{-1}$ , heat rate  $10 \text{ K min}^{-1}$ ) were performed using a Netzsch STA 409 system.

### 3.2.3. Electron microscopy

Scanning electron microscopy images in the backscattered electron (BSE) mode and EDX spectra were recorded using a Philips ESEM XL 30 FEG and a Phenom-World B.V. Phenom ProX.

Transmission electron microscopy images were recorded with a Philips CM20Twin.

### 3.2.4. Magnetic properties

All magnetic measurements were carried out using the ACMS option of a Quantum Design PPMS 9.



For field dependent magnetic properties, hysteresis loops were measured at 300 K and 10 K while cycling the magnetic field  $H_{DC}$  between +90 and -90 kOe.

For the determination of the saturation magnetization values  $M_S$ , linear fittings of the magnetizations from the ranges of +50 to +90 kOe and -50 to -90 kOe were performed. The mean of the absolute values of both intercepts was taken as  $M_S$ .

Remanent magnetization values  $M_R$  were determined by taking the mean of the absolute values of the positive and negative magnetization  $M$  at  $H = 0$  Oe.

Coercivities  $H_C$  were determined by taking the mean of the absolute values of  $H$  at  $M = 0$  Oe.

To measure the temperature dependent magnetic properties, at first, the samples were cooled down to 10 K under zero field conditions ( $H_{DC} = 0$  Oe). The samples were then heated up to 300 K with an applied field of  $H_{DC} = 100$  Oe (zero field cooled, ZFC) followed by cooling down under the same field (field cooled, FC). The magnetization  $M$  of the samples was measured during ZFC and FC. The blocking temperature  $T_B$  is the temperature  $T$  at the maximum value of the magnetization  $M$  of the ZFC curve.

### 3.2.5. Direct magnetoelectric voltage coefficient $\alpha_{ME}$

The direct magnetoelectric voltage coefficient  $\alpha_{ME}$  was measured with the setup described on page 8pp. Prior to the measurements, the samples were sputtered with 100 nm thick gold electrodes using a Cressington Sputter Coater 108 auto. The contacted samples were poled electrically with a Heinzinger DC high voltage power supply LNC 1200-50pos at electrical fields of  $4 \text{ kV cm}^{-1}$  with a current limited to 0.1 mA. The electric field was applied at ambient temperature and the sample was heated above the Curie Temperature of  $\text{BaTiO}_3$  to  $200^\circ\text{C}$  and kept at this temperature for 1 h. Afterwards the sample was allowed to cool down to ambient temperature with an applied electric field in order to maximize the polarization of the composites. Directly before the magnetoelectric measurement, the samples were short circuited for 10 minutes to deplete any accumulated charges. Afterwards, the samples were glued to the contacts of the sample holder with conductive silver epoxy EPO-TEK H20E.

During the measurements, the magnetic DC field was raised from 0 Oe to 10 kOe, decreased to -10 kOe and again increased to 10 kOe. Between 1 and -1 kOe, measuring points were taken every 100 Oe. This interval was increased to 200 Oe from 1 to 10 kOe and -1 to -10 kOe.

At every measuring point, the AC field ( $I = 20 \text{ mA}$ ;  $H_{AC} \approx 10 \text{ Oe}$ ) was applied with five different frequencies (107, 307, 507, 707 and 907 Hz) and the magnetoelectric voltage was measured for five seconds, each.

A typical dataset of a magnetoelectric measurement, as depicted by the MultiVu PPMS software, is shown in Figure 8. As mentioned before, the in-phase and 90° out-of-phase voltages are measured. Unfortunately, only the in-phase part of the voltage is stored directly. The 90° phase shifted part can be extracted from a value that is called the Drive Signal. The Drive Signal is described as the total magnitude of the sample response and is the square root of the sum of the squares of in-phase and out-of-phase voltage.[60]

$$Drive\ Signal = \sqrt{(U_{in-phase})^2 + (U_{out-of-phase})^2}$$

It should be noted that the measured out-of-phase voltage is not constant with  $H_{DC}$  and does not increase linearly with the frequency of  $H_{AC}$ , as would be expected for an induced electromotive force. The origin of this effect is yet unknown.

$$U_{out-of-phase} = -\mu_r(S\cos\theta)\omega\Delta H_{AC}\sin(\omega t + \frac{\pi}{2}) [13]$$

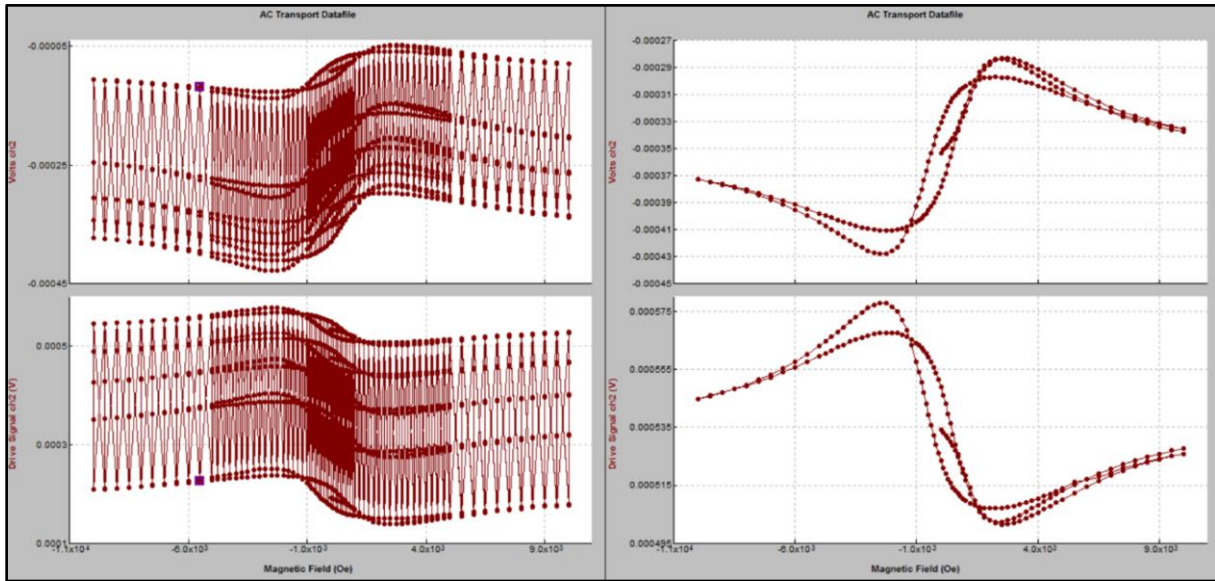


Figure 8: Raw data of a magnetoelectric measurement in the PPMS software MultiVu.

Left: all  $H_{AC}$  frequencies, right: data for  $f = 907$  Hz.

Upper diagrams:  $U_{in-phase}$ . Lower diagrams: Drive Signal.

The raw data were evaluated using OriginPro 8G. It turned out that even for an empty sample holder a small and frequency dependent bias voltage was measured, leading to a shift of the  $U-H_{DC}$  curves as can be seen in Figure 8. The raw data therefore had to be corrected for this voltage shift. Although the general trend of the bias voltage was identical for all measurements, its exact value varied for the individual samples, i.e. a simple addition of the values of a blank

measurement was not sufficient as correction. For this reason the average of the voltage values measured at 10 and -10 kOe were chosen as voltage offset and subtracted from the original data as shown in Figure 9.

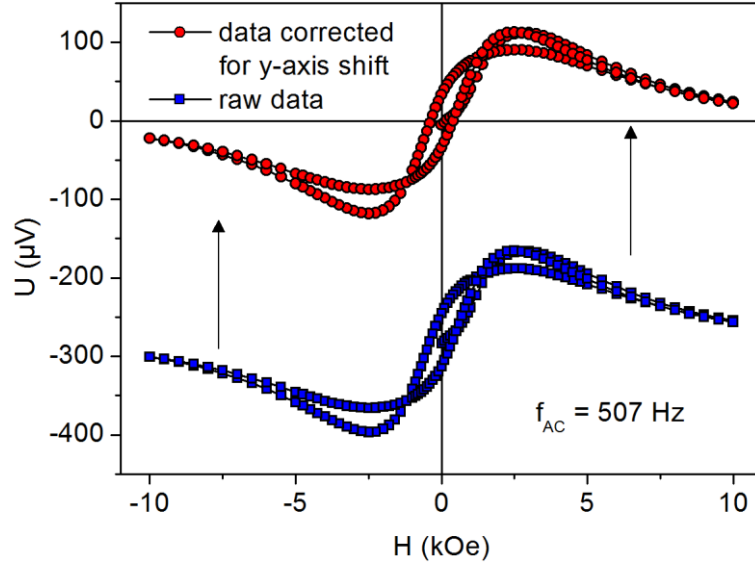


Figure 9: Blue squares: raw magnetolectric measurement dataset, red circles: data corrected for the systematical voltage shift.

With the sample height  $h$  and the applied AC field  $H_{AC}$ , the magnetolectric coefficient  $\alpha_{ME}$  can be calculated from the measured magnetolectric voltage  $U_{ME}$  as follows:

$$\alpha_{ME} = \frac{\Delta E}{\Delta H} = \frac{U_{ME}}{h \cdot H_{AC}}$$

### 3.2.6. Calibration of the $H_{AC}$ field for magnetolectric measurements.

As described earlier, the  $H_{AC}$  field was applied via a custom made solenoid using the AC-Transport option of the PPMS. Because only the current can be set with the ACT option, the  $H_{AC}$  field had to be determined and calibrated with additional equipment.

For the first calibration method an AC hall sensor was installed on the sample holder. In this way, the sensor took the exact position of a sample in a ME measurement. The sensor was calibrated, so that a measured voltage across the sensor could be transferred in a  $H_{AC}$  field with the following formula.

$$H_{AC} = \frac{10 \text{ Oe}}{25 \text{ mV}} \cdot U_{in-phase}$$

For the measurements, an external voltage of 5 V had to be applied to the AC hall sensor. For this reason the electronics of the PPMS ACT option could not be used but the current was provided by an external source and the voltage was measured with an oscilloscope.

Measurements with the sample holder connected to an external test box and mounted inside the PPMS showed that the supply cables inside the PPMS have a remarkable frequency-dependent effect. The determined  $H_{AC}$  fields for different currents and frequencies are listed in Table 4.

Table 4: Calibrated magnetic AC fields for different currents and frequencies.

<b>I in mA</b>	<b><math>f_{AC}</math> in Hz</b>	<b><math>H_{AC}</math> in Oe</b>	<b><math>H_{AC}/I</math> in Oe mA<sup>-1</sup></b>
5	107	2.1	0.42
5	307	1.8	0.36
5	507	1.6	0.32
5	707	1.5	0.30
5	907	1.4	0.28
10	107	4.5	0.45
10	307	4.4	0.44
10	507	4.1	0.41
10	707	3.9	0.39
10	907	3.7	0.37
20	107	9.2	0.46
20	307	8.8	0.44
20	507	8.2	0.41
20	707	7.9	0.40
20	907	7.6	0.38

For a second calibration method of the  $H_{AC}$  field, an induction coil was wound manually from copper wire and contacted to the sample holder. Different driving currents, and thus  $H_{AC}$  fields, were applied in the PPMS and the induced voltage was measured with the AC-Transport option. From these voltages, the  $H_{AC}$  fields were calculated. In Figure 10, the obtained values divided by the corresponding currents are shown. As can be seen, the determined values are in the same range as the ones from the Hall sensor and also the frequency dependency is similar.

As a conclusion, the  $H_{AC}$  field was calibrated with two independent methods and similar results were obtained.

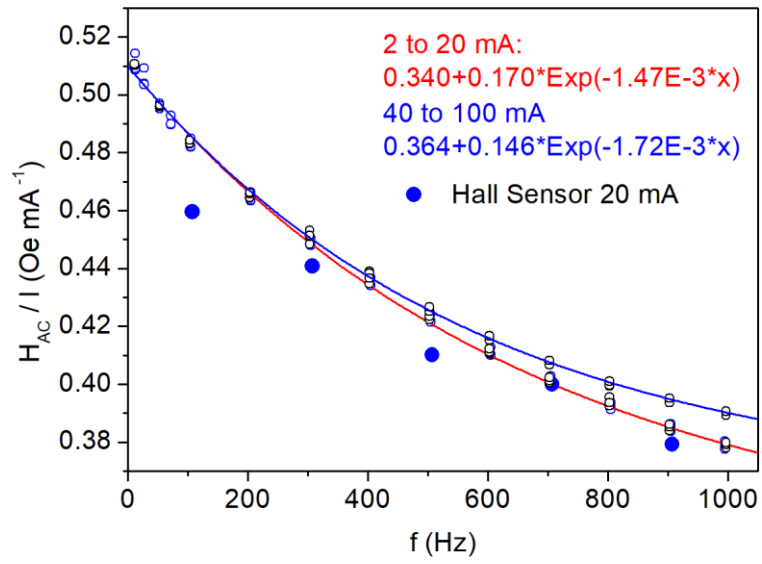


Figure 10: Magnetic AC field per mA driving current obtained from a Hall sensor (blue solid symbols) and from an induction coil (open symbols).

## 4. Results and discussion

### 4.1. Ferrite spinels prepared by mixed oxide method

As can be seen in Figure 11, the mixed oxide synthesis leads to phase pure ferrite spinels  $MFe_2O_4$  in the case of  $M = Co, Ni, Mn, Mg$  or  $Zn$ . However, because of its redox properties, the manganese ferrite spinel had to be synthesized under a protecting atmosphere of  $N_2$ .

For two reasons  $CuFe_2O_4$  stands out. On the one hand the five other ferrite spinels crystallize in the cubic space group  $Fd-3m$  while the modification stable at room temperature of  $CuFe_2O_4$  is the tetragonal  $I4_1/amd$ . [31] On the other hand, all prepared samples of  $CuFe_2O_4$  contained at least trace amounts of  $CuO$ .

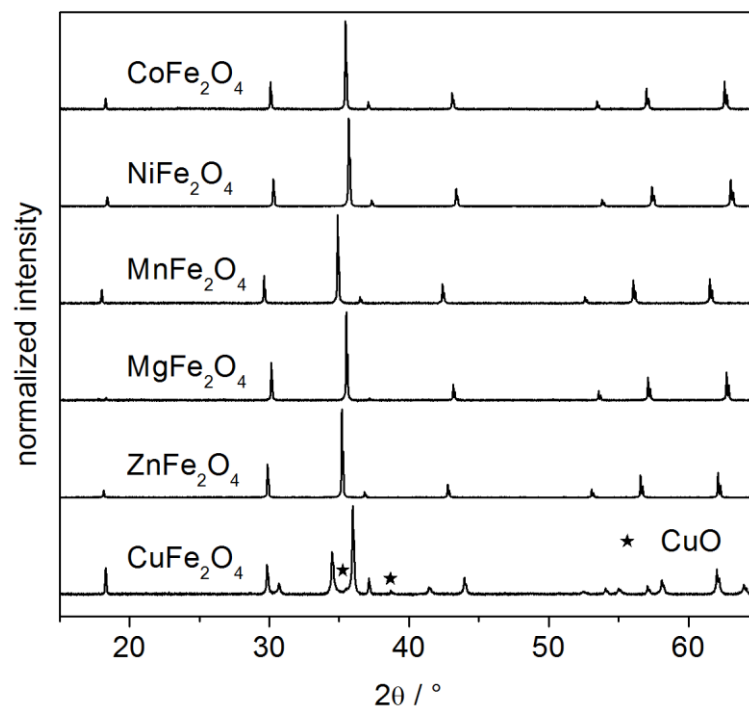


Figure 11: X-ray diffractograms of ferrite spinels prepared by the mixed oxide method.

The field dependent magnetic measurements of the ferrites show ferrimagnetic hystereses for all samples, as shown in Figure 12. The measurements were performed at 300 and 10 K and generally show the expected ferrimagnetic behavior with rising magnetization values and higher coercive fields at lower temperatures.

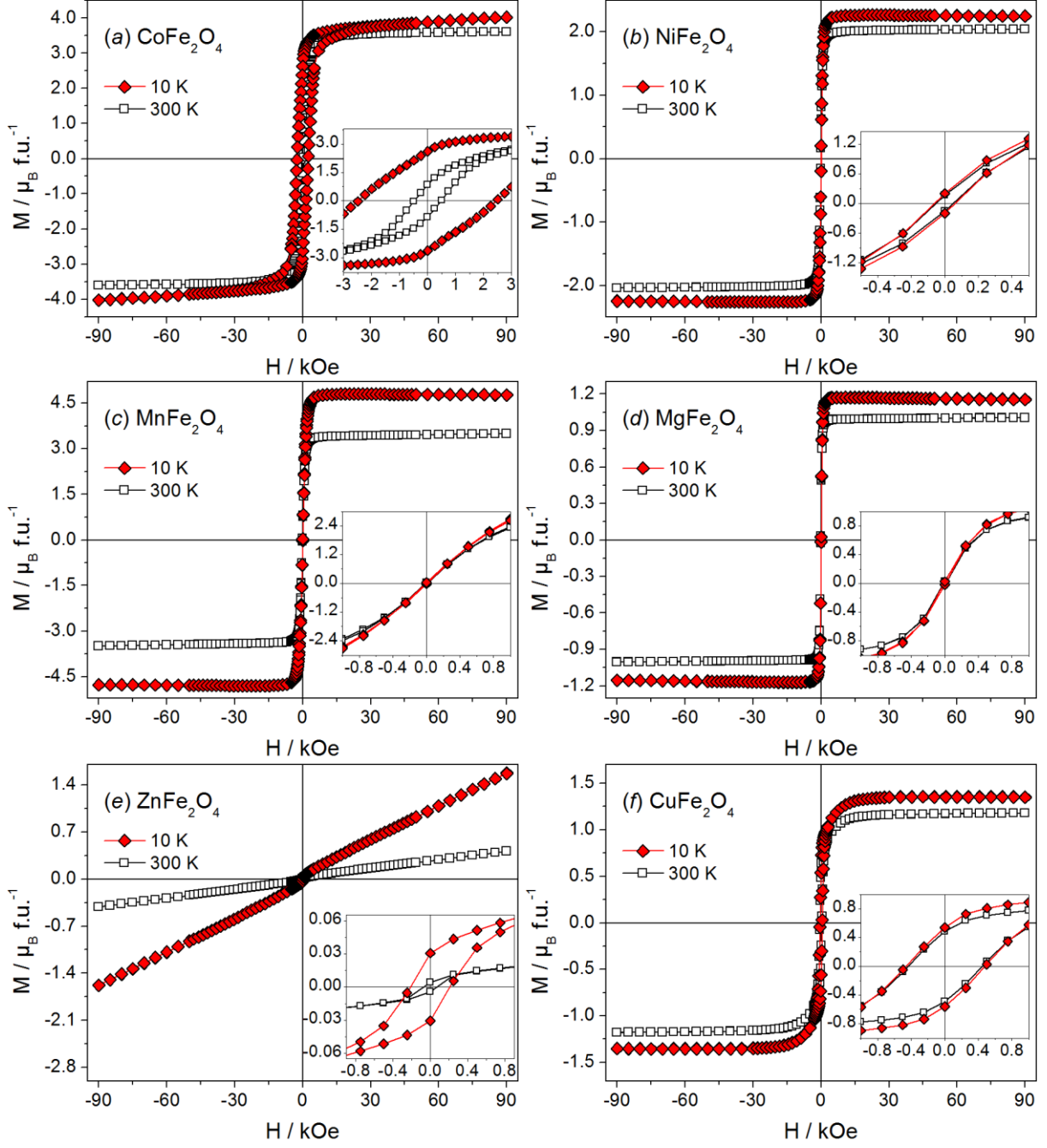


Figure 12: Magnetic field dependent magnetization curves at 300 and 10 K of ferrite spinels prepared by the mixed oxide route: (a)  $\text{CoFe}_2\text{O}_4$ , (b)  $\text{NiFe}_2\text{O}_4$ , (c)  $\text{MnFe}_2\text{O}_4$ , (d)  $\text{MgFe}_2\text{O}_4$ , (e)  $\text{ZnFe}_2\text{O}_4$  and (f)  $\text{CuFe}_2\text{O}_4$ .

The determined saturation magnetizations ( $M_S$ ), remanences ( $M_R$ ) and coercivities ( $H_C$ ) are listed in Table 5. With  $M_S = 3.5 \mu_B$ ,  $\text{CoFe}_2\text{O}_4$  shows the highest saturation magnetization at 300 K. The remanence  $M_R = 0.85 \mu_B$  and coercivity  $H_C = 482 \text{ Oe}$  are the highest values at room temperature, too. In contrast, although high  $M_S$  values could be achieved for  $\text{MnFe}_2\text{O}_4$  and  $\text{MgFe}_2\text{O}_4$ , the corresponding hysteresses were too narrow to be measured accurately with the

ACMS Option of the Quantum Design PPMS.\* ZnFe<sub>2</sub>O<sub>4</sub> showed almost no hysteresis at 300 K but it strongly broadens at 10 K. On the other hand, the M<sub>S</sub>, M<sub>R</sub>, and H<sub>C</sub> values for zinc ferrite are very low. As can be seen in Figure 12 e), ZnFe<sub>2</sub>O<sub>4</sub> is basically paramagnetic with a small ferrimagnetic contribution. This indicates an inversion parameter close to  $i = 0$ .

As can be seen in Table 5, all investigated ferrite spinels possess saturation magnetizations, and thus inversion parameters, that are consistent with the theoretic and literature values for bulk samples. The M<sub>S</sub> values increase when measured at 10 K compared to measurements taken at 300 K. Especially CoFe<sub>2</sub>O<sub>4</sub> and MnFe<sub>2</sub>O<sub>4</sub> the low temperature results fit well into the spin only theory.

In summary, the desired ferrite spinels were prepared successfully by the classic mixed oxide method either phase pure or, in the case of CuFe<sub>2</sub>O<sub>4</sub>, with good purity. The obtained samples and data were used for comparison with the ferrites synthesized by the soft chemistry methods described in the following chapters.

Table 5: M<sub>S</sub>, M<sub>R</sub> and H<sub>C</sub>, literature values of M<sub>S</sub> and theoretical ones. Inversion parameters from literature ( $i_{lit}$ ) and calculated from experimental M<sub>S</sub> values at 10 K ( $i_{exp}$ ).

<b>Ferrite Spinel</b>	<b>T in K</b>	<b>M<sub>S</sub> in μ<sub>B</sub></b>	<b>M<sub>R</sub> in μ<sub>B</sub></b>	<b>H<sub>C</sub> in Oe</b>	<b>M<sub>S</sub> from lit. in μ<sub>B</sub></b>	<b>M<sub>S</sub> μ<sub>theor</sub> in μ<sub>B</sub></b>	<b><math>i_{lit}</math></b>	<b><math>i_{exp}</math></b>
CoFe <sub>2</sub> O <sub>4</sub>	300	3.5	0.85	482.4	3.5	3.8 – 4.2	0.7 – 0.8	~0.82
	10	3.7	2.63	2462.0	[20]		[17]	
NiFe <sub>2</sub> O <sub>4</sub>	300	2.0	0.16	51.2	2.6	2	1.0	0.95
	10	2.3	0.20	61.9	[20]		[21,22]	
MnFe <sub>2</sub> O <sub>4</sub>	300	3.4	0.0	<20	4.1	5	0.2 – 0.6	†
	10	4.8	0.0	<20	[20]		[22–25]	
MgFe <sub>2</sub> O <sub>4</sub>	300	1.0	0.0	<20	1.4 – 1.6	1 – 3	0.7 – 0.9	0.88
	10	1.2	0.0	<20	[20,27]		[26]	
ZnFe <sub>2</sub> O <sub>4</sub>	300	0.03	0.0	<20	0	0 – 1.5	0.0 – 0.3	~0.02
	10	0.11	0.03	212.4	[20]		[28,29]	
CuFe <sub>2</sub> O <sub>4</sub>	300	1.2	0.49	442.2	0.8 – 2.1	1 – 2.6	0.8 – 1.0	0.95
	10	1.4	0.55	470.2	[32,33]		[22,30,31]	

† For MnFe<sub>2</sub>O<sub>4</sub>, the calculation is not possible, because  $\mu_{theor} = 5$  for all inversion parameters.

\* Because of a small residual magnetization of the superconductive magnet in the PPMS when switching from high magnetic fields to zero, hystereses with H<sub>C</sub> < 20 Oe are not measured correctly and can appear as inverted hystereses in the experimental data. See [61] for detailed information.



## **4.2. Ferrite spinels prepared by polyol mediated synthesis**

### 4.2.1. Introduction to polyol synthesis

The so called polyol process was first described as a synthesis method for nanosized metal particles, e.g. copper, by the group of Fernand Fièvet and Michel Figlarz in 1993.[62] It involved a reduction of metal ions using a polyol as solvent.

Polyols in general are molecules that contain more than one alcohol functional group. The most common used polyols are short  $\alpha$ -diols and etherglycols. Using polyols as solvent has some advantages, for examples they have relatively high dipole moments and therefore are able to solvate ionic substances such as metal chlorides, nitrates or acetates quite readily. Additionally, they possess high boiling points and can be heated up to 250 °C under pressure. Because of their multiple oxygen atoms, polyols are also chelating agents which allows them to form metal complexes as intermediates and to coordinate on particle surfaces, preventing aggregations and stopping particle growth.

Over the years, the polyol process was picked up by other groups that amplified the range of preparable compounds from simple metals to various metal oxides such as spinels and perovskites.[63,64] Eventually, additional amphiphils were used as surfactants and ferrite spinels were prepared as described by Caruntu et al.[65]

The polyol synthesis route used in this work derived from a combination of different literature references[62–65] and was adjusted to finally yield phase pure ferrite spinel nanopowders.

### 4.2.2. Characterization of the polyol prepared ferrite spinel powders

X-ray diffractograms of the obtained samples are shown in Figure 13. With the exception of  $\text{CuFe}_2\text{O}_4$ , all ferrites gave diffractograms with a low signal to noise ratio. The spinel reflexes are strongly broadened and only the main peak around 35° indicates the formation of the cubic spinel phases. As will be explained in the following sections (XRD, TEM and BET of the calcined powders) this broadening is due to the small particle sizes of the powders.

In the diffractogram of  $\text{CuFe}_2\text{O}_4$ , comparatively sharp reflexes are present. The peak at 22.8° could not be assigned, but a set of other reflexes can be referenced to  $\text{Cu}_2\text{O}$ . The occurrence of the reduced copper species can be explained as follows: The alcohol function of the diethylene glycol can be oxidized by nitrate to the corresponding aldehyde or carboxylic acid under the formation of nitrogen oxides that evolve as brown gases.[66] While this has no further influence on the preparation of the other ferrites,  $\text{Cu}^{2+}$  ions react with aldehydes and hydroxide to  $\text{Cu}_2\text{O}$ , water and the corresponding carboxylic acid. This reaction is widely used for example in Fehling's test. An additional heat treatment of the powder leads to the oxidation of  $\text{Cu}_2\text{O}$  to

CuO but does not yield the desired  $\text{CuFe}_2\text{O}_4$  species (Figure 16). In summary, it is not possible to obtain  $\text{CuFe}_2\text{O}_4$  under the applied conditions. Correspondingly,  $\text{CuFe}_2\text{O}_4$  was not further investigated. To overcome these side reactions it could be favorable to use chlorides instead of nitrates as starting materials to prevent the oxidation of the alcohol function of the solvent and thus the reduction of  $\text{Cu}^{2+}$ .

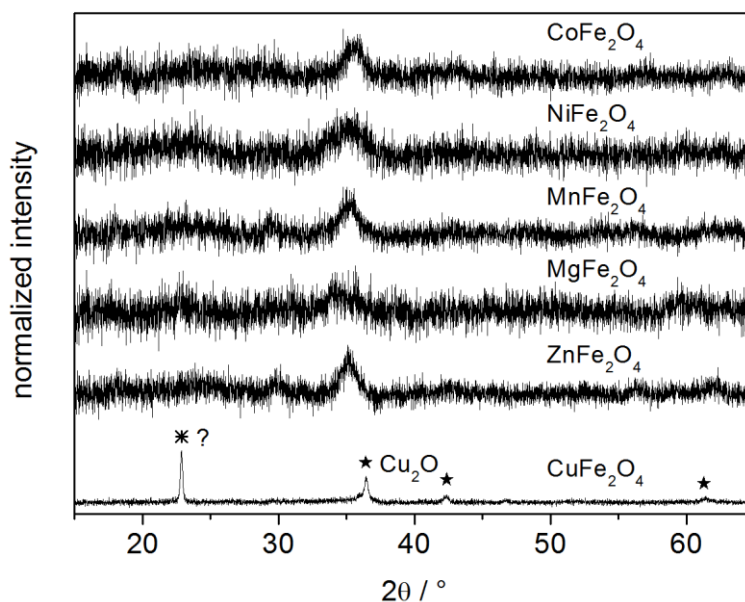


Figure 13: X-ray diffractograms of the as prepared ferrite spinels synthesized by the polyol method. A background correction was performed for all diffractograms.

To determine residuals of nitrates, diethylene glycolate, water and hydroxides, the powders were characterized by thermogravimetric analyses (TGA). In general, all powders contain a high amount of thermally decomposable substances. The weight losses range from 32% to 60% at temperatures between 250 and 400 °C as listed in detail in Table 6 and shown exemplarily for two samples in Figure 14 (a).

In Figure 14 (b), the X-ray diffractograms of  $\text{CoFe}_2\text{O}_4$  calcined at 250 °C and 950 °C are compared. With the pattern of the as prepared sample in mind (Figure 13), it can be seen that, with increasing temperature, the peaks of the spinel phase get sharper, reflecting a successive crystallite growth. Furthermore, no additional side reactions or secondary phases occur at elevated temperatures.

For further investigations, aliquots of the as prepared ferrites from the polyol syntheses were heated for one hour at the respective calcination temperatures determined by TGA (listed in Table 6). These samples are denoted as ‘calcined’ in the following.

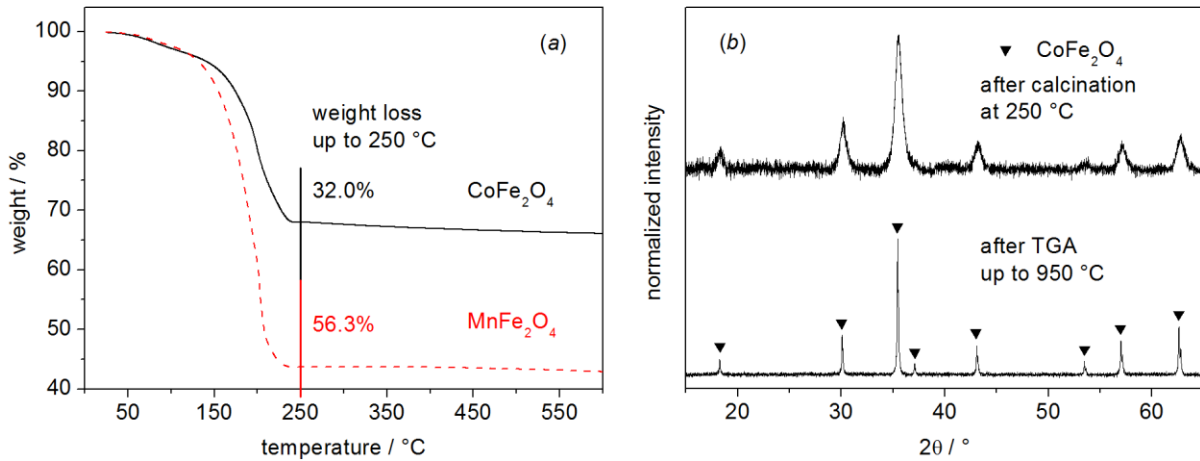


Figure 14: (a) Exemplarily thermogravimetric measurement of the as prepared ferrite spinel powders of  $\text{CoFe}_2\text{O}_4$  and  $\text{MnFe}_2\text{O}_4$  synthesized by the polyol route and (b) X-ray diffractograms of  $\text{CoFe}_2\text{O}_4$  after calcination at  $250\text{ }^\circ\text{C}$  and after the TGA measurement.

The particle/crystallite sizes of the samples, calcined at the corresponding temperature with no further weight loss, were determined by two different methods. In a first step the specific surface areas of the powders were measured via nitrogen physisorption according to the Brunauer, Emmett and Teller (BET) theory.[67] Presuming uniformly cubic or spherical particles, the corresponding sizes can be calculated from the specific surface areas and the crystallographic density as follows:

$$\text{particle size (nm)} = \frac{6000}{\rho \text{ (g cm}^{-3}\text{)} \cdot A \text{ (m}^2 \text{ g}^{-1}\text{)}}$$

Using this method, the average particle sizes were calculated to be in the range of 10 to 16 nm, as listed in Table 6. From the X-ray patterns an average crystallite size can be determined by the Scherrer equation using the Full Width at Half Maximum (FWHM) values.[68] The FWHMs were determined by fitting of the reflexes with the program WinXpow. The results are in the same range as from the BET investigations and are listed in Table 6, too. Because of the similarity of crystallite and particle sizes it can be concluded that each powder particle consists of one crystallographic domain.

To get a better understanding of the particle morphologies and size distributions, transmission electron microscopy (TEM) investigations were performed. Selected micrographs with different magnifications of the calcined  $\text{CoFe}_2\text{O}_4$  and  $\text{NiFe}_2\text{O}_4$  powders are shown in Figure 15. The powders consist of micrometer sized conglomerates of mostly uniform, spherical particles with a narrow size distribution ranging from 10 to 50 nm with most of the particles being close to 10 nm. Hence, the results from the BET and Scherrer calculations were confirmed by TEM.

Table 6: TGA results and particle/crystallite sizes derived from BET and XRD measurements of the calcined ferrite spinel powders synthesized by polyol route.

<b>Compound</b>	<b>Temperature in °C</b>	<b>Weight loss in %</b>	<b>Particle size in nm</b>	<b>Crystallite size in nm</b>
CoFe <sub>2</sub> O <sub>4</sub>	250	32.0	15	13
NiFe <sub>2</sub> O <sub>4</sub>	400	48.6	14	14
MnFe <sub>2</sub> O <sub>4</sub>	250	56.3	10	10
MgFe <sub>2</sub> O <sub>4</sub>	400	60.3	16	12
ZnFe <sub>2</sub> O <sub>4</sub>	350	56.2	14	13

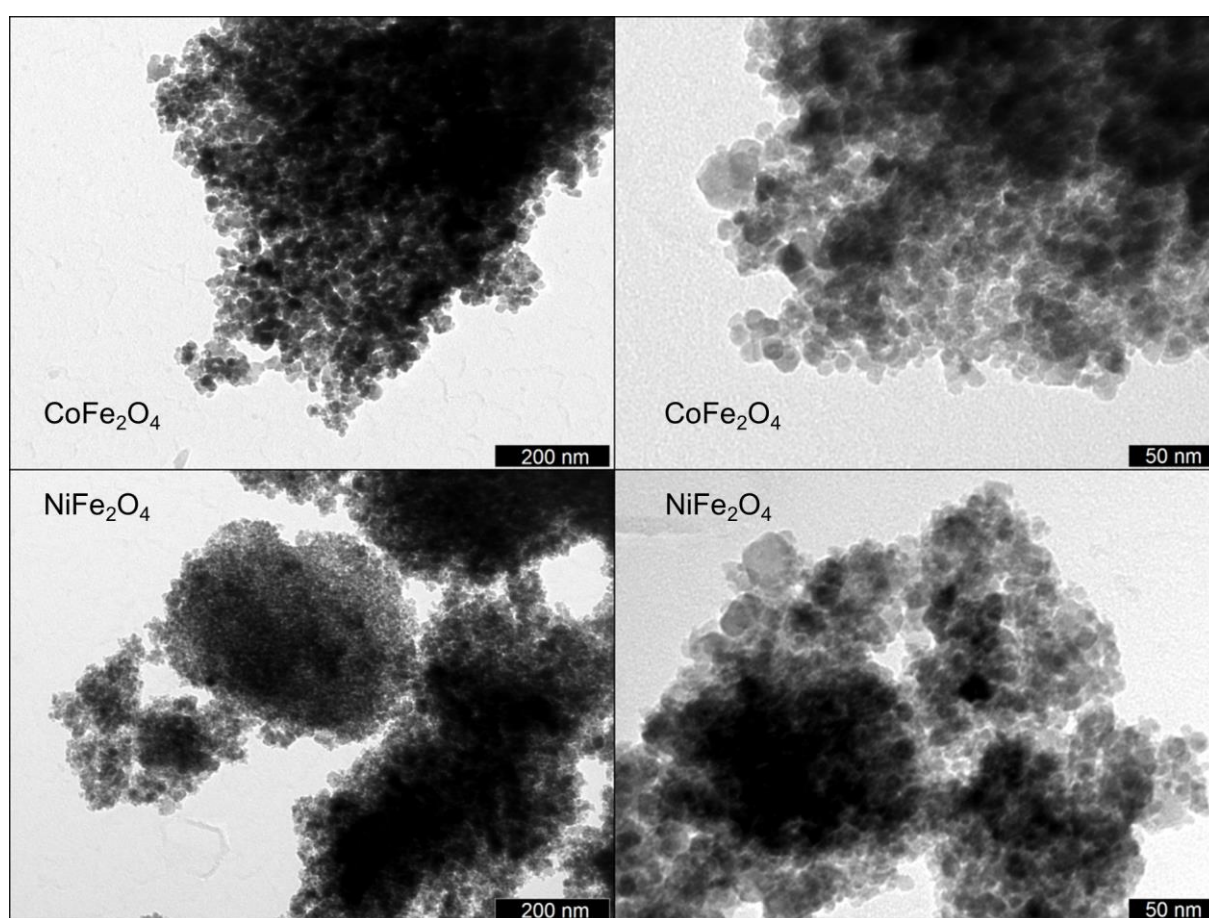


Figure 15: TEM micrographs of CoFe<sub>2</sub>O<sub>4</sub> and NiFe<sub>2</sub>O<sub>4</sub> polyol powders after calcination at 250 °C and 400 °C, respectively.

In general, all ferrites show a temperature dependent particle growth but the samples of  $\text{MnFe}_2\text{O}_4$  and  $\text{CuFe}_2\text{O}_4$  undergo side reactions at higher temperatures as derived from the X-ray diffractograms shown in Figure 16. The  $\text{CuFe}_2\text{O}_4$  sample treated at  $950\text{ }^\circ\text{C}$  contains  $\text{CuO}$  and  $\text{Fe}_2\text{O}_3$  as impurities.

The formation of manganese ferrite cannot unambiguously be proven. After calcination of the as prepared powder at  $600\text{ }^\circ\text{C}$  a spinel phase forms but the Bragg angles are in better accordance with  $\text{Fe}_3\text{O}_4$  (PDF 75-0033) than  $\text{MnFe}_2\text{O}_4$  (PDF 10-0319) or  $\text{Mn}_3\text{O}_4$  (PDF 24-0734). Additionally, hematite (that is not present in the sample calcined at  $250\text{ }^\circ\text{C}$ ) was found. A qualitative test of the  $\text{MnFe}_2\text{O}_4$  powder was performed by oxidizing a sample with  $\text{KNO}_3$  in a bunsen burner flame in the presence of carbonate ions. The resulting green color of  $\text{MnO}_4^{2-}$  confirms the presence of Mn. However, it seems likely that the precipitation of Mn was not quantitative during the polyol synthesis. Thus, the applied conditions most likely do not lead to phase pure  $\text{MnFe}_2\text{O}_4$ .

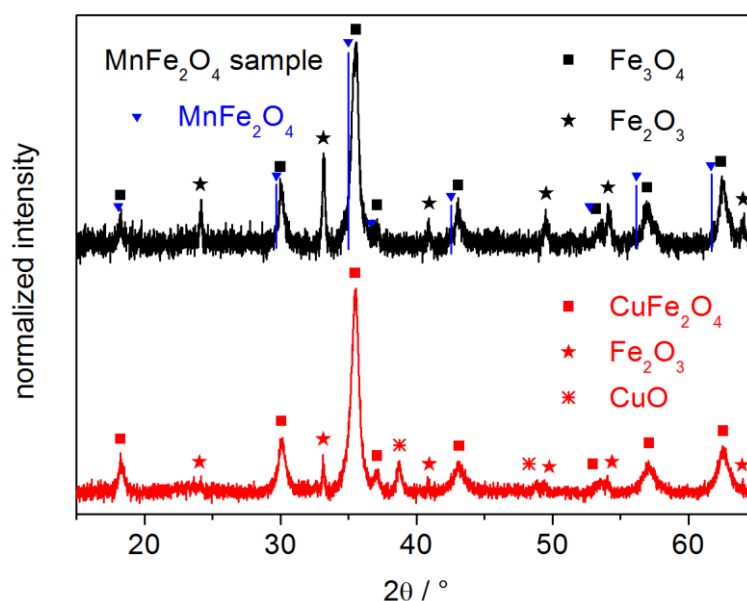


Figure 16: X-ray diffractograms of thermally treated ( $600\text{ }^\circ\text{C}$ )  $\text{MnFe}_2\text{O}_4$  and  $\text{CuFe}_2\text{O}_4$  powders from the polyol synthesis.

#### 4.2.3. Magnetic properties of polyol prepared ferrite spinel powders

Superparamagnetism describes a single domain behavior of sufficiently small ferro- or ferrimagnetic particles. When the particle size is below a compound-specific critical limit, the magnetic moments are locked together and act as a super magnetic moment. By thermal relaxations, this moment fluctuates and with a measuring time higher than the relaxation time the net magnetization is zero without an applied external field, leading to the disappearance of the hysteresis in magnetic field dependent measurements.[69]

Obviously, the thermal fluctuation of the magnetic moments depends on the temperature and the transition temperature between “free” fluctuation and locked magnetic moment is called blocking temperature ( $T_B$ ). Below  $T_B$  the field dependent magnetization curves exhibit hystereses whereas above  $T_B$  no remanence or coercivity but only a saturation magnetization can be observed. There are multiple influences on the blocking temperature. An applied DC magnetic field, for example, results in a lowering of  $T_B$ . Smaller particles sizes also lead to a lowering of  $T_B$ . Furthermore, the measuring time has a great impact on the observed  $T_B$ . That leads to a wide range of possible blocking temperatures for any substance from several Kelvin to more than room temperature.[69]

The field dependent magnetic properties of the calcined polyol prepared powders were characterized and the graphs are shown in Figure 17. The corresponding saturation and remanent magnetization values and coercivities are listed in Table 7. All samples show ferrimagnetic behavior at 10 K. Whereas cobalt ferrite also shows a distinct hysteresis with considerable remanent magnetization and coercive field at 300 K, the hystereses of nickel, magnesium and zinc ferrite become very small at room temperature. This behavior is part of the superparamagnetism that is expected for magnetic particles with sizes smaller than about 20 nm, depending on the anisotropy constants and  $M_S$  values of each compound. Cobalt ferrite for example, has been studied intensely and, depending on the particle size, its saturation magnetization can be varied from values as low as  $0.9 \mu_B$  [70] to  $2.7 \mu_B$  [71] and even up to the bulk value of  $3.5 \mu_B$  [20]. For small particles of  $ZnFe_2O_4$  it is known that an exchange of  $Zn^{2+}$  and  $Fe^{3+}$  between tetrahedral and octahedral sites can occur and nanoscale samples have considerably higher ferrimagnetism than the bulk.[72] This can explain the significantly increased hysteresis of the polyol prepared  $ZnFe_2O_4$  compared to the mixed oxide sample.

Temperature dependent magnetization measurements, depicted in Figure 18, reveal the occurrence of blocking temperatures and therefore prove superparamagnetic properties for all powders.

The blocking temperatures were determined from the maximum magnetization values of the ZFC curves. Whereas the  $T_B$  values for Ni, Mg and  $ZnFe_2O_4$  are below 300 K, it seems that for  $CoFe_2O_4$   $T_B$  is significantly higher under the applied measuring conditions and is not yet reached up to 300 K. For this reason, the  $CoFe_2O_4$  sample appears to be ferrimagnetic in the field dependent measurements at 300 K.

Table 7: Saturation magnetization, remanence magnetization and coercive fields measured at 300 K and 10 K of the calcined ferrite spinels prepared by the polyol method.

<b>Compound</b>	<b>Temperature</b>	<b><math>M_S</math> in <math>\mu_B</math></b>	<b><math>M_R</math> in <math>\mu_B</math></b>	<b><math>H_C</math> in Oe</b>
$CoFe_2O_4$	300 K	2.2	0.2	228
	10 K	2.4	1.9	16484
$NiFe_2O_4$	300 K	1.6	0.0	< 20
	10 K	1.9	0.5	323
$MgFe_2O_4$	300 K	0.8	0.0	< 20
	10 K	1.0	0.3	360
$ZnFe_2O_4$	300 K	0.3	0.0	< 20
	10 K	1.7	0.3	254

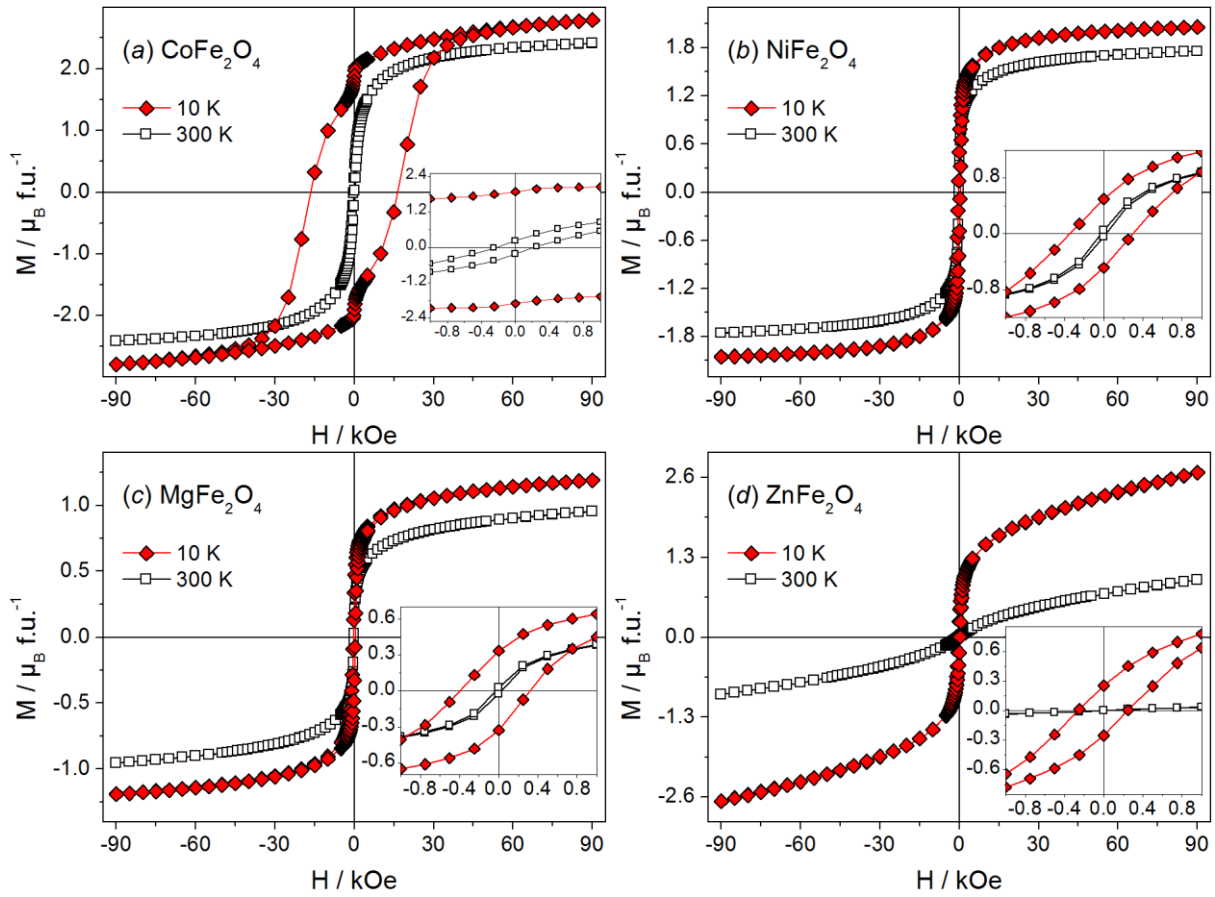


Figure 17: Magnetic field dependent magnetization curves at 300 and 10 K of calcined ferrite spinels prepared by polyol route: (a)  $\text{CoFe}_2\text{O}_4$ , (b)  $\text{NiFe}_2\text{O}_4$ , (c)  $\text{MgFe}_2\text{O}_4$  and (d)  $\text{ZnFe}_2\text{O}_4$ .

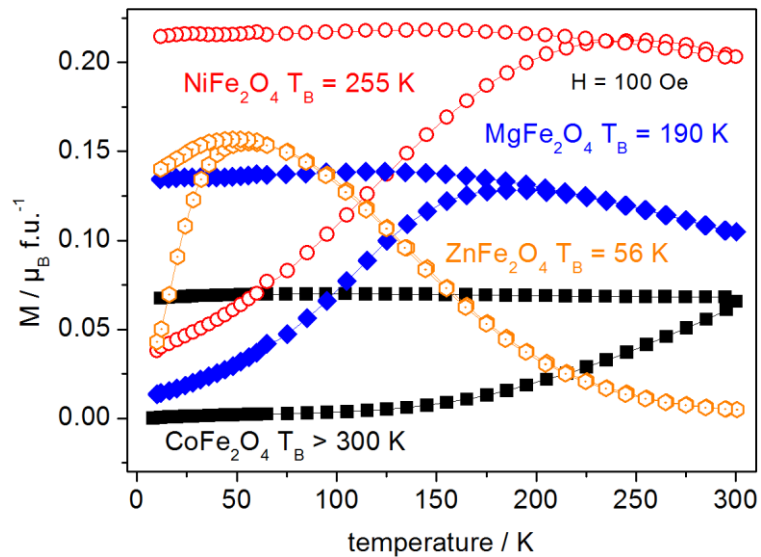


Figure 18: Temperature dependent magnetizations of the calcined ferrite powders prepared by the polyol method.



Additional calcination experiments at different temperatures were performed to gain a better understanding of the particle growth at temperatures suitable to achieve dense ceramic bodies. Therefore, samples of  $\text{CoFe}_2\text{O}_4$  were calcined for 1 h at 400, 600, 800 and 1000 °C respectively. The calcined powders were characterized by XRD and the resulting diffractograms are shown in Figure 19. With increasing calcination temperature, the peaks in the X-ray diffractograms get sharper and the signal-to-noise ratio rises because of the increasing crystallinity of the samples.

TEM micrographs, depicted in Figure 21, show the temperature dependent growth of the particles as indicated by the sharpening reflexes and thus bigger crystallites in the X-ray diffractograms. The particle sizes of the powder, heated at 400 °C, range from 15 to 40 nm. After treatment at 600 °C, the sizes increase to 20 to 45 nm and the particles start to form sharp edges. At 800 °C all crystallites exhibit sharp edges with a size between 50 and 150 nm and the powders are no longer exclusively nanoparticles. The smallest particles of the sample treated at 1000 °C are about 300 nm in diameter and the biggest are close to the  $\mu\text{m}$  range.

The corresponding magnetic properties are shown in Figure 20. Although the sample calcined at 400 °C shows a distinct hysteresis, the  $M_S$ ,  $M_R$ , and  $H_C$  values are small when compared to the other samples. For higher calcination temperatures, the saturation and remanent magnetizations rise. The coercivity reaches a maximum at 800 °C and then decreases. The values are summarized in Table 8.

Table 8: Saturation magnetization, remanence magnetization and coercive fields measured at 300 K the  $\text{CoFe}_2\text{O}_4$  polyol powders calcined at different temperatures.

<b>Calcination temperature</b>	<b><math>M_S</math> in <math>\mu_B</math></b>	<b><math>M_R</math> in <math>\mu_B</math></b>	<b><math>H_C</math> in Oe</b>
<b>400 °C</b>	2.1	0.40	636
<b>600 °C</b>	3.0	0.92	1135
<b>800 °C</b>	3.1	1.17	1226
<b>1000 °C</b>	3.2	1.16	933
<b>1100 °C (see MO method)</b>	3.5	0.85	483

Concluding, the particle size of the ferrites and their magnetic properties are tunable by the calcination temperature. The particle growth continues with increasing temperature and the saturation and remanence magnetization values as well as the coercivities, are strongly dependent on the particle size.

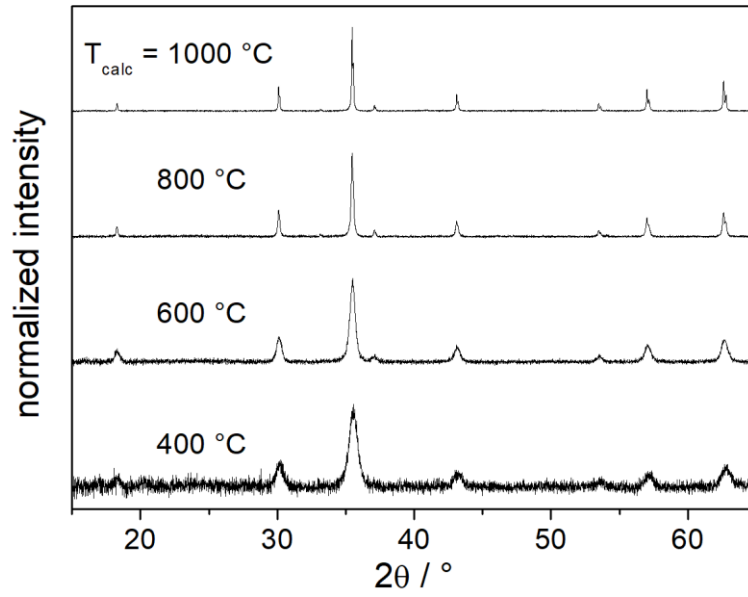


Figure 19: X-ray diffractograms of the  $\text{CoFe}_2\text{O}_4$  polyol powders calcined at different temperatures.

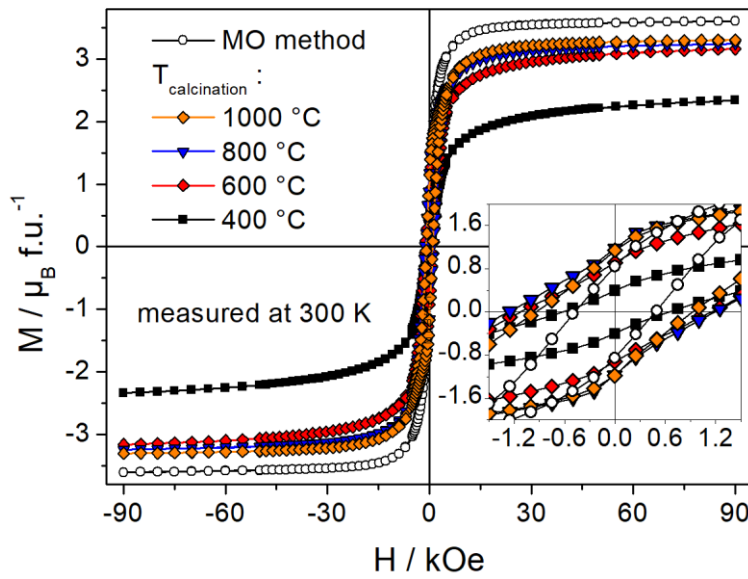


Figure 20: Field dependent magnetization measurements of the  $\text{CoFe}_2\text{O}_4$  polyol powders calcined at different temperatures.

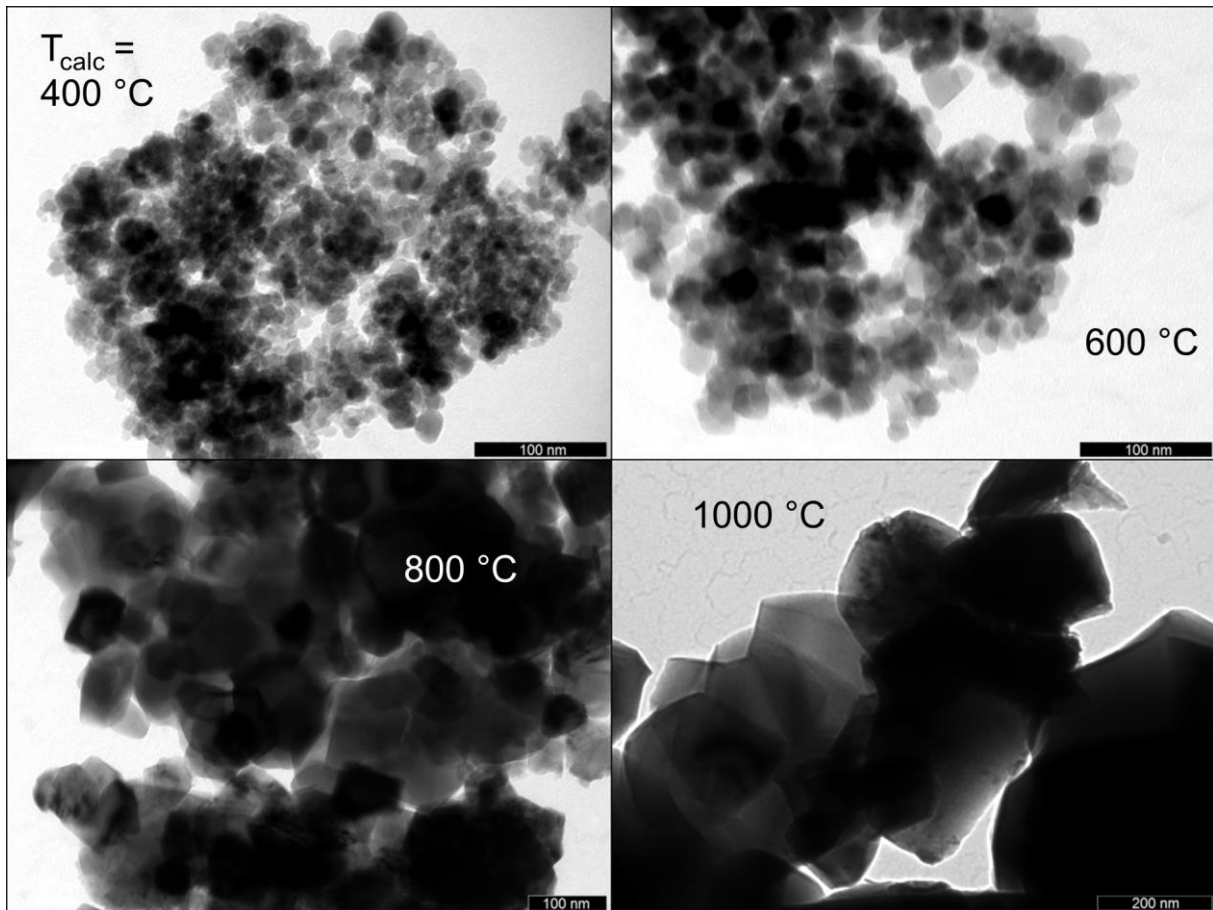


Figure 21: TEM micrographs of  $\text{CoFe}_2\text{O}_4$  samples calcined at different temperatures.

In summary, the polyol method proved to be a convenient synthesis approach to prepare cobalt, nickel, magnesium and zinc ferrite spinel powders with particle sizes in the range of 10 to 20 nm. In the case of manganese and copper ferrite, side reactions occur and therefore other preparation routes should be used.

TEM investigations along with BET and XRD reveal a homogeneous size distribution and the single crystalline nature of the single particles.

When calcined at low temperatures, the powders exhibit superparamagnetic properties. The particle size, and hence the magnetic behavior, can be tuned by further thermal treatments at higher temperatures.

### **4.3. Functionalized cobalt and nickel ferrite spinels.**

#### 4.3.1. Surface modification of nanoparticles

In the polyol synthesis, surface active agents are frequently used to limit the particle growth. The idea to use amphiphilic agents in the synthesis of ferrite spinels was inspired by a paper of Caruntu et al.[65] In this publication, different carboxylic acids as myristic acid and oleic acid were used to obtain discrete monodisperse nanoparticles of ferrite spinels. As the authors showed it is possible to synthesize different  $MFe_2O_4$  samples with  $M^{2+} = Fe, Mn, Co, Ni$  and  $Zn$  with only slight alterations of the preparation conditions.

Therefore, the size control of the nanoparticles using a similar capping agent was aimed at. Palmitic acid was chosen as detergent because of its long alkylic chain and predictably strong preference to interact with the polar surface of the metal oxides with the carboxylate function. As described in the following paragraphs, the palmitic acid indeed coordinates to the nanoparticles surface while forming a “shell” of alkylic chains, making the particles hydrophobic enough to precipitate from the solvent diethylene glycol. Additionally, the synthesized powders were completely soluble in nonpolar solvents, which is advantageous for further applications.

#### 4.3.2. Characterization of the palmitic acid capped cobalt and nickel ferrites

The powders were found to be indissoluble in polar solvents but dissolve easily in nonpolar solvents such as toluene, chloroform, diethyl ether and heptane. These findings agree with the general assumption that the polar carboxylate function of the palmitate interacts with the polar ferrite spinels and the alkyl groups form a hydrophobic sphere around these particles.

With a sufficient concentration of nanoparticles, the so obtained solutions form a ferro fluid that can be manipulated with external magnetic fields. An image of a saturated solution of the palmitate capped cobalt ferrite particles in chloroform is shown in Figure 22.



Figure 22: A saturated solution of palmitate capped  $\text{CoFe}_2\text{O}_4$  particles in chloroform next to a permanent magnet. The solution is drawn towards the magnet.

The homogeneous solutions can be used as starting materials for further syntheses. For example a solution of palmitic acid capped  $\text{CoFe}_2\text{O}_4$  was used for spray drying and the mixed spinels of  $\text{Co}_x\text{Ni}_{(1-x)}\text{Fe}_2\text{O}_4$  were used for the formation of uniform thin films on indium tin oxide substrates to investigate their catalytic properties in the electrochemical oxygen evolution and oxygen reduction reactions. The latter is described more thoroughly in one of the following sections.

In the X-ray diffractograms of the palmitic acid capped ferrite spinels only the main peak (311) of the spinel structure at  $35^\circ 2\theta$  is detected as is shown exemplarily in Figure 23 for  $\text{Co}_{0.4}\text{Ni}_{0.6}\text{Fe}_2\text{O}_4$ . Additionally, a set of reflexes shows conformity with a reference of calcium palmitate. Because there is no calcium involved in the synthesis, it can be concluded that a structure similar to calcium palmitate forms, i.e. palmitate coordinated to a bivalent metal ion, formed. Calcination of the as prepared powders for 30 min at  $950^\circ\text{C}$  resulted in a sharpening of the ferrite spinel peaks without the occurrence of any impurities.

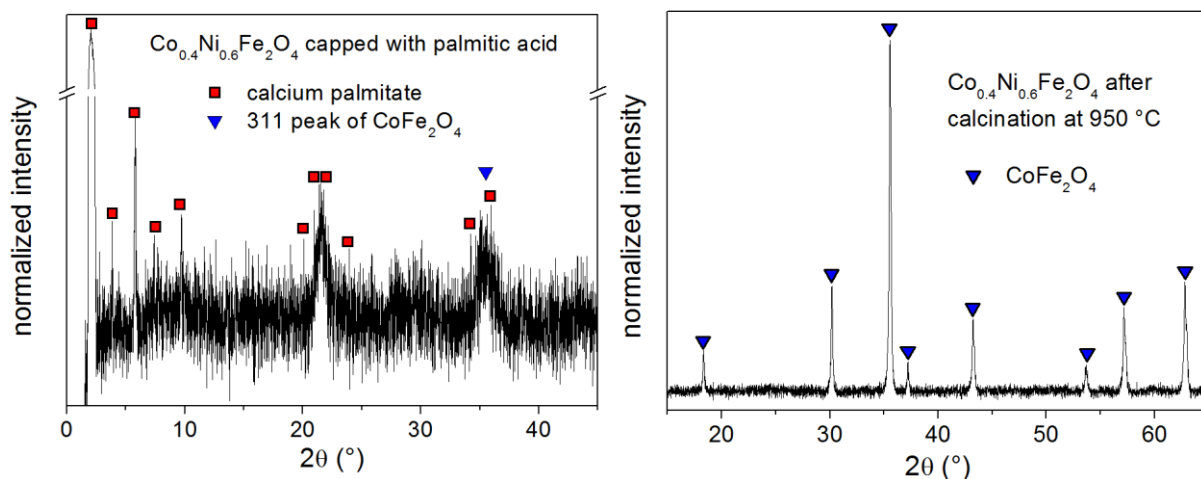


Figure 23: X-ray diffractogram of the as prepared powder of  $\text{Co}_{0.4}\text{Ni}_{0.6}\text{Fe}_2\text{O}_4$  (*left*) and after calcination at  $950\text{ }^\circ\text{C}$  (*right*).

Raman investigations of the as prepared powders showed that the spinel structure has already formed. A typical Raman spectrum of these powders in comparison with a spectrum of  $\text{CoFe}_2\text{O}_4$ , prepared by the mixed oxide method, is shown in Figure 24. These spectra prove that the as prepared powders are not a mixture of cobalt, nickel and iron oxides, hydroxides or nitrates because such components would readily be detectable in the Raman spectra. Only traces of hematite ( $\text{Fe}_2\text{O}_3$ ) are present in the spectra. Furthermore, bands related to palmitic acid prove the presence of the organic surface coating.

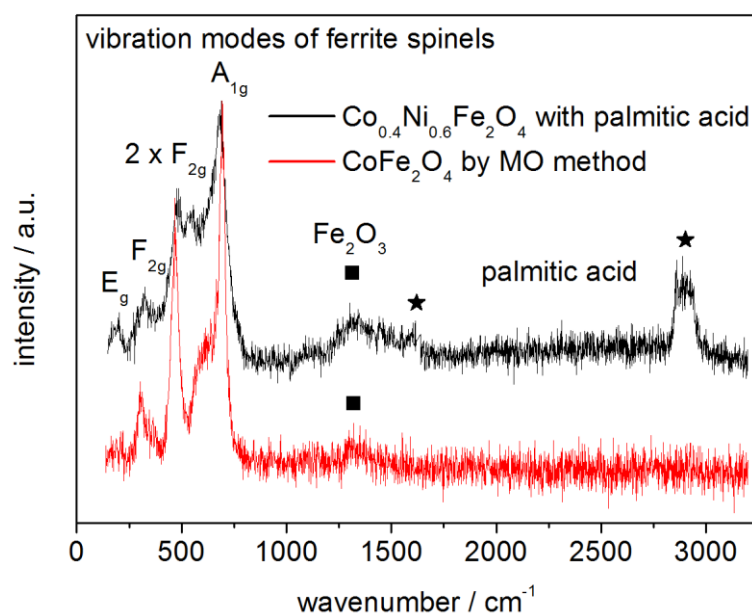


Figure 24: Raman spectrum of an as prepared palmitic acid functionalized ferrite spinel.

The thermogravimetric investigation in flowing synthetic air is shown in Figure 25. The palmitic acid functionalized powders lose 40 – 60% of their weight between room temperature and 450 °C. The main weight loss occurs at temperatures around 250 °C. Higher temperatures of up to 950 °C do not lead to any further weight changes. Thus, the palmitic acid can be decomposed completely from the system by calcination without destroying the ferrites, but of course a particle growth has to be taken into consideration during the heat treatment.

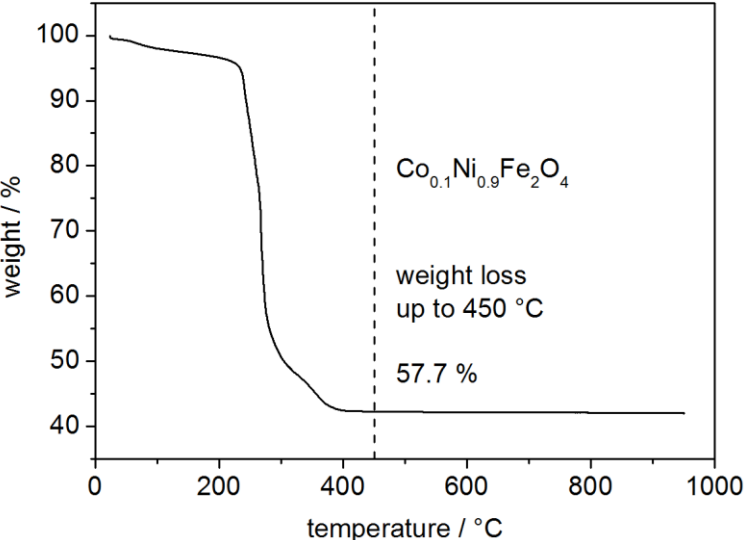


Figure 25: Thermogravimetric measurement of a ferrite spinel capped with palmitic acid.

The palmitic acid capped powders show ferrimagnetic and superparamagnetic properties. Similar to the samples prepared by the polyol method without additional surface functionalization. Corresponding graphs are shown in Figure 26 exemplarily for  $\text{Co}_{0.9}\text{Ni}_{0.1}\text{Fe}_2\text{O}_4$ .

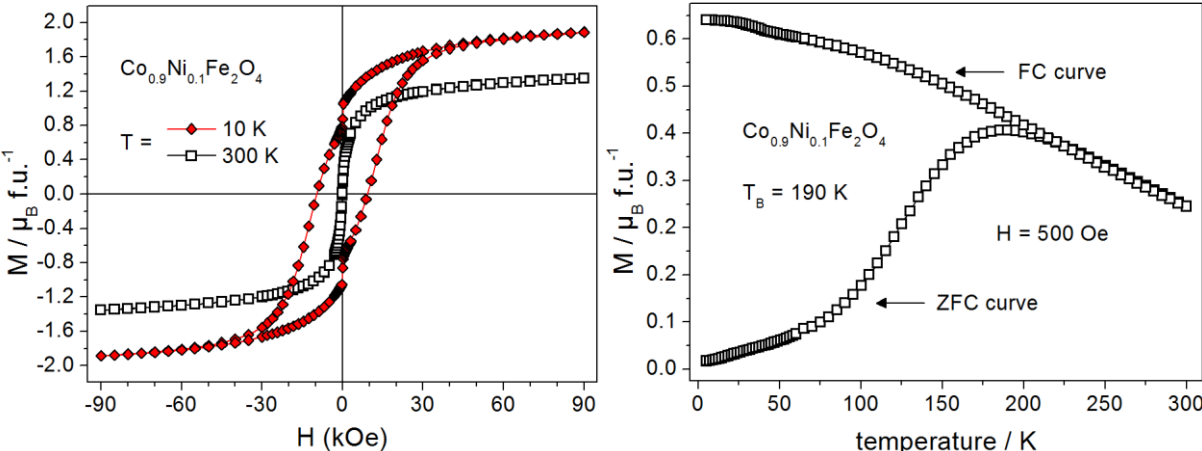


Figure 26: Field (*left*) and temperature (*right*) dependent magnetization of  $\text{Co}_{0.9}\text{Ni}_{0.1}\text{Fe}_2\text{O}_4$  capped with palmitic acid.

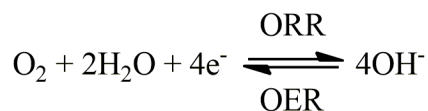
In Table 9 the saturation magnetizations, remanences, coercivities and blocking temperatures are listed for the complete  $\text{Co}_x\text{Ni}_{(1-x)}\text{Fe}_2\text{O}_4$  series. It was found that all values decrease with increasing nickel content, in consistence with literature.[73–76]

Table 9: Saturation and remanence magnetizations and coercive fields at different temperatures and blocking temperatures of as prepared ferrite spinels capped with palmitic acid.

$\text{Co}_x\text{Ni}_{(1-x)}\text{Fe}_2\text{O}_4$	$M_S$ in $\mu_B$ at		$M_R$ in $\mu_B$ at		$H_C$ in Oe at		$T_B$ in K
	300 K	10 K	300 K	10 K	300 K	10 K	
x = 1	0.49	0.81	0.00	0.41	<20	9900	140
0.9	1.17	1.64	0.00	0.87	<20	9470	190
0.8	0.57	0.92	0.00	0.43	<20	7480	145
0.7	0.31	0.58	0.00	0.24	<20	6570	125
0.6	0.25	0.50	0.00	0.14	<20	743	110
0.5	0.15	0.38	0.00	0.08	<20	1540	90
0.4	0.22	0.47	0.00	0.09	<20	850	110
0.3	0.18	0.42	0.00	0.13	<20	3536	85
0.2	0.12	0.36	0.00	0.07	<20	1500	65
0.1	0.07	0.31	0.00	0.03	<20	303	26
0.0	0.06	0.32	0.00	0.00	<20	<20	11

#### 4.3.3. Catalytic properties in the oxygen evolution and reduction reaction

The oxygen reduction reaction (ORR) and the oxygen evolution reaction (OER) are two major electrochemical challenges in the development of reversible fuel cells operating on oxygen.[77]



3d metal spinels have been reported to be interesting compounds for catalyzing both reactions.[78] For this reason, the  $\text{Co}_x\text{Ni}_{(1-x)}\text{Fe}_2\text{O}_4$  series was screened with linear sweep voltammetry (LSV) and scanning electrochemical microscopy (SECM) to reveal the catalytic properties in the OER and ORR. This characterization was done by Gerda Seiffarth and Matthias Steimecke from the group of Prof. Michael Bron at the Martin Luther University Halle-Wittenberg and the results were published in a peer reviewed journal.[79]



Essential for the investigations are evenly distributed thin films of the catalyst on the indium tin oxide substrates. Because of the palmitic acid functionalization, the as prepared spinel powders are soluble in nonpolar solvents. Therefore, solutions of the spinels can be pipetted onto the substrate and uniform films form upon evaporation of the organic solvent. The desired film thickness can easily be adjusted by variation of the concentration and repeating the coating step several times.

The sample  $\text{Co}_{0.1}\text{Ni}_{0.9}\text{Fe}_2\text{O}_4$  showed the most promising activities as OER catalyst and was mixed with nitrogen doped carbon nanotubes (NCNT), which are known to be good ORR catalysts to obtain a bifunctional electrocatalyst. As can be seen from Figure 27, the mixture of the ferrite spinel and the NCNT is a suitable bifunctional electrocatalyst for both, the ORR (high negative current density at negative potentials) and the OER (high current density at positive potentials). The results are described in detail in [79].

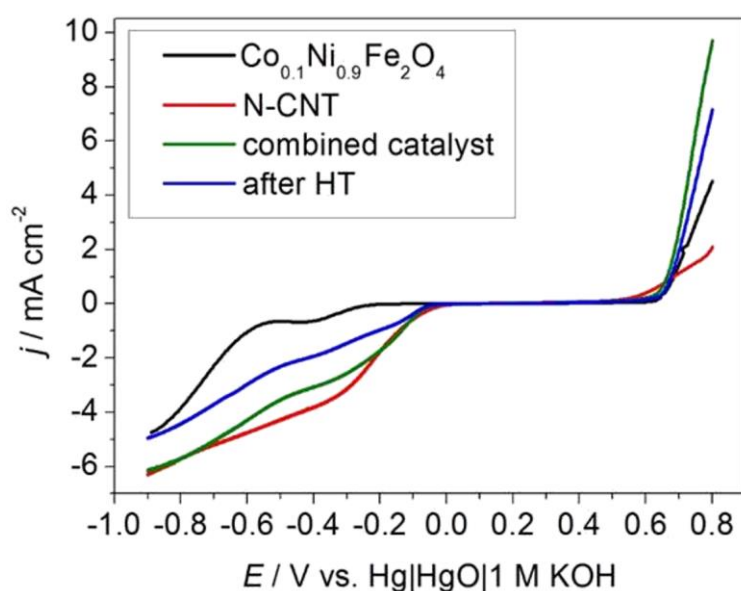


Figure 27: Combination of ORR and OER polarization curves of the ferrite spinel, NCNT, mixed sample and heat treated mixed sample. Edited from [79].

#### 4.4. Composites of $\text{CoFe}_2\text{O}_4$ and $\text{BaTiO}_3$ with 2-2 connectivity

The following findings were obtained together with Norman Quandt during his time as master candidate. The results were published in [57] and are summarized in the following. The full article is included in the appendix as A1.

As mentioned in the introduction, aligning different phases in (alternating) layers is referred to as 2-2 connectivity. To realize this type of structure, the ferroic layers were spin coated in a triple layer system onto Pt-coated silicon wafers. In this arrangement, a  $\text{CoFe}_2\text{O}_4$  layer was placed between a bottom and a top layer of  $\text{BaTiO}_3$ . In addition to its ferroic properties,  $\text{BaTiO}_3$  acts as insulating material and to minimize leakage currents.

Both  $\text{CoFe}_2\text{O}_4$  and  $\text{BaTiO}_3$  were spin coated from a solution of the respective metal salts in a mixture of DMF and acetic acid. Each spin coating step was followed by the heat treatment shown in Figure 28.

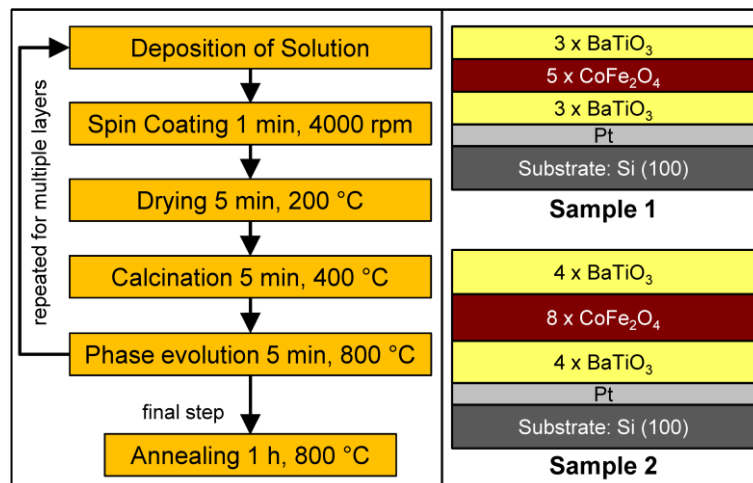


Figure 28: Reaction flow chart of triple layer multiferroics.[57]

The resulting multilayers were investigated with scanning electron microscopy to determine their structure. In Figure 29 the images of the two samples are shown.

The magnetic and electric polarization properties of the obtained thin film multiferroics were investigated. As depicted in Figure 30, it was found that the samples exhibit both magnetic and electric polarization hystereses, which is essential for magnetoelectric coupling. The magnetoelectric properties of the thin film structures are still to be characterized, which is not trivial as the electric polarization turned out to be difficult.

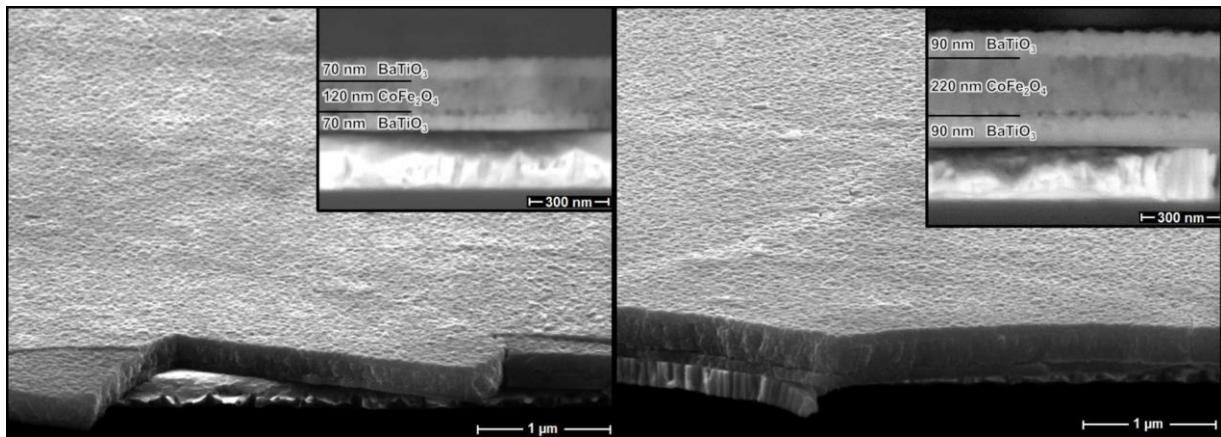


Figure 29 Scanning electron microscopy images, revealing the triple layer structure of the samples. Edited from [57].

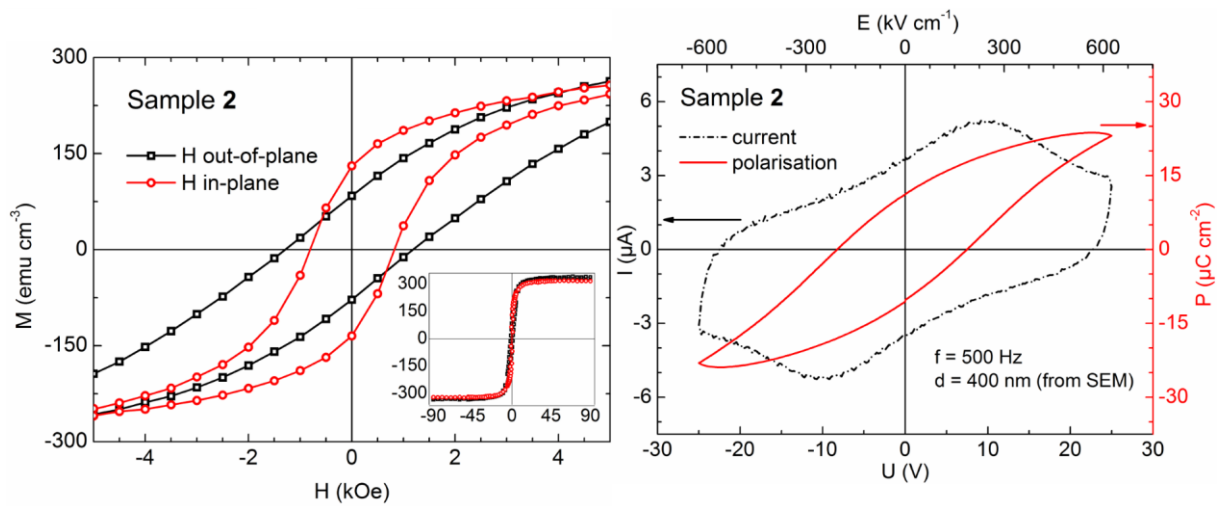


Figure 30: Magnetic (left) and electric polarization (right) hystereses of sample 2 from [57].

#### 4.5. Composites of CoFe<sub>2</sub>O<sub>4</sub> and BaTiO<sub>3</sub> with 0-3 connectivity

The results in this chapter have been published in [58].

The 0-3 composites of CoFe<sub>2</sub>O<sub>4</sub> and BaTiO<sub>3</sub> were prepared from powders synthesized by the polyol mediated synthesis method. A cobalt ferrite nanopowder was prepared by the polyol mediated synthesis, as described in chapter 4.2. and was redispersed in diethylene glycol. Barium hydroxide and titanium isopropoxide were added under protective argon atmosphere as barium titanate starting compounds. This mixture was refluxed to form the barium titanate precursor together with the cobalt ferrite embedded.

The resulting powdery mixture was treated in air to decompose carbonates and to form barium titanate. To form dense ceramics suitable for magnetoelectric measurements, sintering temperatures of at least 1200 °C had to be carried out.

Unfortunately, barium titanate reacts with cobalt ferrite in air at temperatures higher than 900 °C and forms side products like barium hexaferrites (BaFe<sub>12</sub>O<sub>19</sub>). The situation becomes even more complicated since Ti<sup>4+</sup>/Co<sup>2+</sup> can substitute Fe<sup>3+</sup> in BaFe<sub>12</sub>O<sub>19</sub>. Additionally, cobalt and iron can be incorporated in barium titanate, leading to an increased electric conductivity which is highly undesired for magnetoelectrics.

To avoid these problems, a reductive sintering step followed by reoxidation at low temperatures was implemented. During thermal treatment in forming gas, cobalt ferrite is reduced to an alloy of cobalt and iron. This leads to a powder consisting of barium titanate and cobalt iron alloy that was sintered under forming gas atmosphere. As metals, Co and Fe are not incorporated in the BaTiO<sub>3</sub> matrix, i.e. contaminations of this phase are effectively avoided.

It has to be noted that the density of the ceramic samples must be adjusted precisely. If the samples density is too low, the resulting cobalt ferrite / barium titanate composite will also possess a low density. If the density is too high, upon reoxidation, the cobalt iron alloy, reacting to cobalt ferrite, increases its volume and thus cracks and even powderization of the ceramic can occur.

During reoxidation of the ceramic bodies in air at 800 °C, a temperature much lower than the sintering temperature, the cobalt ferrite is formed again leading to magnetoelectric ceramics of barium titanate and cobalt ferrite. A scheme of this synthesis route is depicted in Figure 31.

XRD measurements proved phase-purity and SEM/EDX investigations revealed the desired 0-3 distribution of the cobalt ferrite in the barium titanate matrix with no indications for incorporation of Fe or Co in BaTiO<sub>3</sub>.

Impedance measurements show a Maxwell-Wagner like behavior as described before for barium titanate ferrite spinel composites. The loss tangents are quite low compared to

composites prepared in air pointing to a very low incorporation of cobalt and iron ions in the BaTiO<sub>3</sub> matrix.

The composites exhibit the expected magnetic properties with hystereses typically for cobalt ferrite. The observed saturation magnetizations agree well with the nominal CoFe<sub>2</sub>O<sub>4</sub> contents.

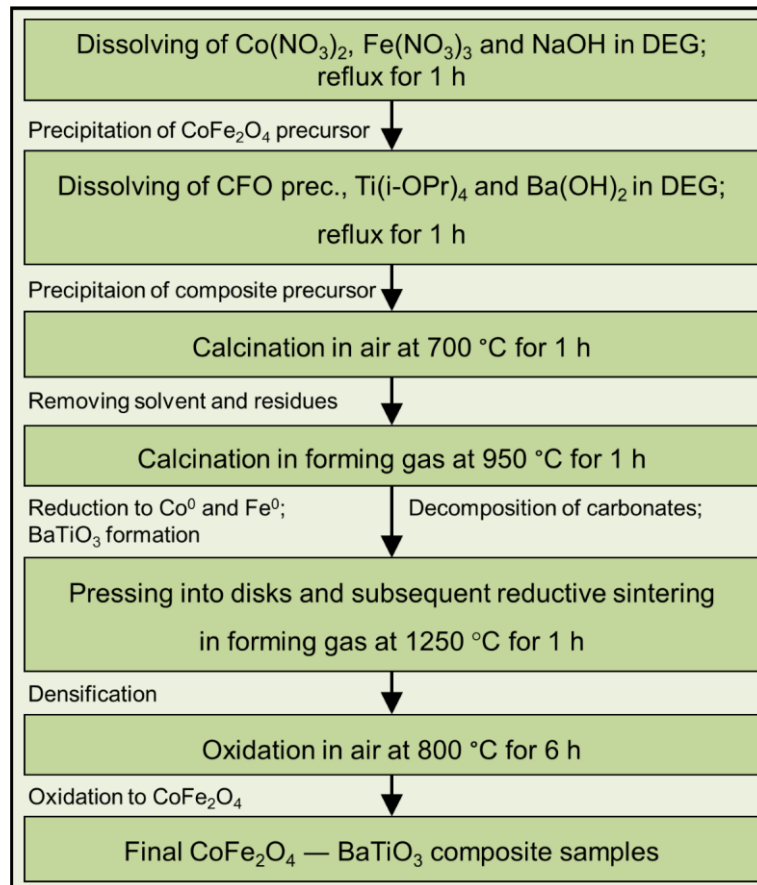


Figure 31: Synthesis scheme for BaTiO<sub>3</sub> – CoFe<sub>2</sub>O<sub>4</sub> composites with reductive sintering.[58]

To investigate the magnetoelectric properties of the composites the custom made device described in chapter 2.4. was used. The H<sub>DC</sub> dependent measurements reveal a hysteretic behavior of the magnetoelectric voltage coefficient  $\alpha_{ME}$  as shown in Figure 32. It could be shown that the magnetic and magnetoelectric coercivities are very different and that the maximum  $\alpha_{ME}$  values are dependent on the sweep direction of the applied magnetic field H<sub>DC</sub>.

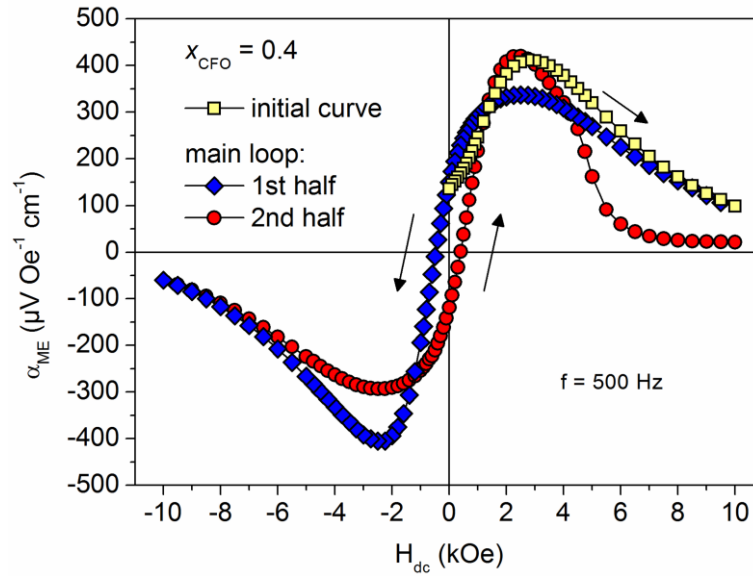


Figure 32:  $H_{DC}$  field dependent magneto-electric coefficient of a composite.[58]

The new approach of reductive sintering and reoxidation at low temperatures results in phase-pure samples with the desired 0-3 morphology and magnetic and electric properties characteristic for  $\text{CoFe}_2\text{O}_4$  and  $\text{BaTiO}_3$ . The magneto-electric hystereses exhibit a hitherto unknown dependence on the sweep direction of the magnetic DC field and coercivities that are different from the magnetic ones.

#### 4.6. Composites of $\text{Co}_{1/3}\text{Fe}_{2/3}$ and $\text{BaTiO}_3$ with 0-3 connectivity

In the course of the investigations discussed in the previous chapter, a new kind of composites was obtained, namely composites of barium titanate with cobalt iron alloy particles embedded. This kind of composites has been unknown in magnetoelectric literature and could be explained by the fact that, if the sintering is performed under oxidizing atmospheres, the alloy will not be stable and oxidizes. With the reductive sintering, introduced in [58], it is possible to preserve iron and cobalt in their metallic state while at the same time apply temperatures high enough to achieve a sufficient sintering of the  $\text{BaTiO}_3$  matrix yielding dense ceramics. But it has to be taken in mind that oxygen vacancies can occur in the barium titanate. These oxygen vacancies affect the ferroelectric properties of the barium titanate and have to be kept at a minimum.

A series of  $\text{Co}_{1/3}\text{Fe}_{2/3} - \text{BaTiO}_3$  composites was prepared and tested with focus on the magnetoelectric properties. The results have been published in [59].

It turned out that the composites possess appropriate electric and magnetic properties to achieve a magnetoelectric coupling. The  $H_{\text{DC}}$  dependent magnetoelectric investigations revealed a behavior completely different from the  $\text{CoFe}_2\text{O}_4/\text{BaTiO}_3$  composites. The magnetoelectric hystereses are shown in Figure 33. When electrically poled in the same direction, the sign of  $\alpha_{\text{ME}}$  is opposite to those of the composites containing  $\text{CoFe}_2\text{O}_4$  and also the course of the hystereses differs strongly. What's more, each sample had a different course of its hysteresis and thus the  $\text{Co}_{1/3}\text{Fe}_{2/3}$  content has a different influence on the magnetoelectric behavior than  $\text{CoFe}_2\text{O}_4$ . The cobalt ferrite content mainly influences the values of  $\alpha_{\text{ME}}$  but not the whole course of the hysteresis as with  $\text{Co}_{1/3}\text{Fe}_{2/3}$ .

With the new reductive sintering approach, a synthesis route for barium titanate composites with ferromagnetic alloys or elements was developed. It was shown that these kind of composites exhibit magnetoelectric coupling and they show a behavior, which is completely new in the field of magnetoelectrics, opening a door for an additional branch of research.

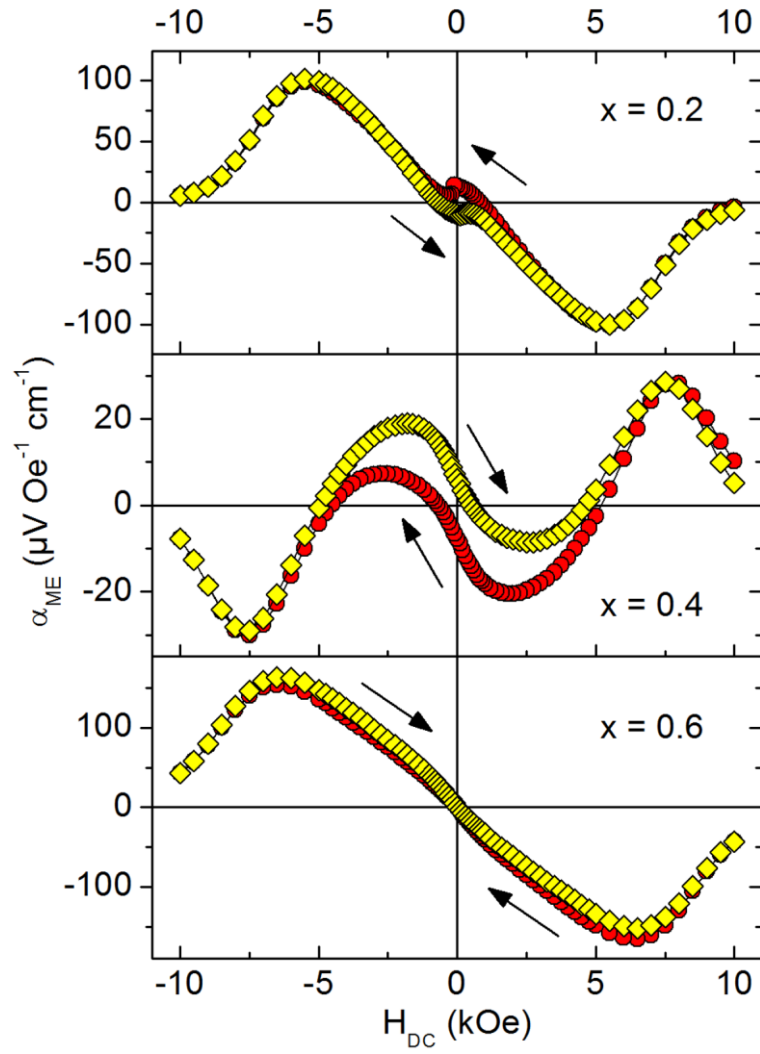


Figure 33  $H_{DC}$  field dependent magnetolectric coefficients of  $(Co_{1/3}Fe_{2/3})_x - (BaTiO_3)_{(1-x)}$  composites.[59]



## 5. Summary

This thesis covers the synthesis and investigation of multiferroic and magnetoelectric composites of barium titanate with ferrite spinels and a  $\text{Co}_{1/3}\text{Fe}_{2/3}$  alloy.

Different approaches were addressed to prepare ferrite spinels as composite precursors. While the mixed oxide method leads to well crystallized ferrite spinels with appropriate ferrimagnetic properties, the polyol mediated synthesis initially results in nearly amorphous nano sized powders with superparamagnetic properties. However, by additional heat treatment, the particle sizes increase and the magnetic properties can be tuned between superparamagnetic and ferrimagnetic behavior.

The polyol mediated method was used for the composites, because the small particle sizes ensure an evenly distribution of the ferrite and barium titanate in the precursor and thus in the final ceramics, although the high sintering temperatures lead to a massive particle growth

To prevent chemical reactions between barium titanate and the ferrite spinel, i.e. a substitution of the  $\text{BaTiO}_3$  matrix by cobalt and iron ions as well as the formation of barium hexaferrite, a reductive sintering procedure with subsequent reoxidation was developed. In this way, the side reactions were strongly suppressed, which is a key factor in the preparation of barium titanate – ferrite spinel composites from nanoscaled powders.

With this route – polyol mediated synthesis for ferrite and titanate with subsequent calcination and sintering in reductive atmosphere – two kinds of composites were prepared. The first set of composites consists of  $\text{CoFe}_2\text{O}_4$  as ferrimagnetic phase embedded in a ferroelectric matrix of  $\text{BaTiO}_3$ . The second kind of composites also contains  $\text{BaTiO}_3$  as matrix but involves the alloy  $\text{Co}_{1/3}\text{Fe}_{2/3}$  as ferromagnetic phase. Both sets of composites were prepared with different compositions. The composites were characterized by XRD, SEM, EDX, impedance spectroscopy, magnetic and magnetoelectric measurements. For the magnetoelectric investigations, a custom made measurement setup was developed. This allowed detailed investigations on the completely different magnetoelectric properties for both kinds of composites. The cobalt ferrite composites show magnetoelectric hystereses with maxima of  $\alpha_{\text{ME}}$  up to  $420 \mu\text{V Oe}^{-1} \text{cm}^{-1}$  that are dependent on the direction of the sweep of the magnetic field  $H_{\text{DC}}$ . The cobalt iron alloy composites possess  $\alpha_{\text{ME}}$  values of up to  $165 \mu\text{V Oe}^{-1} \text{cm}^{-1}$  and for each composition the course of the magnetoelectric hystereses is unique, which was not anticipated and is completely new to magnetoelectric research. The results have been published in peer reviewed journals.

## 6. References

- [1] N. Ortega, A. Kumar, J.F. Scott, R.S. Katiyar, Multifunctional magnetoelectric materials for device applications, *J. Phys.: Condens. Matter.* 27 (2015) 504002. doi:10.1088/0953-8984/27/50/504002.
- [2] N.A. Spaldin, M. Fiebig, The renaissance of magnetoelectric multiferroics, *Science.* 309 (2005) 391–392. doi:10.1126/science.1113357.
- [3] N.A. Hill, Why are there so few magnetic ferroelectrics?, *J. Phys. Chem. B.* 104 (2000) 6694–6709. doi:10.1021/jp000114x.
- [4] M.R. Koblischka, Multiferroika. Materialien mit ferroelektrischer und -magnetischer Ordnung, *Physik in Unserer Zeit.* 40 (2009) 132–137. doi:10.1002/piuz.200801188.
- [5] S. Dong, J.-M. Liu, S.-W. Cheong, Z. Ren, Multiferroic materials and magnetoelectric physics: symmetry, entanglement, excitation, and topology, *Advances in Physics.* 64 (2015) 519–626. doi:10.1080/00018732.2015.1114338.
- [6] J. van den Boomgaard, D.R. Terrell, R.A.J. Born, H.F.J.I. Giller, An in situ grown eutectic magnetoelectric composite material, *J. Mater. Sci.* 9 (1974) 1705–1709. doi:10.1007/BF00540770.
- [7] A.M.J.G. van Run, D.R. Terrell, J.H. Scholing, An in situ grown eutectic magnetoelectric composite material, *J. Mater. Sci.* 9 (1974) 1710–1714. doi:10.1007/BF00540771.
- [8] G. Schileo, Recent developments in ceramic multiferroic composites based on core/shell and other heterostructures obtained by sol–gel routes, *Prog. Solid State Chem.* 41 (2013) 87–98. doi:10.1016/j.progsolidstchem.2013.09.001.
- [9] R.E. Newnham, D.P. Skinner, L.E. Cross, Connectivity and piezoelectric-pyroelectric composites, *Mater. Res. Bull.* 13 (1978) 525–536. doi:10.1016/0025-5408(78)90161-7.
- [10] C.-W. Nan, M.I. Bichurin, S. Dong, D. Viehland, G. Srinivasan, Multiferroic magnetoelectric composites: Historical perspective, status, and future directions, *J. Appl. Phys.* 103 (2008) 031101. doi:10.1063/1.2836410.
- [11] C.-W. Nan, Magnetoelectric effect in composites of piezoelectric and piezomagnetic phases, *Phys. Rev. B.* 50 (1994) 6082–6088. doi:10.1103/PhysRevB.50.6082.
- [12] R.C. Kambale, D.-Y. Jeong, J. Ryu, Current status of magnetoelectric composite thin/thick films, *Advances in Condensed Matter Physics.* 2012 (2012) 1–15. doi:10.1155/2012/824643.
- [13] J. Ma, J. Hu, Z. Li, C.-W. Nan, Recent progress in multiferroic magnetoelectric composites: from bulk to thin films, *Adv. Mater.* 23 (2011) 1062–1087. doi:10.1002/adma.201003636.
- [14] M.M. Vijatović, J.D. Bobić, B.D. Stojanović, History and challenges of barium titanate: Part I, *Science of Sintering.* 40 (2008) 155–165.
- [15] M.M. Vijatović, J.D. Bobić, B.D. Stojanović, History and challenges of barium titanate: Part II, *Science of Sintering.* 40 (2008) 235–244.
- [16] D.S. Mathew, R.-S. Juang, An overview of the structure and magnetism of spinel ferrite nanoparticles and their synthesis in microemulsions, *Chemical Engineering Journal.* 129 (2007) 51–65. doi:10.1016/j.cej.2006.11.001.
- [17] M.R. De Guire, R.C. O’Handley, G. Kalonji, The cooling rate dependence of cation distributions in  $\text{CoFe}_2\text{O}_4$ , *J. Appl. Phys.* 65 (1989) 3167–3172. doi:10.1063/1.342667.
- [18] W.P. Osmond, The magnetic structure of spinels containing paramagnetic octahedral cations but diamagnetic tetrahedral cations, *Proc. Phys. Soc.* 85 (1965) 1191. doi:10.1088/0370-1328/85/6/318.
- [19] E. Riedel, C. Janiak, *Anorganische Chemie*, 7. Aufl, de Gruyter, Berlin, 2007.
- [20] J.M.D. Coey, *Magnetism and magnetic materials*, 1st ed., Cambridge University Press, 2010.
- [21] T. Yao, O. Imafuji, H. Jinno, EXAFS study of cation distribution in nickel aluminate ferrites, *Journal of the American Ceramic Society.* 74 (1991) 314–317.

- [22] T. Tangcharoen, W. Klysubun, C. Kongmark, W. Pecharapa, Synchrotron X-ray absorption spectroscopy and magnetic characteristics studies of metal ferrites (metal = Ni, Mn, Cu) synthesized by sol-gel auto-combustion method, *Phys. Status Solidi A*. 211 (2014) 1903–1911. doi:10.1002/pssa.201330477.
- [23] A. Yang, V.G. Harris, S. Calvin, X. Zuo, C. Vittoria, Extended X-ray absorption fine structure analysis of cation distribution in  $\text{MnFe}_2\text{O}_4$  single crystal films and artificial ferrite structures, *IEEE Transactions on Magnetics*. 40 (2004) 2802–2804. doi:10.1109/TMAG.2004.832246.
- [24] H.J. Lee, G. Kim, D.H. Kim, J.-S. Kang, C.L. Zhang, S.-W. Cheong, J.H. Shim, S. Lee, H. Lee, J.-Y. Kim, B.H. Kim, B.I. Min, Valence states and occupation sites in  $(\text{Fe,Mn})_3\text{O}_4$  spinel oxides investigated by soft x-ray absorption spectroscopy and magnetic circular dichroism, *J. Phys.: Condens. Matter*. 20 (2008) 295203. doi:10.1088/0953-8984/20/29/295203.
- [25] A. Yang, C.N. Chinnasamy, J.M. Greneche, Y. Chen, S.D. Yoon, Z. Chen, K. Hsu, Z. Cai, K. Ziemer, C. Vittoria, V.G. Harris, Enhanced Néel temperature in Mn ferrite nanoparticles linked to growth-rate-induced cation inversion, *Nanotechnology*. 20 (2009) 185704. doi:10.1088/0957-4484/20/18/185704.
- [26] H.S.C. O'Neill, H. Annersten, D. Virgo, The temperature dependence of the cation distribution in magnesioferrite ( $\text{MgFe}_2\text{O}_4$ ) from powder XRD structural refinements and Mössbauer spectroscopy, *Am. Mineral*. 77 (1992) 725–740. doi:http://www.minsocam.org/ammin/AM77/AM77\_725.pdf.
- [27] E. Wieser, H. Schröder, K. Kleinstück, A contribution to the magnetic structure of  $\text{MgFe}_2\text{O}_4$  by neutron diffraction and Mössbauer effect, *Physica Status Solidi (A)*. 1 (1970) 749–755.
- [28] W. Schiessl, W. Potzel, H. Karzel, M. Steiner, G.M. Kalvius, A. Martin, M.K. Krause, I. Halevy, J. Gal, W. Schäfer, others, Magnetic properties of the  $\text{ZnFe}_2\text{O}_4$  spinel, *Physical Review B*. 53 (1996) 9143.
- [29] T. Abbas, Y. Khan, M. Ahmad, S. Anwar, X-ray diffraction study of the cation distribution in the Mn-Zn-ferrites, *Solid State Communications*. 82 (1992) 701–703.
- [30] X.-X. Tang, A. Manthiram, J.B. Goodenough, Copper ferrite revisited, *Journal of Solid State Chemistry*. 79 (1989) 250–262. doi:10.1016/0022-4596(89)90272-7.
- [31] A.M. Balagurov, I.A. Bobrikov, V.Y. Pomjakushin, D.V. Sheptyakov, V.Y. Yushankhai, Interplay between structural and magnetic phase transitions in copper ferrite studied with high-resolution neutron diffraction, *Journal of Magnetism and Magnetic Materials*. 374 (2015) 591–599. doi:10.1016/j.jmmm.2014.08.092.
- [32] N.M. Deraz, Size and crystallinity-dependent magnetic properties of copper ferrite nanoparticles, *Journal of Alloys and Compounds*. 501 (2010) 317–325. doi:10.1016/j.jallcom.2010.04.096.
- [33] R. Köferstein, T. Walther, D. Hesse, S.G. Ebbinghaus, Crystallite-growth, phase transition, magnetic properties, and sintering behaviour of nano- $\text{CuFe}_2\text{O}_4$  powders prepared by a combustion-like process, *J. Solid State Chem*. 213 (2014) 57–64. doi:10.1016/j.jssc.2014.02.010.
- [34] J. van den Boomgaard, A.M.J.G. van Run, J.V. Suchtelen, Piezoelectric-piezomagnetic composites with magnetoelectric effect, *Ferroelectrics*. 14 (1976) 727–728. doi:10.1080/00150197608236711.
- [35] J. van den Boomgaard, R. a. J. Born, A sintered magnetoelectric composite material  $\text{BaTiO}_3\text{-Ni}(\text{Co, Mn})\text{Fe}_2\text{O}_4$ , *J Mater Sci*. 13 (1978) 1538–1548. doi:10.1007/BF00553210.
- [36] J. van den Boomgaard, A.M.J.G. Van Run, J. Van Suchtelen, Magnetoelectricity in piezoelectric-magnetostrictive composites, *Ferroelectrics*. 10 (1976) 295–298. doi:10.1080/00150197608241997.

- [37] J. van den Boomgaard, A.M.J.G. van Run, Poling of a ferroelectric medium by means of a built-in space charge field, with special reference to sintered magnetoelectric composites, *Solid State Communications*. 19 (1976) 405–407. doi:10.1016/0038-1098(76)91177-7.
- [38] Y.Q. Dai, J.M. Dai, X.W. Tang, K.J. Zhang, X.B. Zhu, J. Yang, Y.P. Sun, Thickness effect on the properties of BaTiO<sub>3</sub>–CoFe<sub>2</sub>O<sub>4</sub> multilayer thin films prepared by chemical solution deposition, *Journal of Alloys and Compounds*. 587 (2014) 681–687. doi:10.1016/j.jallcom.2013.11.026.
- [39] B. Bajac, J. Vukmirovic, I. Tokic, S. Ognjanovic, V.V. Srdic, Synthesis and characterization of multilayered BaTiO<sub>3</sub>/NiFe<sub>2</sub>O<sub>4</sub> thin films, *Processing and Application of Ceramics*. 7 (2013) 15–20. doi:10.2298/PAC1301015B.
- [40] S.S. Kumbhar, M.A. Mahadik, V.S. Mohite, Y.M. Hunge, P.K. Chougule, K.Y. Rajpure, C.H. Bhosale, Fabrication of Ni<sub>0.4</sub>Zn<sub>0.6</sub>Fe<sub>2</sub>O<sub>4</sub>–BaTiO<sub>3</sub> bilayered thin films obtained by spray pyrolysis method for magnetoelectric (ME) effect measurement, *J Mater Sci: Mater Electron*. 27 (2016) 3799–3811. doi:10.1007/s10854-015-4225-3.
- [41] S. Geprägs, D. Mannix, M. Opel, S.T.B. Goennenwein, R. Gross, Converse magnetoelectric effects in Fe<sub>3</sub>O<sub>4</sub>/BaTiO<sub>3</sub> multiferroic hybrids, *Physical Review B*. 88 (2013). doi:10.1103/PhysRevB.88.054412.
- [42] J. Zhai, Z. Xing, S. Dong, J. Li, D. Viehland, Magnetoelectric Laminate Composites: An Overview, *J. Am. Chem. Soc.* 91 (2008) 351–358. doi:10.1111/j.1551-2916.2008.02259.x.
- [43] A. Khamkongkao, P. Jantaratana, C. Sirisathitkul, T. Yamwong, S. Maensiri, Frequency-dependent magnetoelectricity of CoFe<sub>2</sub>O<sub>4</sub>–BaTiO<sub>3</sub> particulate composites, *Trans. Nonferrous Met. Soc. China*. 21 (2011) 2438–2442. doi:10.1016/S1003-6326(11)61033-9.
- [44] M. Etier, V.V. Shvartsman, Y. Gao, J. Landers, H. Wende, D.C. Lupascu, Magnetoelectric effect in (0–3) CoFe<sub>2</sub>O<sub>4</sub>–BaTiO<sub>3</sub> (20/80) composite ceramics prepared by the organosol route, *Ferroelectrics*. 448 (2013) 77–85. doi:10.1080/00150193.2013.822292.
- [45] R.P. Mahajan, K.K. Patankar, M.B. Kothale, S.C. Chaudhari, V.L. Mathe, S.A. Patil, Magnetoelectric effect in cobalt ferrite-barium titanate composites and their electrical properties, *Pramana*. 58 (2002) 1115–1124. doi:10.1007/s12043-002-0227-9.
- [46] V. Gorige, R. Kati, D.H. Yoon, P.S.A. Kumar, Strain mediated magnetoelectric coupling in a NiFe<sub>2</sub>O<sub>4</sub>–BaTiO<sub>3</sub> multiferroic composite, *J. Phys. D: Appl. Phys.* 49 (2016) 405001. doi:10.1088/0022-3727/49/40/405001.
- [47] J.-P. Zhou, L. Lv, Q. Liu, Y.-X. Zhang, P. Liu, Hydrothermal synthesis and properties of NiFe<sub>2</sub>O<sub>4</sub>@BaTiO<sub>3</sub> composites with well-matched interface, *Sci. Technol. Adv. Mater.* 13 (2012) 045001. doi:10.1088/1468-6996/13/4/045001.
- [48] A. Gupta, R. Chatterjee, Dielectric and magnetoelectric properties of BaTiO<sub>3</sub>–Co<sub>0.6</sub>Zn<sub>0.4</sub>Fe<sub>1.7</sub>Mn<sub>0.3</sub>O<sub>4</sub> composite, *J. Eur. Ceram. Soc.* 33 (2013) 1017–1022. doi:10.1016/j.jeurceramsoc.2012.11.003.
- [49] K.K. Patankar, S.A. Patil, K.V. Sivakumar, R.P. Mahajan, Y.D. Kolekar, M.B. Kothale, AC conductivity and magnetoelectric effect in CuFe<sub>1.6</sub>Cr<sub>0.4</sub>O<sub>4</sub>–BaTiO<sub>3</sub> composite ceramics., *Mater. Chem. Phys.* 65 (2000) 97–102. doi:10.1016/S0254-0584(00)00216-9.
- [50] R.-F. Zhang, C.-Y. Deng, L. Ren, Z. Li, J.-P. Zhou, Dielectric, ferromagnetic and magnetoelectric properties of BaTiO<sub>3</sub>–Ni<sub>0.7</sub>Zn<sub>0.3</sub>Fe<sub>2</sub>O<sub>4</sub> composite ceramics, *Materials Research Bulletin*. 48 (2013) 4100–4104. doi:10.1016/j.materresbull.2013.06.026.
- [51] D.C. Lupascu, H. Wende, M. Etier, A. Nazrabi, I. Anusca, H. Trivedi, V.V. Shvartsman, J. Landers, S. Salamon, C. Schmitz-Antoniak, Measuring the magnetoelectric effect across scales, *GAMM-Mitteilungen*. 38 (2015) 25–74. doi:10.1002/gamm.201510003.
- [52] K.H.J. Buschow, ed., *Handbook of magnetic materials.*, 1. ed, Elsevier, North-Holland, Amsterdam, 2011.
- [53] R.S. Singh, T. Bhimasankaram, G.S. Kumar, S.V. Suryanarayana, Dielectric and magnetoelectric properties of Bi<sub>5</sub>FeTi<sub>3</sub>O<sub>15</sub>, *Solid State Communications*. 91 (1994) 567–569. doi:10.1016/0038-1098(94)90376-X.

- [54] J.-P. Rivera, On definitions, units, measurements, tensor forms of the linear magnetoelectric effect and on a new dynamic method applied to Cr-Cl boracite, *Ferroelectrics*. 161 (1994) 165–180. doi:10.1080/00150199408213365.
- [55] M.M. Kumar, A. Srinivas, S.V. Suryanarayana, G.S. Kumar, T. Bhimasankaram, An experimental setup for dynamic measurement of magnetoelectric effect, *Bull Mater Sci*. 21 (1998) 251–255. doi:10.1007/BF02744978.
- [56] G.V. Duong, R. Groessinger, M. Schoenhardt, D. Bueno-Basques, The lock-in technique for studying magnetoelectric effect, *Journal of Magnetism and Magnetic Materials*. 316 (2007) 390–393. doi:10.1016/j.jmmm.2007.03.185.
- [57] T. Walther, N. Quandt, R. Köferstein, R. Roth, M. Steimecke, S.G. Ebbinghaus, BaTiO<sub>3</sub>–CoFe<sub>2</sub>O<sub>4</sub>–BaTiO<sub>3</sub> trilayer composite thin films prepared by chemical solution deposition, *J. Eur. Ceram. Soc.* 36 (2016) 559–565. doi:10.1016/j.jeurceramsoc.2015.10.009.
- [58] T. Walther, U. Straube, R. Köferstein, S.G. Ebbinghaus, Hysteretic magnetoelectric behavior of CoFe<sub>2</sub>O<sub>4</sub>–BaTiO<sub>3</sub> composites prepared by reductive sintering and reoxidation, *J. Mater. Chem. C*. 4 (2016) 4792–4799. doi:10.1039/C6TC00995F.
- [59] T. Walther, R. Köferstein, S.G. Ebbinghaus, Novel magnetoelectric composites of cobalt iron alloy and barium titanate, *J. Am. Ceram. Soc.* 100 (2017) 1502–1507. doi:10.1111/jace.14744.
- [60] Quantum Design, Application Note 1084-403 Format of AC Transport Measurement Data Files, (2009).
- [61] Quantum Design, Application Note 1070-207 Using PPMS Superconducting Magnets at Low Fields, (2009).
- [62] F. Fievet, F. Fievet-Vincent, J.-P. Lagier, B. Dumont, M. Figlarz, Controlled nucleation and growth of micrometre-size copper particles prepared by the polyol process, *J. Mater. Chem.* 3 (1993) 627–632. doi:10.1039/JM9930300627.
- [63] J. Merikhi, H.-O. Jungk, C. Feldmann, Sub-micrometer CoAl<sub>2</sub>O<sub>4</sub> pigment particles — synthesis and preparation of coatings, *J. Mater. Chem.* 10 (2000) 1311–1314. doi:10.1039/A910201I.
- [64] M. Siemons, T. Weirich, J. Mayer, U. Simon, Preparation of nanosized perovskite-type oxides via polyol method, *Z. Anorg. Allg. Chem.* 630 (2004) 2083–2089. doi:10.1002/zaac.200400300.
- [65] D. Caruntu, Y. Remond, N.H. Chou, M.-J. Jun, G. Caruntu, J. He, G. Goloverda, C. O'Connor, V. Kolesnichenko, Reactivity of 3d transition metal cations in diethylene glycol solutions. synthesis of transition metal ferrites with the structure of discrete nanoparticles complexed with long-chain carboxylate anions, *Inorg. Chem.* 41 (2002) 6137–6146. doi:10.1021/ic025664j.
- [66] R.P. Kreh, R.M. Spotnitz, J.T. Lundquist, Mediated electrochemical synthesis of aromatic aldehydes, ketones, and quinones using ceric methanesulfonate, *The Journal of Organic Chemistry*. 54 (1989) 1526–1531.
- [67] S. Brunauer, P.H. Emmett, E. Teller, Adsorption of gases in multimolecular layers, *Journal of the American Chemical Society*. 60 (1938) 309–319.
- [68] P. Scherrer, Bestimmung der Grösse und der inneren Struktur von Kolloidteilchen mittels Röntgenstrahlen., *Nachrichten von Der Gesellschaft Der Wissenschaften Zu Göttingen*. (1918) 98–100.
- [69] J.L. Dormann, D. Fiorani, E. Tronc, Magnetic relaxation in fine-particle systems, in: I. Prigogine, S.A. Rice (Eds.), *Advances in Chemical Physics*, John Wiley & Sons, Inc., 1997: p. 288pp. doi:10.1002/9780470141571.ch4.
- [70] K.V.P.M. Shafi, A. Gedanken, R. Prozorov, J. Balogh, Sonochemical preparation and size-dependent properties of nanostructured CoFe<sub>2</sub>O<sub>4</sub> particles, *Chemistry of Materials*. 10 (1998) 3445–3450. doi:10.1021/cm980182k.

- [71] S. Ammar, A. Helfen, N. Jouini, F. Fiévet, I. Rosenman, F. Villain, P. Molinié, M. Danot, Magnetic properties of ultrafine cobalt ferrite particles synthesized by hydrolysis in a polyol medium, *J. Mater. Chem.* 11 (2001) 186–192. doi:10.1039/B003193N.
- [72] C.N. Chinnasamy, A. Narayanasamy, N. Ponpandian, K. Chattopadhyay, H. Guerault, J.M. Greneche, Magnetic properties of nanostructured ferrimagnetic zinc ferrite, *Journal of Physics: Condensed Matter.* 12 (2000) 7795.
- [73] S. Singhal, J. Singh, S.K. Barthwal, K. Chandra, Preparation and characterization of nanosize nickel-substituted cobalt ferrites ( $\text{Co}_{1-x}\text{Ni}_x\text{Fe}_2\text{O}_4$ ), *Journal of Solid State Chemistry.* 178 (2005) 3183–3189. doi:10.1016/j.jssc.2005.07.020.
- [74] S. Kubickova, J. Vejpravova, P. Holec, D. Niznansky, Correlation of crystal structure and magnetic properties of  $\text{Co}_{(1-x)}\text{Ni}_x\text{Fe}_2\text{O}_4/\text{SiO}_2$  nanocomposites, *Journal of Magnetism and Magnetic Materials.* 334 (2013) 102–106. doi:10.1016/j.jmmm.2013.01.005.
- [75] R. Pązik, A. Zięcina, E. Zachanowicz, M. Małecka, B. Poźniak, J. Miller, Z. Śniadecki, N. Pierunek, B. Idzikowski, L. Mrówczyńska, A. Ekner-Grzyb, R.J. Wiglusz, Synthesis, structural features, cytotoxicity, and magnetic properties of colloidal ferrite spinel  $\text{Co}_{1-x}\text{Ni}_x\text{Fe}_2\text{O}_4$  ( $0.1 \leq x \leq 0.9$ ) nanoparticles, *European Journal of Inorganic Chemistry.* 2015 (2015) 4750–4760. doi:10.1002/ejic.201500668.
- [76] U. Wongpratad, S. Maensiri, E. Swatsitang, EXAFS analysis of cations distribution in structure of  $\text{Co}_{1-x}\text{Ni}_x\text{Fe}_2\text{O}_4$  nanoparticles obtained by hydrothermal method in aloe vera extract solution, *Applied Surface Science.* 380 (2016) 60–66. doi:10.1016/j.apsusc.2016.02.082.
- [77] J. Suntivich, H.A. Gasteiger, N. Yabuuchi, H. Nakanishi, J.B. Goodenough, Y. Shao-Horn, Design principles for oxygen-reduction activity on perovskite oxide catalysts for fuel cells and metal–air batteries, *Nature Chemistry.* 3 (2011) 546–550. doi:10.1038/nchem.1069.
- [78] Y. Liang, Y. Li, H. Wang, J. Zhou, J. Wang, T. Regier, H. Dai,  $\text{Co}_3\text{O}_4$  nanocrystals on graphene as a synergistic catalyst for oxygen reduction reaction, *Nat. Mater.* 10 (2011) 780–786. doi:10.1038/nmat3087.
- [79] G. Seiffarth, M. Steimecke, T. Walther, M. Kühhirt, S. Rümmler, M. Bron, Mixed transition metal oxide supported on nitrogen doped carbon nanotubes – a simple bifunctional electrocatalyst studied with scanning electrochemical microscopy, *Electroanalysis.* 28 (2016) 2335–2345. doi:10.1002/elan.201600254.

## **Appendix**

- A1** BaTiO<sub>3</sub>–CoFe<sub>2</sub>O<sub>4</sub>–BaTiO<sub>3</sub> trilayer composite thin films prepared by chemical solution deposition
- A2** Hysteretic magnetoelectric behavior of CoFe<sub>2</sub>O<sub>4</sub>–BaTiO<sub>3</sub> composites prepared by reductive sintering and reoxidation
- A3** Novel magnetoelectric composites of cobalt iron alloy and barium titanate

**A1** BaTiO<sub>3</sub>–CoFe<sub>2</sub>O<sub>4</sub>–BaTiO<sub>3</sub> trilayer composite thin films prepared by chemical solution deposition

Reprinted with the permission of Elsevier Ltd.





# BaTiO<sub>3</sub>–CoFe<sub>2</sub>O<sub>4</sub>–BaTiO<sub>3</sub> trilayer composite thin films prepared by chemical solution deposition



Till Walther<sup>a</sup>, Norman Quandt<sup>a</sup>, Roberto Köferstein<sup>a</sup>, Robert Roth<sup>b</sup>, Matthias Steimecke<sup>c</sup>, Stefan G. Ebbinghaus<sup>a,\*</sup>

<sup>a</sup> Institute of Chemistry, Inorganic Chemistry, Martin Luther University Halle-Wittenberg, Kurt Mothes Strasse 2, 06120 Halle, Germany

<sup>b</sup> Institute of Physics, Martin Luther University Halle-Wittenberg, von Danckelmann Platz 3, 06120 Halle, Germany

<sup>c</sup> Institute of Chemistry, Industrial Chemistry, Martin Luther University Halle-Wittenberg, von Danckelmann Platz 4, 06120 Halle, Germany

## ARTICLE INFO

### Article history:

Received 22 July 2015

Received in revised form 7 October 2015

Accepted 9 October 2015

Available online 26 October 2015

### Keywords:

Multiferroics

Thin films

BaTiO<sub>3</sub>

CoFe<sub>2</sub>O<sub>4</sub>

Spin coating

## ABSTRACT

Multiferroic BaTiO<sub>3</sub>–CoFe<sub>2</sub>O<sub>4</sub>–BaTiO<sub>3</sub> thin films were synthesized by spin coating of Co(NO<sub>3</sub>)<sub>2</sub>–Fe(NO<sub>3</sub>)<sub>3</sub> and Ba(OAc)<sub>2</sub>–Ti(*i*-OPr)<sub>4</sub> dissolved in a mixture of acetic acid and dimethylformamide. Stepwise thermal treatment at 200, 400 and 800 °C led to the desired phases. The phase formation process was monitored by thermoanalytic, XRD, IR and Raman measurements. SEM was used to characterize the structure and thickness of each layer. Two samples with different thicknesses of perovskite and spinel layers are discussed. Sample **1** consists of 120 nm CoFe<sub>2</sub>O<sub>4</sub> between two 70 nm BaTiO<sub>3</sub> layers. For sample **2**, the 90 nm BaTiO<sub>3</sub> top and bottom layers are enclosing 220 nm CoFe<sub>2</sub>O<sub>4</sub>. The surface qualities were determined by AFM indicating rms roughness values of about 4 nm. Magnetic investigations reveal slightly anisotropic behavior. Polarization measurements show hysteresis loops ( $P_{S(\max)} = 29 \mu\text{C cm}^{-2}$ ;  $P_{R(\max)} = 17 \mu\text{C cm}^{-2}$ ) with switching peaks at the corresponding coercive fields.

© 2015 Elsevier Ltd. All rights reserved.

## 1. Introduction

Multiferroics are compounds that exhibit at least two ferroic order phenomena [1]. The coupling between ferroic orders, especially the ability to change the electric polarization by an external magnetic field, i.e., the magneto-electric effect (ME), has high potential to be used in new devices and applications [2,3]. Different possibilities of connections between electric and magnetic phases in multiferroic composites have been suggested and investigated [4,5]. Whereas magneto-electric coefficients of particulate composites (0–3) are often significantly lower than predicted by theory, laminated thick film structures (2–2 composites) of various piezoelectric and magnetostrictive phases have been reported to show high ME voltage coefficients [6,7]. Over the past years the focus of the development of layer-structured multiferroics shifted from epoxy glued composites to submicron- and finally nano-scaled samples with direct interfaces between magnetostrictive and piezoelectric phase [8]. Generally two basic principles are used for the preparation of thin layered oxides. The first one is the gas phase deposition, used e.g., in chemical vapor deposition (CVD),

pulsed laser deposition (PLD) or molecular beam epitaxy (MBE). The second principle is the deposition from a liquid phase like electrochemical deposition, chemical solution deposition (CSD) and co-precipitation methods (e.g., sol–gel). The latter two methods generally comprise a coating step like dip or spin coating. Although deposition from the gas phase often leads to very thin and epitaxial films of the ferroelectric and magnetic phase as well as high-quality interfaces, the needed machinery is quite expensive and challenging to operate. In contrast, with liquid phase deposition methods the growth control may be limited but the equipment is comparatively inexpensive and easy to handle. Thus, a variety of sample compositions and synthesis conditions can be screened quite fast.

Here, we report on BTO-CFO-BTO layer-structured 2–2 composites consisting of ferroelectric BaTiO<sub>3</sub> and ferrimagnetic CoFe<sub>2</sub>O<sub>4</sub> prepared by a chemical solution spin coating approach. Spin coating has been frequently described in literature, e.g., [9–15] but has not yet been investigated systematically for CoFe<sub>2</sub>O<sub>4</sub>–BaTiO<sub>3</sub> composites [16].

The optimum synthesis temperatures for the formation of the perovskite and spinel were determined via thermogravimetric experiments and the phase evolution and purity of the composites was confirmed by XRD, IR and Raman measurements. SEM and AFM images were used to examine the thickness, morphology and surface quality of the samples. Magnetic and electric measurements

\* Corresponding author. Tel.: +49 345 5525870.

E-mail address: [stefan.ebbinghaus@chemie.uni-halle.de](mailto:stefan.ebbinghaus@chemie.uni-halle.de) (S.G. Ebbinghaus).

show ferroelectric and hard magnetic behavior for the composite thin films.

## 2. Experimental

### 2.1. Material preparation

All chemicals were used without further purification if not stated otherwise.  $2 \times 2$  cm pieces of Pt-sputtered, 100-oriented Si-wafers (Micromotive GmbH) were chosen as substrates. An alkaline tenside solution (Hellmanex® III) was used for cleaning the substrates. For the  $\text{CoFe}_2\text{O}_4$  layers, stoichiometric amounts of  $\text{Co}(\text{NO}_3)_2 \cdot 6\text{H}_2\text{O}$  and  $\text{Fe}(\text{NO}_3)_3 \cdot 9\text{H}_2\text{O}$  (both Sigma–Aldrich) were dissolved in a mixture of acetic acid and dimethylformamide (DMF) (volume ratio: 1:3) with a concentration of  $[\text{Co}^{2+}] = 0.3 \text{ mol l}^{-1}$ . For the  $\text{BaTiO}_3$  layers, initial  $\text{Ba}^{2+}$  and  $\text{Ti}^{4+}$  solutions were prepared separately.  $\text{Ba}(\text{CH}_3\text{COO})_2$  (Sigma–Aldrich) was dissolved in acetic acid at  $60^\circ\text{C}$  and then cooled to room temperature. Distilled  $\text{Ti}(\text{i-OPr})_4$  (Alfa Aesar) was dissolved in a mixture of acetic acid and DMF (volume ratio: 4:9).  $\text{Ba}^{2+}$  and  $\text{Ti}^{4+}$  solutions were combined prior to the coating process resulting in a final solution with  $[\text{Ba}^{2+}] = [\text{Ti}^{4+}] = 0.3 \text{ mol l}^{-1}$ . The cleaned substrates were covered with the corresponding precursor solution and spin coated for 1 min at 4000 rpm with a modular spin processor WS-650-23NPP from Laurell Technologies Corporation. After a drying step at  $200^\circ\text{C}$  the samples were calcined at  $400^\circ\text{C}$  for 5 min followed by a phase formation step at  $800^\circ\text{C}$  in static air for 5 min. After cooling down to room temperature, the next layer was coated. This process was repeated until the desired number of layers was accomplished. Finally, the samples were annealed at  $800^\circ\text{C}$  in static air for one hour to increase the crystallinity and slowly cooled down to room temperature.

Two samples with different numbers of layers and hence film thicknesses are discussed in this paper. Sample 1 consists of 3  $\text{BaTiO}_3$  layers, followed by 5 layers  $\text{CoFe}_2\text{O}_4$  topped with 3 layers  $\text{BaTiO}_3$ . The 2 is built up from 4 bottom  $\text{BaTiO}_3$  layers, 8 middle  $\text{CoFe}_2\text{O}_4$  and 4 top  $\text{BaTiO}_3$  layers. A flowchart of the coating process and schematic sample structures is shown in Fig. 1.

### 2.2. Characterization

Thermoanalytic measurements in flowing synthetic air (flow rate  $20 \text{ ml min}^{-1}$ , heating rate  $10 \text{ K min}^{-1}$ ) of the predried ( $200^\circ\text{C}$ ) solutions were performed using a Netzsch STA 449 system. X-ray diffraction patterns were recorded in locked uncoupled mode ( $\theta/\theta$  scan with  $2.5^\circ$  offset between X-ray tube/detector and the normal of the sample surface) on a Bruker AXS D8Advance

diffractometer operating with  $\text{CuK}\alpha$  radiation. Fourier transformed infrared (FT-IR) spectra were collected at room temperature using a Bruker Tensor 27 spectrometer equipped with a diamond ATR unit. A Raman microscope consisting of an InVia Raman spectrometer (Renishaw) with  $1800 \text{ lmm}^{-1}$  grating and a 532 nm laser (Cobolt CWD PSS, 100 mW, Renishaw) was used to obtain spectra in the region of  $200\text{--}800 \text{ cm}^{-1}$ . The laser power was fixed at 5% with an exposure time of 60 s. Cross sectional scanning electron microscope images from freshly fractured samples were taken with a Philips ESEM XL30 FEG. Topographical measurements were performed using an atomic force microscope (AFM) MFP3D (Asylum Research Oxford Instruments) equipped with commercial super-sharp silicon tips (type SSS-NCL, Nanosensors) operating in tapping mode. Magnetic measurements were carried out using a Quantum Design PPMS9. Hysteresis loops were measured at 300 K with cycling of the magnetic field between 90 and  $-90 \text{ kOe}$ . For anisotropic investigations the sample plane was aligned either parallel or perpendicular to the magnetic field. Data sets were corrected for the diamagnetic contributions of the substrate and the sample holder by a linear fit of the ranges  $\pm 50\text{--}90 \text{ kOe}$ . Magnetization values are normalized to the  $\text{CoFe}_2\text{O}_4$  volume fractions. For ferroelectric measurements the Pt layer on the substrate was used as bottom electrode. For top electrodes  $80 \times 80 \mu\text{m}^2$  copper films (40 nm) were evaporated on the sample surfaces and covered with gold (20 nm). Ferroelectric polarization and leakage currents were measured as a function of applied voltage ( $\pm 25 \text{ V}$ ) with a TF2000 Analyzer from aixACCT Systems GmbH.

## 3. Results and discussion

### 3.1. Thermal analysis

Drying of the  $\text{Ba}^{2+}/\text{Ti}^{4+}$  solution at  $200^\circ\text{C}$  for 1 h in air resulted in a yellowish powder. TG and DTA investigations up to  $1000^\circ\text{C}$  in flowing air (heating rate:  $10 \text{ K min}^{-1}$ ) were carried out on this powder (Fig. 2). The endothermic weight loss of roughly 6.5% in the temperature range  $50\text{--}250^\circ\text{C}$  is due to the evaporation of remaining water from the sample. A series of exothermic reactions which can be assigned to the stepwise decomposition of the organic components starts at  $250^\circ\text{C}$  and is finished at  $750^\circ\text{C}$  with a total weight loss of 45.6%. No further weight change was detected up to  $1000^\circ\text{C}$ . The XRD measurement of the resulting white powder indicated phase-pure  $\text{BaTiO}_3$ .

Simultaneous TG and DTA investigations of the  $\text{Co}^{2+}/\text{Fe}^{3+}$  solution predried for 1 h at  $200^\circ\text{C}$  are shown in Fig. 3. The endothermic signal in the DTA curve below ca.  $200^\circ\text{C}$  with a corresponding

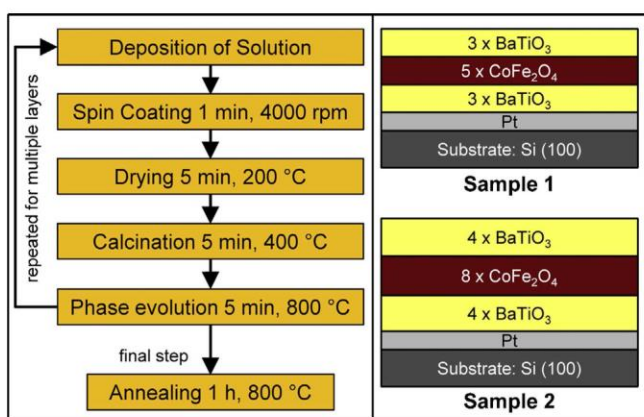


Fig. 1. Flowchart of the spin coating process (left) and schematic structure of samples 1 and 2 (right).

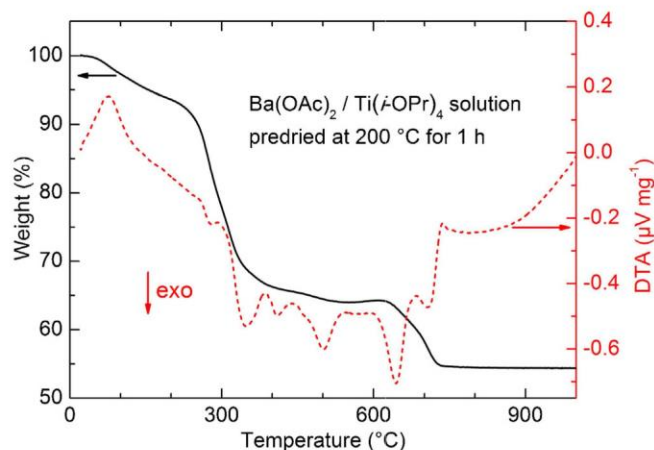
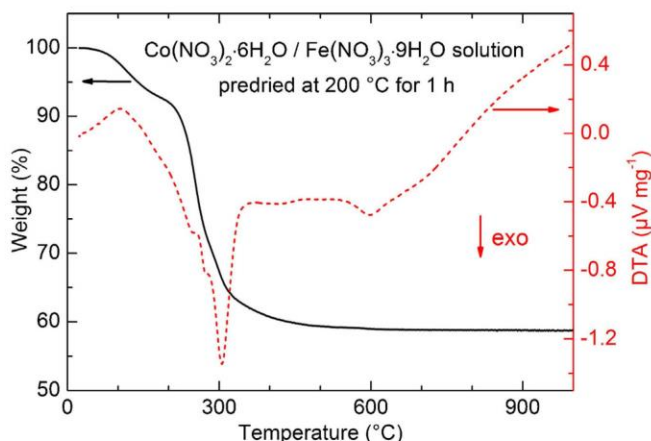


Fig. 2. Simultaneous TG and DTA investigations of predried solution of barium(II) acetate and titanium(IV) isopropoxide in acetic acid and DMF.



**Fig. 3.** Simultaneous TG and DTA investigations of the predried solution of cobalt(II) and iron(III) nitrate dissolved in acetic acid and DMF.

weight loss of 8.0% again can be assigned to the release of water. Strong exothermic DTA signals between 200 and roughly 370 °C are accompanied by an additional weight loss of 22.4%. A slight gradual weight change up to 600 °C leads to a total weight loss of 41.1%. The exothermic DTA signal at 600 °C (without significant weight change) most likely stems from the crystallization of the spinel phase. No further change in weight was detected up to 1000 °C and XRD measurements of the resulting dark powder indicated phase-pure  $\text{CoFe}_2\text{O}_4$ .

These thermal investigations show that for the used solutions a calcination temperature of 750 °C is sufficient to ensure the completion of the phase formation of both  $\text{BaTiO}_3$  and  $\text{CoFe}_2\text{O}_4$ .

### 3.2. XRD, IR and Raman

X-Ray diffractograms of **1** and **2** are shown in Fig. 4. All detected diffraction peaks can be assigned to cubic  $\text{CoFe}_2\text{O}_4$ ,  $\text{BaTiO}_3$  or the substrate [17]. From the measurements it cannot be differentiated between the cubic and tetragonal modification of  $\text{BaTiO}_3$  due to relatively small crystallites and thus broadened reflections [18]. The XRD measurements show that the coating process leads to phase-pure  $\text{BaTiO}_3$  and  $\text{CoFe}_2\text{O}_4$  layers without any secondary phases, such as  $\text{BaTi}_{14}\text{O}_{19}$  or  $\text{BaFe}_{12}\text{O}_{19}$ .

Infrared spectra of composites and single component film samples are shown in Fig. 5. Due to the small layer thickness and the diamond ATR set-up no transversal but only longitudinal vibrations were detected, known as Berreman effect [19]. Longitudinal

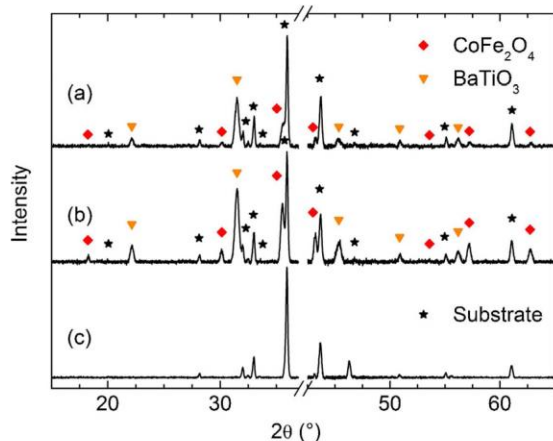


**Fig. 4.** X-ray diffraction patterns of (a) sample **1**, (b) sample **2** and (c) the uncoated, thermally treated substrate. An axis break was inserted at the Pt (1 1 1) peak.

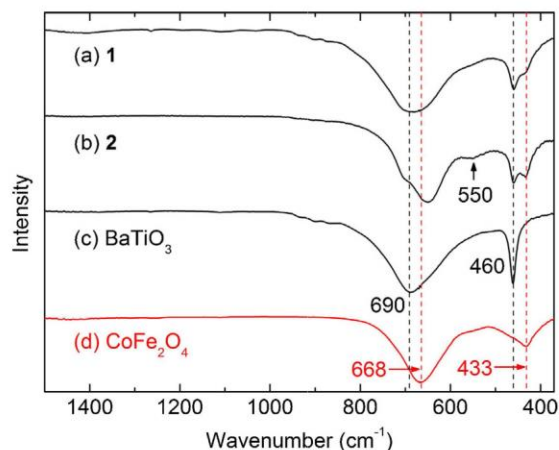


**Fig. 5.** FT-IR spectra (ATR-technique) of samples **1** (a) and **2** (b) compared to films of pure  $\text{BaTiO}_3$  (c) and  $\text{CoFe}_2\text{O}_4$  (d).

metal–oxygen bond vibration bands at 460 and 690  $\text{cm}^{-1}$  can be assigned to cubic or tetragonal  $\text{BaTiO}_3$  [20] while the bands at 433 and 668  $\text{cm}^{-1}$  belong to cubic  $\text{CoFe}_2\text{O}_4$  [21], respectively. Due to the thicker  $\text{CoFe}_2\text{O}_4$  layer in sample **2** one additional weak transversal vibration at 550  $\text{cm}^{-1}$  was detected [22].

In Fig. 6 confocal Raman spectra of the composite samples are shown. At the laser wavelength of 532 nm,  $\text{BaTiO}_3$  possesses a relatively low absorption (<15%) [23], compared to  $\text{CoFe}_2\text{O}_4$  (>90%) [24]. Hence only Raman active modes of  $\text{CoFe}_2\text{O}_4$  can be seen in the spectra. In the measured range from 200 to 800  $\text{cm}^{-1}$  there are five intensity maxima. All of them are in accordance with literature data for  $\text{CoFe}_2\text{O}_4$  and  $\text{BaTiO}_3$ – $\text{CoFe}_2\text{O}_4$  thin film composites [25,26]. Raman active modes in ferrite spinels have  $A_{1g}$ ,  $E_g$  and  $3 \times T_{2g}$  symmetry. The maximum at 302  $\text{cm}^{-1}$  can be assigned to the  $E_g$  mode, the maxima at 468 and 567  $\text{cm}^{-1}$  to two of the  $T_{2g}$  modes and the maximum at 690  $\text{cm}^{-1}$  to the  $A_{1g}$  mode. A third  $T_{2g}$  mode with a very small intensity should be located close to 210  $\text{cm}^{-1}$  but was not detected in the obtained spectra. On the other hand, due to partial cation distribution between octahedral and tetrahedral sites another Raman active mode with  $A_{1g}$  character appears at 616  $\text{cm}^{-1}$ , in accordance with the partial occupation of the tetrahedral sites by  $\text{Fe}^{3+}$  ions in inverse spinel ferrites [27–29].

### 3.3. SEM and AFM

Cross-section and surface scanning electron micrographs were taken for both samples (Figs. 7 and 8). The SEM images of sample

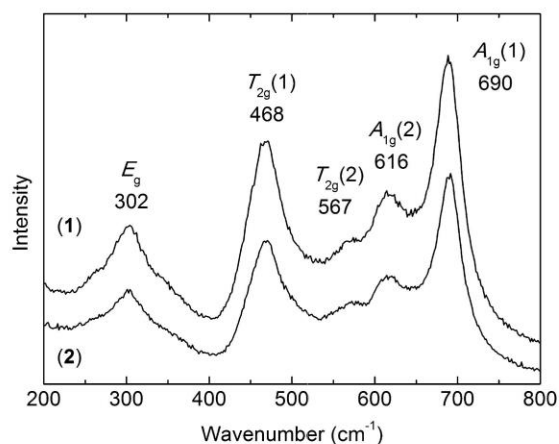


**Fig. 6.** Confocal Raman spectra of samples **1** and **2**.

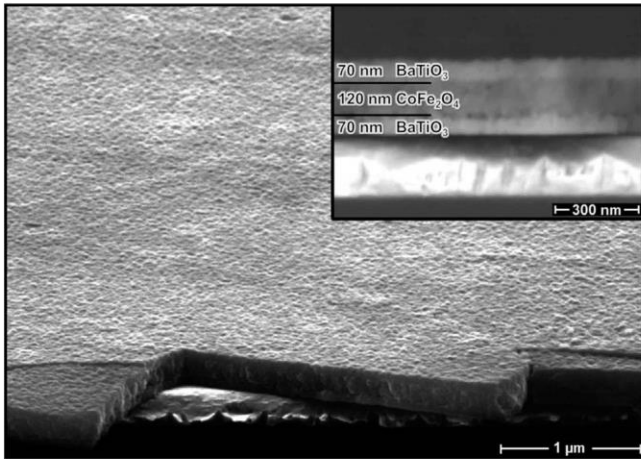


Fig. 7. SEM images of sample **1**: surface (SE mode) and cross section (inset; BSE mode).

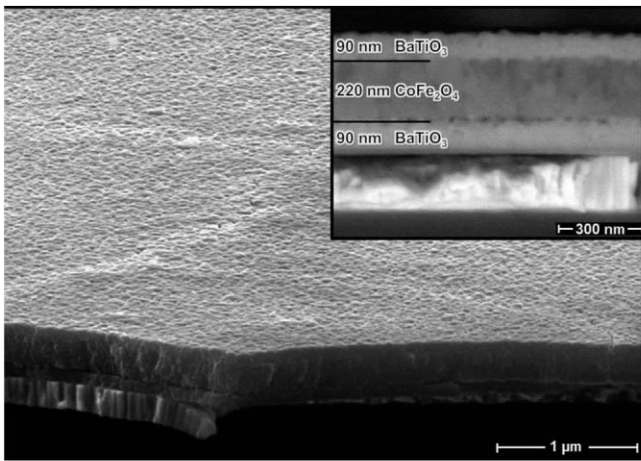


Fig. 8. SEM images of sample **2**: surface (SE mode) and cross section (inset; BSE mode).

**1** show a clearly distinguishable sandwich structure. The thickness of the bottom BaTiO<sub>3</sub> layer is about 70 nm, followed by the 120 nm thick CoFe<sub>2</sub>O<sub>4</sub> and the top layer BaTiO<sub>3</sub> of again 70 nm. Since three and five spin coating steps were applied for the BaTiO<sub>3</sub> and CoFe<sub>2</sub>O<sub>4</sub> layers, respectively, it can be stated that each coating step leads to an individual layer of  $25 \pm 5$  nm thickness independent of type of oxide deposited.

The sandwich structure of sample **2** is shown in Fig. 8. The CoFe<sub>2</sub>O<sub>4</sub> layer (eight spin coating steps) with a thickness of 220 nm is embedded between two 90 nm BaTiO<sub>3</sub> layers (four spin coating steps each). The secondary electron mode SEM images of sample **1** and **2** reveal the uniform and smooth surfaces of both samples.

Between the top BaTiO<sub>3</sub> and the CoFe<sub>2</sub>O<sub>4</sub> layers of both samples uniform interfaces with direct contact of the two phases formed, whereas the interfaces between the bottom BaTiO<sub>3</sub> and the CoFe<sub>2</sub>O<sub>4</sub> layers are partially disturbed by voids. Thus, BaTiO<sub>3</sub> is growing much better on CoFe<sub>2</sub>O<sub>4</sub> than vice versa.

To further investigate the quality of the sample surfaces, AFM images were taken (Fig. 9). The root mean square value (rms) of 3.8 for **1** is slightly smaller than the 4.6 nm for **2**, probably because of the larger number of coating steps and in turn increased sample thickness of sample **2**. Both surfaces show circular shaped particles, indicated as grains. The sizes of the BaTiO<sub>3</sub> particles were estimated to be in the range 50–120 nm for **1** and 60–160 nm for **2**. These diameters correspond roughly to the determined top layer thickness (from cross sectional SEM investigations) of 70 (**1**) and 90 nm (**2**) indicating an aspect ratio close to unity for the BTO particles. In general, the AFM investigations reveal good quality surfaces consistent with earlier literature reports on spin coated BaTiO<sub>3</sub> and respective composite thin films [30–32].

#### 3.4. Magnetic and electric properties

Field dependent magnetization curves of sample **1** and **2** are shown in Figs. 10 and 11. The in-plane and out-of-plane saturation magnetization values ( $M_S$ ) for sample **1** are both  $M_S = 307 \text{ emu cm}^{-3}$ . Whereas the  $M_S$  values for sample **2** slightly differ, with  $319 \text{ emu cm}^{-3}$  in-plane and  $338 \text{ emu cm}^{-3}$  out-of-plane. The difference between the saturation magnetizations of sample **1** and **2** is probably due to the thicker CoFe<sub>2</sub>O<sub>4</sub> layer, thus

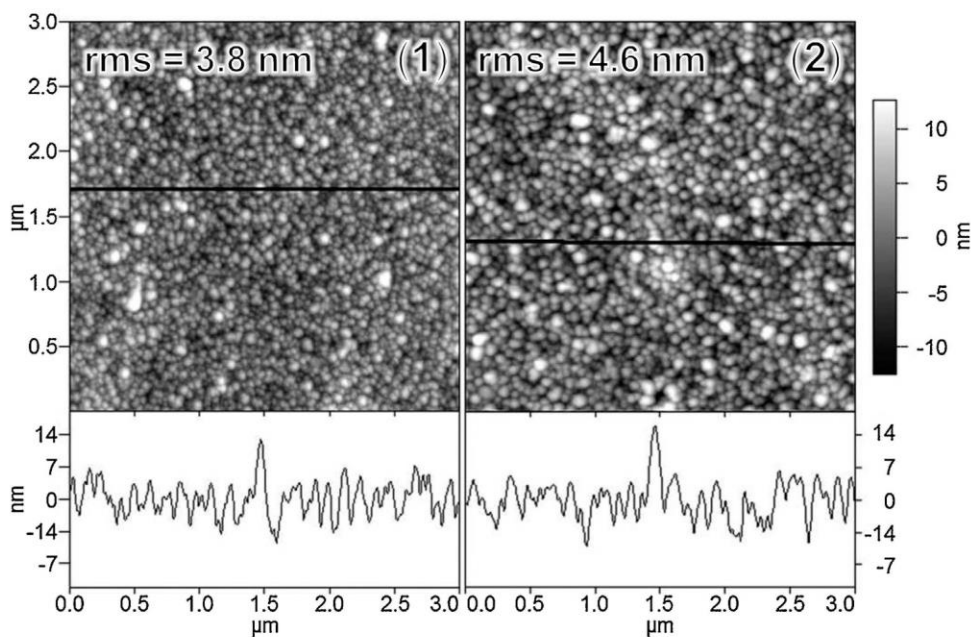


Fig. 9. AFM images and line traces (black lines) of samples **1** and **2**.

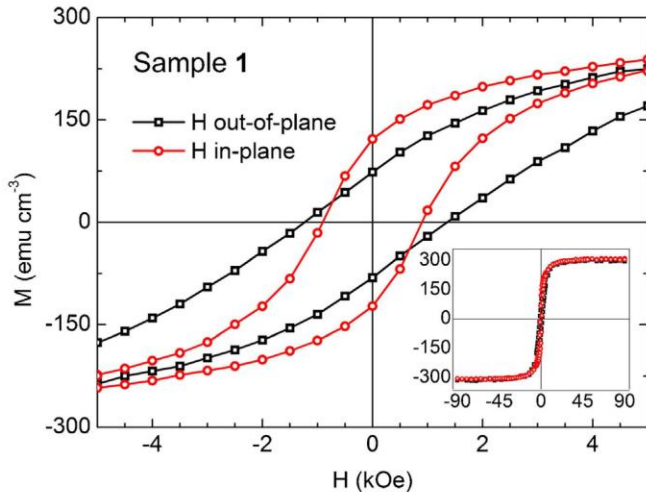


Fig. 10. Magnetic hysteresis of sample 1: 70 nm BaTiO<sub>3</sub> | 120 nm CoFe<sub>2</sub>O<sub>4</sub> | 70 nm BaTiO<sub>3</sub>.

increased grain sizes, for sample 2. Pronounced anisotropies were observed for the remanence magnetizations and coercivities. The remanence magnetization values ( $M_R$ ) of sample 1 are  $M_R = 122$  in-plane and  $75 \text{ emu cm}^{-3}$  out-of-plane, while for sample 2 the difference between  $M_R$  values is slightly higher with  $M_R = 132$  in-plane and  $M_R = 81 \text{ emu cm}^{-3}$  out-of-plane. The in-plane coercivities are  $H_C = 900$  for 1 and  $H_C = 800$  Oe for 2. In contrast, the coercivity values for out-of-plane aligned samples are about 400 Oe higher than for in-plane with  $H_C = 1300$  for 1 and  $H_C = 1200$  Oe for 2. Hence, the easy axis lies in the film plane for both samples. There are three possible sources for the magnetic anisotropy, namely shape-, magnetocrystalline- and strain-induced anisotropy [33]. A preferred orientation of the CoFe<sub>2</sub>O<sub>4</sub> grains in the films would lead to magnetocrystalline anisotropy, whereas strain induced anisotropy would indicate a strong coupling between CoFe<sub>2</sub>O<sub>4</sub> and BaTiO<sub>3</sub> interface, that is crucial for magneto-electric properties [5]. Therefore, the determination of the specifics of the anisotropy will be interesting to investigate in future work.

Field dependent polarization (P-E) and simultaneous current-voltage (I-V) measurements of samples 1 and 2 are shown in Figs. 12 and 13. Both P-E curves show a hysteresis with saturation polarizations (determined from the maximum of P) of 1:  $P_S = 29$  and 2:  $P_S = 24 \text{ } \mu\text{C cm}^{-2}$ , remanence polariza-

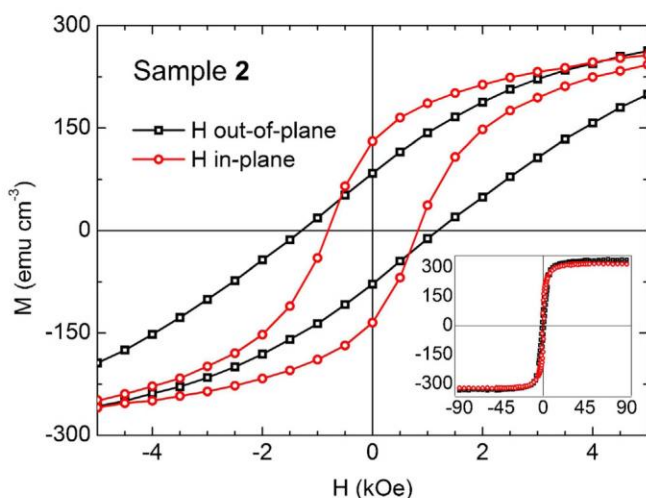


Fig. 11. Magnetic hysteresis of sample 2: 90 nm BaTiO<sub>3</sub> | 220 nm CoFe<sub>2</sub>O<sub>4</sub> | 90 nm BaTiO<sub>3</sub>.

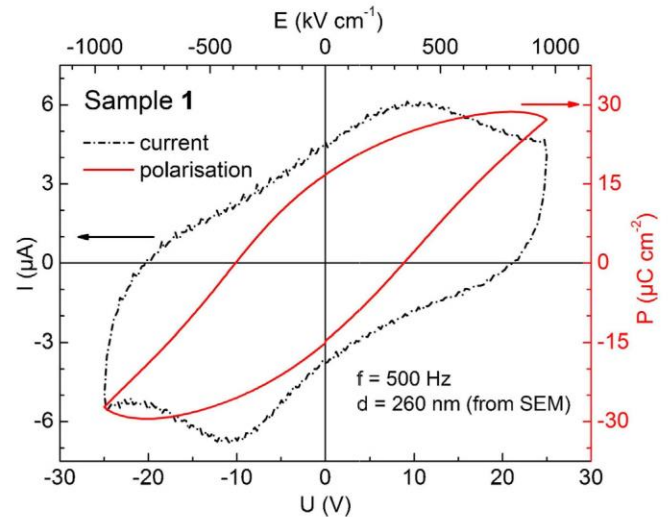


Fig. 12. Ferroelectric hysteresis and corresponding current loop of sample 1: 70 nm BaTiO<sub>3</sub> | 120 nm CoFe<sub>2</sub>O<sub>4</sub> | 70 nm BaTiO<sub>3</sub>.

tions  $P_R = 17$  and  $P_R = 11 \text{ } \mu\text{C cm}^{-2}$  and coercive electric fields with  $E_C = 360$  and  $E_C = 200 \text{ kV cm}^{-1}$ , respectively. Both samples show ferroelectric behavior [34]. The peaks in the I-V curves at the corresponding P-E coercive fields  $E_C$  are typical for the polarization switching in ferroelectric compounds [35]. To the best of our knowledge, the observed  $P_S$  and  $P_R$  values are among the highest reported for CoFe<sub>2</sub>O<sub>4</sub>-BaTiO<sub>3</sub> composites, with  $P_S$  varying from 3.4 to about  $30 \text{ } \mu\text{C cm}^{-2}$  [36–40] with a remarkable exception of  $P_S = 64(1) \text{ } \mu\text{C cm}^{-2}$  reported in [41]. Our measurements can also compete with various PLD films of pure BaTiO<sub>3</sub> (e.g.,  $P_S = 28 \text{ } \mu\text{C cm}^{-2}$  [35],  $P_R = 12.3 \text{ } \mu\text{C cm}^{-2}$  [42]). In addition, the saturation polarizations  $P_S = 27.3$  and  $23 \text{ } \mu\text{C cm}^{-2}$  found for single crystal [43] and ceramic bulk [44] BaTiO<sub>3</sub>, respectively, agree well with our results. On the other hand, it has to be noted that at high voltages (>20 V) our films become slightly leaky. This is probably due to the presence of oxygen vacancies, which might be healed by annealing in O<sub>2</sub>.

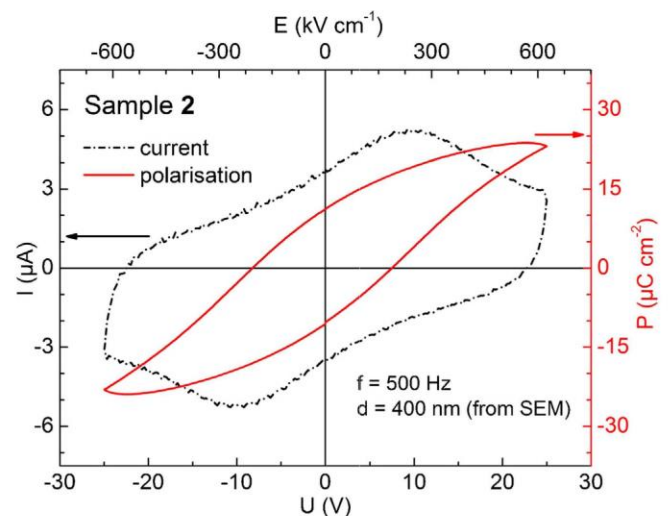


Fig. 13. Ferroelectric hysteresis and corresponding current loop of sample 2: 90 nm BaTiO<sub>3</sub> | 220 nm CoFe<sub>2</sub>O<sub>4</sub> | 90 nm BaTiO<sub>3</sub>.

#### 4. Conclusion

Two sandwich-structured BaTiO<sub>3</sub>-CoFe<sub>2</sub>O<sub>4</sub>-BaTiO<sub>3</sub> thin films with different thicknesses of the two oxide phases were prepared by a chemical solution based spin coating process. Thermal investigations of the precursor solutions revealed that a calcination temperature of 750 °C is high enough to ensure a complete phase formation of both the spinel and perovskite. In the infrared spectrum of sample **1** only longitudinal vibrations are detectable due to the Berreman effect, whereas the thicker sample **2** additionally shows one small transversal vibrational band. In Raman measurements only vibrational modes of CoFe<sub>2</sub>O<sub>4</sub> were detected for both samples because of the low absorption of BaTiO<sub>3</sub> at the used laser wavelength of 532 nm. The thickness of individual layers and the composite films in whole were derived from cross sectional SEM images. Each coating step leads to a growth of the layers by about 25 nm. Thus, the individual layer thickness of each sample is easily controllable by the number of the spin coating steps. While the interface of CFO on top of BTO showed some voids the reverse interface (BTO on CFO) was almost defect-free on the SEM scale. From atomic force microscopic measurements surface roughness values of rms = 3.8 and 4.6 nm were calculated for samples **1** and **2**, respectively. The saturation magnetization values of 307 emu cm<sup>-3</sup> (in and out-of-plane) for **1** with 120 nm CoFe<sub>2</sub>O<sub>4</sub> layer are slightly lower than the corresponding values of 319 (in-plane) and 338 emu cm<sup>-3</sup> (out-of-plane) for sample **2** with a thicker CoFe<sub>2</sub>O<sub>4</sub> layer of 220 nm. Both samples exhibit a magnetic anisotropy that hints to a preferred orientation of the CoFe<sub>2</sub>O<sub>4</sub> particles and a strong coupling between BaTiO<sub>3</sub> and CoFe<sub>2</sub>O<sub>4</sub> layers with the magnetic easy axis in the sample plane. Concerning the ferroelectric properties, the saturation and remanence polarization values  $P_S = 29$  and  $P_R = 17 \mu\text{C cm}^{-2}$  are higher for sample **1** (two 70 nm BaTiO<sub>3</sub> layers) than for sample **2** with  $P_S = 24$  and  $P_R = 11 \mu\text{C cm}^{-2}$  (two 90 nm BaTiO<sub>3</sub> layers). The polarization values of our spin coated films are comparable to the ones reported for PLD films and ceramic bulk BTO, indicating a very good film quality.

In summary, the spin coating of Ba/Ti- and Co/Fe-salts dissolved in HOAc/DMF was found to be a fast and versatile solution-based method to obtain high-quality multiferroic thin films exhibiting both ferrimagnetism and ferroelectricity. The thickness of the films can easily and reproducibly be controlled by the number of coating steps.

#### Acknowledgements

The authors thank Mr. F. Syrowatka for the SEM images and Prof. M. Alexe for providing access to the ferroelectric measurement equipment. Financial support by the German Research Foundation within the Collaborative Research Centre (SFB 762) Functionality of Oxide Interfaces is gratefully acknowledged.

#### References

- [1] N.A. Spaldin, M. Fiebig, The renaissance of magnetoelectric multiferroics, *Science* 309 (2005) 391–392, <http://dx.doi.org/10.1126/science.1113357>.
- [2] C.-W. Nan, M.I. Bichurin, S. Dong, D. Viehland, G. Srinivasan, Multiferroic magnetoelectric composites: historical perspective, status, and future directions, *J. Appl. Phys.* 103 (2008) 031101, <http://dx.doi.org/10.1063/1.2836410>.
- [3] J. Ma, J. Hu, Z. Li, C.-W. Nan, Recent progress in multiferroic magnetoelectric composites: from bulk to thin films, *Adv. Mater.* 23 (2011) 1062–1087, <http://dx.doi.org/10.1002/adma.201003636>.
- [4] R.E. Newnham, D.P. Skinner, L.E. Cross, Connectivity and piezoelectric-pyroelectric composites, *Mater. Res. Bull.* 13 (1978) 525–536, [http://dx.doi.org/10.1016/0025-5408\(78\)90161-7](http://dx.doi.org/10.1016/0025-5408(78)90161-7).
- [5] Y. Wang, J. Hu, Y. Lin, C.-W. Nan, Multiferroic magnetoelectric composite nanostructures, *NPG Asia Mater.* 2 (2010) 61–68, <http://dx.doi.org/10.1038/asiamat.2010.32>.
- [6] S. Priya, R. Islam, S. Dong, D. Viehland, Recent advancements in magnetoelectric particulate and laminate composites, *J. Electroceram.* 19 (2007), <http://dx.doi.org/10.1007/s10832-007-9042-5>.
- [7] J. Zhai, Z. Xing, S. Dong, J. Li, D. Viehland, Magnetoelectric laminate composites: an overview, *J. Am. Ceram. Soc.* 91 (2008) 351–358, <http://dx.doi.org/10.1111/j.1551-2916.2008.02259.x>.
- [8] R.C. Kambale, D.-Y. Jeong, J. Ryu, Current status of magnetoelectric composite thin/thick films, *Adv. Condens. Matter. Phys.* 2012 (2012) 1–15, <http://dx.doi.org/10.1155/2012/824643>.
- [9] M. Shi, R. Zuo, Y. Xu, L. Wang, C. Gu, H. Su, et al., Preparation and multiferroic properties of 2–2 type CoFe<sub>2</sub>O<sub>4</sub>/Pb(Zr,Ti)O<sub>3</sub> composite films with different structures, *Ceram. Int.* 40 (2014) 9249–9256, <http://dx.doi.org/10.1016/j.ceramint.2014.01.146>.
- [10] J.M. Li, G.Z. Li, Z.H. Bai, L.L. Wang, M. Feng, H.B. Li, Effects of Mg doping on multiferroic properties of bilayered Co<sub>1-x</sub>Mg<sub>x</sub>Fe<sub>2</sub>O<sub>4</sub>/PMN-PT composite thin films, *Ceram. Int.* 40 (2014) 1933–1937, <http://dx.doi.org/10.1016/j.ceramint.2013.07.101>.
- [11] B. Chen, Y.-C. Li, J.-Y. Wang, J.-G. Wan, J.-M. Liu, Anisotropic manipulation of ferroelectric polarization in SrTiO<sub>3</sub>/(Co<sub>0.9</sub>Zn<sub>0.1</sub>)Fe<sub>2</sub>O<sub>4</sub> heterostructural films by magnetic field, *J. Appl. Phys.* 115 (2014) 044102, <http://dx.doi.org/10.1063/1.4863144>.
- [12] Y. Kawabata, W. Sakamoto, K. Yoshida, T. Iijima, M. Moriya, T. Yogo, Synthesis and characterization of multiferroic Pb(Zr,Ti)O<sub>3</sub>/CoFe<sub>2</sub>O<sub>4</sub>/Pb(Zr,Ti)O<sub>3</sub> layered composite thin films by chemical solution deposition, *J. Ceram. Soc. Jpn.* 121 (2013) 614–618.
- [13] B. Bajac, J. Vukmirovic, I. Tokic, S. Ognjanovic, V.V. Srdic, Synthesis and characterization of multilayered BaTiO<sub>3</sub>/NiFe<sub>2</sub>O<sub>4</sub> thin films, *Process. Appl. Ceram.* 7 (2013) 15–20, <http://dx.doi.org/10.2298/PAC1301015B>.
- [14] M. Feng, W. Wang, Y. Zhou, H. Li, D. Jia, Influence of residual stress on magnetoelectric coupling of bilayered CoFe<sub>2</sub>O<sub>4</sub>/PMN-PT thin films, *J. Mater. Chem.* 21 (2011) 10738–10743, <http://dx.doi.org/10.1039/C1JM11271F>.
- [15] J.G. Wan, X.W. Wang, Y.J. Wu, M. Zeng, Y. Wang, H. Jiang, et al., Magnetoelectric CoFe<sub>2</sub>O<sub>4</sub>-Pb(Zr,Ti)O<sub>3</sub> composite thin films derived by a sol-gel process, *Appl. Phys. Lett.* 86 (2005) 122501, <http://dx.doi.org/10.1063/1.1889237>.
- [16] Y.Q. Dai, J.M. Dai, X.W. Tang, K.J. Zhang, X.B. Zhu, J. Yang, et al., Thickness effect on the properties of BaTiO<sub>3</sub>-CoFe<sub>2</sub>O<sub>4</sub> multilayer thin films prepared by chemical solution deposition, *J. Alloys Compounds* 587 (2014) 681–687, <http://dx.doi.org/10.1016/j.jallcom.2013.11.026>.
- [17] PDF 2 (International Centre for Diffraction Data, Pennsylvania). CoFe<sub>2</sub>O<sub>4</sub> [22–1086], BaTiO<sub>3</sub> [79–2263] (2001).
- [18] M.H. Frey, D.A. Payne, Grain-size effect on structure and phase transformations for barium titanate, *Phys. Rev. B* 54 (1996) 3158–3168, <http://dx.doi.org/10.1103/PhysRevB.54.3158>.
- [19] D.W. Berreman, Infrared absorption at longitudinal optic frequency in cubic crystal films, *Phys. Rev.* 130 (1963) 2193–2198, <http://dx.doi.org/10.1103/PhysRev.130.2193>.
- [20] E.J.H. Lee, F.M. Pontes, E.R. Leite, E. Longo, R. Magnani, P.S. Pizani, et al., Effects of post-annealing on the dielectric properties of Au/BaTiO<sub>3</sub>/Pt thin film capacitors, *Mater. Lett.* 58 (2004) 1715–1721, <http://dx.doi.org/10.1016/j.matlet.2003.10.047>.
- [21] M. Lenglet, B. Lefez, Infrared optical properties of cobalt(II) spinels, *Solid State Commun.* 98 (1996) 689–694, [http://dx.doi.org/10.1016/0038-1098\(96\)00109-3](http://dx.doi.org/10.1016/0038-1098(96)00109-3).
- [22] R.D. Waldron, Infrared spectra of ferrites, *Phys. Rev.* 99 (1955) 1727–1735, <http://dx.doi.org/10.1103/PhysRev.99.1727>.
- [23] T. Müller, T. Großmann, H.-P. Abicht, Nitrogen containing barium titanate: preparation and characterisation, *J. Phys. Chem. Solids* 70 (2009) 1093–1097, <http://dx.doi.org/10.1016/j.jpcs.2009.06.003>.
- [24] F. Hochu, M. Lenglet, Co(II) optical absorption in spinels: infrared and ligand-field spectroscopic study of the ionicity of the bond. Magnetic structure and Co<sup>2+</sup> → Fe<sup>3+</sup> MMCT in ferrites. Correlation with the magneto-optical properties, *Acta Passiva Electron. Components* 20 (1998) 169–187, <http://dx.doi.org/10.1155/1998/16871>.
- [25] P.R. Graves, C. Johnston, J.J. Campaniello, Raman scattering in spinel structure ferrites, *Mater. Res. Bull.* 23 (1988) 1651–1660, [http://dx.doi.org/10.1016/0025-5408\(88\)90255-3](http://dx.doi.org/10.1016/0025-5408(88)90255-3).
- [26] J. Barbosa, B. Almeida, J.A. Mendes, A.G. Rolo, J.P. Araújo, X-ray diffraction and Raman study of nanogranular BaTiO<sub>3</sub>-CoFe<sub>2</sub>O<sub>4</sub> thin films deposited by laser ablation on Si/Pt substrates, *Phys. Status Solidi A* 204 (2007) 1731–1737, <http://dx.doi.org/10.1002/pssa.200675327>.
- [27] H. Cynn, S.K. Sharma, T.F. Cooney, M. Nicol, High-temperature Raman investigation of order-disorder behavior in the MgAl<sub>2</sub>O<sub>4</sub> spinel, *Phys. Rev. B* 45 (1992) 500–502, <http://dx.doi.org/10.1103/PhysRevB.45.500>.
- [28] Z. Wang, P. Lazor, S.K. Saxena, H.S.C. O'Neill, High pressure Raman spectroscopy of ferrite MgFe<sub>2</sub>O<sub>4</sub>, *Mater. Res. Bull.* 37 (2002) 1589–1602, [http://dx.doi.org/10.1016/S0025-5408\(02\)819-X](http://dx.doi.org/10.1016/S0025-5408(02)819-X).
- [29] P. Chandramohan, M.P. Srinivasan, S. Velmurugan, S.V. Narasimhan, Cation distribution and particle size effect on Raman spectrum of CoFe<sub>2</sub>O<sub>4</sub>, *J. Solid State Chem.* 184 (2011) 89–96, <http://dx.doi.org/10.1016/j.jssc.2010.10.019>.
- [30] F.M. Pontes, E.R. Leite, E.J.H. Lee, E. Longo, J.A. Varela, Dielectric properties and microstructure of SrTiO<sub>3</sub>/BaTiO<sub>3</sub> multilayer thin films prepared by a chemical route, *Thin Solid Films* 385 (2001) 260–265, [http://dx.doi.org/10.1016/S0040-6090\(01\)772-6](http://dx.doi.org/10.1016/S0040-6090(01)772-6).
- [31] K. Tanaka, K. Suzuki, D. Fu, K. Nishizawa, T. Miki, K. Kato, Grain size effect on dielectric and piezoelectric properties of alkoxy-derived BaTiO<sub>3</sub>-based thin

- films, *Jpn. J. Appl. Phys.* 43 (2004) 6525–6529, <http://dx.doi.org/10.1143/JJAP.43.6525>.
- [32] Y. Ito, W. Sakamoto, M. Moriya, T. Yogo, Synthesis and properties of multiferroic  $0.7\text{BiFeO}_3$ – $0.3\text{BaTiO}_3$  thin films by Mn doping, *Ceram. Int. (Suppl. 1)* (2013) 39, <http://dx.doi.org/10.1016/j.ceramint.2012.10.112>, S451–S455.
- [33] J. Barbosa, B. Almeida, A.M. Pereira, J.P. Araújo, I. Gomes, J. Mendes, Stress induced magnetic anisotropy on  $\text{BaTiO}_3$ – $\text{CoFe}_2\text{O}_4$  nanogranular composite thin films, *J. Non-Cryst. Solids* 354 (2008) 5250–5252, <http://dx.doi.org/10.1016/j.jnoncrsol.2008.05.085>.
- [34] J.F. Scott, Ferroelectrics go bananas, *J. Phys. Condens. Matter.* 20 (2008) 021001, <http://dx.doi.org/10.1088/0953-8984/20/02/021001>.
- [35] O. Trithaveesak, J. Schubert, C. Buchal, Ferroelectric properties of epitaxial  $\text{BaTiO}_3$  thin films and heterostructures on different substrates, *J. Appl. Phys.* 98 (2005) 114101, <http://dx.doi.org/10.1063/1.2135891>.
- [36] X.-H. Liu, Z. Xu, X.-Y. Wei, Z.-H. Dai, X. Yao, Ferroelectric, ferromagnetic, and magnetoelectric characteristics of  $0.9(0.7\text{BiFeO}_3$ – $0.3\text{BaTiO}_3)$ – $0.1\text{CoFe}_2\text{O}_4$  ceramic composite, *J. Am. Ceram. Soc.* 93 (2010) 2975–2977.
- [37] Y. Deng, D. Wu, H. Yu, Y. Du, Enhanced magnetoelectric response and phonon abnormality of self-assembled feather-like  $\text{CoFe}_2\text{O}_4$ – $\text{BaTiO}_3$  nanostructures, *Symp. HH—Nanocompos. Nanostruct. Heterostruct. Correl. Oxide Syst.* 1454 (2012) 57–62, <http://dx.doi.org/10.1557/opl.2012.1068>.
- [38] G. Jian, D. Zhou, J. Yang, H. Shao, F. Xue, Q. Fu, Microstructure and multiferroic properties of  $\text{BaTiO}_3/\text{CoFe}_2\text{O}_4$  films on  $\text{Al}_2\text{O}_3/\text{Pt}$  substrates fabricated by electrophoretic deposition, *J. Eur. Ceram. Soc.* 33 (2013) 1155–1163, <http://dx.doi.org/10.1016/j.jeurceramsoc.2012.11.012>.
- [39] N. Dix, I. Fina, R. Bachelet, L. Fàbrega, C. Kanamadi, J. Fontcuberta, et al., Large out-of-plane ferroelectric polarization in flat epitaxial  $\text{BaTiO}_3$  on  $\text{CoFe}_2\text{O}_4$  heterostructures, *Appl. Phys. Lett.* 102 (2013) 172907, <http://dx.doi.org/10.1063/1.4803943>.
- [40] Q. Yang, W. Zhang, M. Yuan, L. Kang, J. Feng, W. Pan, et al., Preparation and characterization of self-assembled percolative  $\text{BaTiO}_3$ – $\text{CoFe}_2\text{O}_4$  nanocomposites via magnetron co-sputtering, *Sci. Technol. Adv. Mater.* 15 (2014) 025003, <http://dx.doi.org/10.1088/1468-6996/15/2/025003>.
- [41] I. Fina, N. Dix, J.M. Rebled, P. Gemeiner, X. Martí, F. Peiró, et al., The direct magnetoelectric effect in ferroelectric–ferromagnetic epitaxial heterostructures, *Nanoscale* 5 (2013) 8037–8044, <http://dx.doi.org/10.1039/C3NR01011B>.
- [42] T. Li, Z. Hu, M. Zhang, K. Li, D. Yu, H. Yan, Frequency dependence of magnetoelectric effect in epitaxial  $\text{La}_{0.7}\text{Sr}_{0.3}\text{MnO}_3/\text{BaTiO}_3$  bilayer film, *Appl. Surf. Sci.* 258 (2012) 4558–4562, <http://dx.doi.org/10.1016/j.apsusc.2012.01.027>.
- [43] R. Imura, Y. Kitanaka, T. Oguchi, Y. Noguchi, M. Miyayama, Polarization properties and crystal structures of ferroelectric ( $\text{Ba,Ca}$ ) $\text{TiO}_3$  single crystals, *J. Adv. Dielectr.* 4 (2014) 1450003, <http://dx.doi.org/10.1142/S2010135X14500039>.
- [44] Y. Huan, X. Wang, J. Fang, L. Li, Grain size effect on piezoelectric and ferroelectric properties of  $\text{BaTiO}_3$  ceramics, *J. Eur. Ceram. Soc.* 34 (2014) 1445–1448, <http://dx.doi.org/10.1016/j.jeurceramsoc.2013.11.030>.

**A2** Hysteretic magnetoelectric behavior of  $\text{CoFe}_2\text{O}_4\text{-BaTiO}_3$  composites prepared by reductive sintering and reoxidation

Reprinted with the permission of the Royal Society of Chemistry.



Cite this: *J. Mater. Chem. C*, 2016,  
4, 4792

## Hysteretic magnetoelectric behavior of CoFe<sub>2</sub>O<sub>4</sub>–BaTiO<sub>3</sub> composites prepared by reductive sintering and reoxidation

Till Walther,<sup>a</sup> Ulrich Straube,<sup>b</sup> Roberto Köferstein<sup>a</sup> and Stefan G. Ebbinghaus<sup>\*a</sup>

Magnetoelectric composites (CoFe<sub>2</sub>O<sub>4</sub>)<sub>x</sub>–(BaTiO<sub>3</sub>)<sub>1–x</sub> with  $x = 0.1, 0.2, 0.3, 0.4$  and  $0.5$  were prepared by a polyol mediated synthesis route. The densification step was performed in a reducing forming gas atmosphere at 1250 °C. Under these conditions Co<sup>2+</sup> and Fe<sup>3+</sup> are reduced to the corresponding metals and thus a reaction of these elements with the BaTiO<sub>3</sub> matrix is prevented. Reoxidation in air to CoFe<sub>2</sub>O<sub>4</sub> at a rather low temperature of 800 °C leads to samples free of secondary phases. While the course of the synthesis was monitored by TGA, XRD and photometric analysis, the final composites were characterized via SEM, EDX, impedance spectroscopy and magnetic and magnetoelectric (ME) measurements. All samples show pronounced ME hystereses and  $\alpha_{ME}$  maxima dependent on the  $H_{dc}$  field sweep direction. The sample with  $x = 0.4$  exhibits the highest maximum  $\alpha_{ME}$  of 420  $\mu\text{V Oe}^{-1} \text{cm}^{-1}$ .

Received 8th March 2016,  
Accepted 14th April 2016

DOI: 10.1039/c6tc00995f

www.rsc.org/MaterialsC

### 1. Introduction

Multiferroic composites consist of a combination of compounds, which exhibit at least one ferroic order phenomenon like ferroelectricity and ferro- or ferrimagnetism. The coupling between magnetostrictive and piezoelectric phases allows manipulating the electric polarization by a magnetic field or the magnetization by an electric field. These so-called direct and indirect magnetoelectric (ME) effects promise new applications and devices, such as spintronics and MERAMS.<sup>1–4</sup> Several composites have been identified as magnetoelectric materials.<sup>5</sup> The first discovered magnetoelectric composite – and still one of the most prominent combinations – is the system consisting of CoFe<sub>2</sub>O<sub>4</sub> (CFO) and BaTiO<sub>3</sub> (BTO).<sup>6</sup> The hard ferrimagnetic CoFe<sub>2</sub>O<sub>4</sub> shows large magnetostriction while BaTiO<sub>3</sub> is ferroelectric with high piezoelectricity. Furthermore, this system is free of resource-critical elements and is predicted to exhibit high ME voltages.<sup>7–10</sup> CoFe<sub>2</sub>O<sub>4</sub> and BaTiO<sub>3</sub> have already been combined in all three prominent connectivities for composite multiferroics, namely 0–3, 1–3 and 2–2.<sup>11,12</sup> The reported  $\alpha_{ME}$  values for 0–3 composites are typically ranging from a few  $\mu\text{V Oe}^{-1} \text{cm}^{-1}$  to 10  $\text{mV Oe}^{-1} \text{cm}^{-1}$ .<sup>13–15</sup> However, the theoretically predicted much higher  $\alpha_{ME}$  values have not yet been achieved.<sup>16</sup> This is most often explained by an

insufficient interface between the piezoelectric and magnetostrictive phase that prevents mechanical transfers and thus good coupling. One approach to tailor the interface is to build up composites from nanoparticles because of their large surface to volume ratio. One disadvantage of this strategy is that impurities which originate from the reaction of BaTiO<sub>3</sub> with CoFe<sub>2</sub>O<sub>4</sub> at the interface, like substituted barium hexaferrite Ba(Co<sub>0.5</sub>Ti<sub>0.5</sub>)<sub>x</sub>Fe<sub>12–x</sub>O<sub>19</sub>, are favored by large interface areas. While pure BaFe<sub>12</sub>O<sub>19</sub> is multiferroic on its own<sup>17,18</sup> and even composites with perovskites have been investigated,<sup>19,20</sup> the incorporation of Co<sup>2+</sup> and Ti<sup>4+</sup> in BaFe<sub>12</sub>O<sub>19</sub> has a significant impact on its magnetic properties.<sup>21,22</sup>

To overcome the formation of impurity phases, we present in this article a polyol mediated synthesis route for magnetoelectric CoFe<sub>2</sub>O<sub>4</sub>–BaTiO<sub>3</sub> composite ceramics. Using a reductive sintering step followed by reoxidation under mild conditions, the formation of Ba(Co<sub>0.5</sub>Ti<sub>0.5</sub>)<sub>x</sub>Fe<sub>12–x</sub>O<sub>19</sub> was successfully suppressed and phase pure samples with relative densities > 80% were obtained. Measurements of the magnetoelectric coupling show frequency independent values of the ME coefficient above 300 Hz. All samples exhibit a pronounced ME hysteresis with a maximum of  $\alpha_{ME}$  at  $H_{dc} \approx \pm 2500$  Oe. Furthermore, we for the first time describe a dependence of the maximum  $\alpha_{ME}$  values on the direction of the DC-field sweep.

### 2. Experimental

#### 2.1 Material preparation

All chemicals were used as purchased without further purification, if not stated otherwise. Five samples of (CoFe<sub>2</sub>O<sub>4</sub>)<sub>x</sub>–(BaTiO<sub>3</sub>)<sub>(1–x)</sub>

<sup>a</sup> Institute of Chemistry, Inorganic Chemistry, Martin Luther University Halle-Wittenberg, Kurt Mothes Strasse 2, 06120 Halle, Germany.  
E-mail: stefan.ebbinghaus@chemie.uni-halle.de; Fax: +49-345-5527028;  
Tel: +49-345-5525870

<sup>b</sup> Institute of Physics, Martin Luther University Halle-Wittenberg, von Danckelmann Platz 3, 06120 Halle, Germany



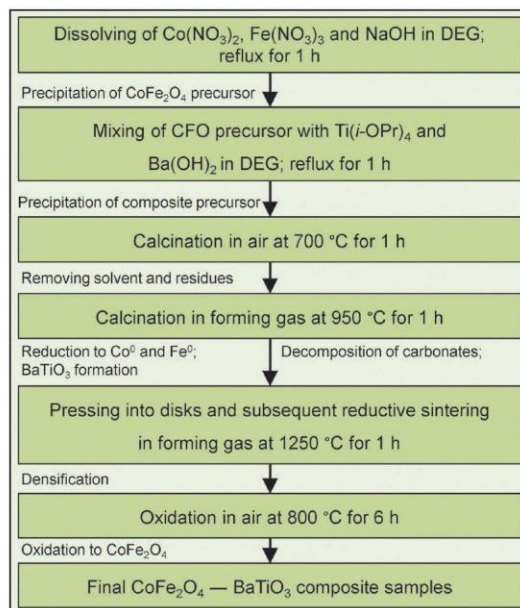


Fig. 1 Scheme of sample preparation.

composites were synthesized with  $x_{\text{CFO}} = 0.1, 0.2, 0.3, 0.4$  and  $0.5$ . A modified polyol mediated process was used to prepare the precursor powders for the ceramics.<sup>23,24</sup> The preparation scheme is shown in Fig. 1 and is described as follows.

$\text{Fe}(\text{NO}_3)_3 \cdot 9\text{H}_2\text{O}$  (20 mmol, Sigma Aldrich) and  $\text{Co}(\text{NO}_3)_2 \cdot 6\text{H}_2\text{O}$  (10 mmol, Sigma Aldrich) were dissolved in deionized water (6 ml). NaOH (80 mmol, Grüssing) and diethylene glycol (250 ml, Carl Roth) were added to the red solution, which was then heated within 45 min to its boiling point ( $\sim 160$  °C) and refluxed for 1 h. After cooling to room temperature, acetone (250 ml, Overlack) was added, resulting in a brown precipitate. Subsequent centrifugation and washing with acetone led to a brown  $\text{CoFe}_2\text{O}_4$  precursor powder. The amount of ferrite was determined by thermogravimetric analysis.

For sample 0.5CFO–0.5BTO, 5 mmol of the presynthesized  $\text{CoFe}_2\text{O}_4$  precursor and 5 mmol  $\text{Ba}(\text{OH})_2 \cdot 8\text{H}_2\text{O}$  (FLUKA) were mixed with diethylene glycol (250 ml, Carl Roth) in an argon flushed flask. Distilled  $\text{Ti}(\text{i-OPr})_4$  (5 mmol, Alfa Aesar) was added and the reaction mixture was heated within 45 min to the boiling point ( $\sim 160$  °C) and kept under reflux for 1 h. After cooling to room temperature, 250 ml of acetone (Overlack) were added to the gray suspension and subsequent centrifugation and washing with acetone led to a gray composite precursor. The precursor powders for the other samples were prepared accordingly, using the respective stoichiometric quantities.

The precursor powders were first calcined in static air at 700 °C for 1 h with a heating rate of 10 K  $\text{min}^{-1}$ . Afterwards, a first reduction step in flowing forming gas (80 ml  $\text{min}^{-1}$ , 10%  $\text{H}_2$ ) at 950 °C for 1 h (heating rate 5 K  $\text{min}^{-1}$ ) was performed and the resulting light gray powders were pressed into disks (100 mg,  $\varnothing = 6$  mm) that were sintered in flowing forming gas (80 ml  $\text{min}^{-1}$ , 10%  $\text{H}_2$ ) at 1250 °C for 1 h (heating rate 5 K  $\text{min}^{-1}$ ). Finally, reoxidation in static air at 800 °C for 6 h (heating rate 10 K  $\text{min}^{-1}$ ) led to black ceramic bodies of  $\text{CoFe}_2\text{O}_4$ - $\text{BaTiO}_3$  composites.

## 2.2 Characterization

Thermogravimetric measurements in flowing synthetic air or forming gas (10%  $\text{H}_2$ ) (flow rate 40 ml  $\text{min}^{-1}$ , heat rate 10 K  $\text{min}^{-1}$ ) were performed using a Netzsch STA 409 system. X-ray diffraction patterns were recorded at room temperature on a Bruker D8 Advance diffractometer operating with  $\text{CuK}\alpha$  radiation. For the quantitative cobalt ferrite determination, small aliquots of the samples were dissolved in a mixture of hydrochloric acid ( $\geq 37\%$ , Sigma Aldrich) and hydrogen peroxide solution (30%, Overlack). After dissolution, residual peroxides were decomposed by heating. The solutions were diluted to an approximated Fe concentration of 1 mg  $\text{l}^{-1}$  and Spectroquant Iron Test solution (Merck Millipore) was added. For absorbance measurements at  $\lambda = 560$  nm a VWR UV-3100PC Spectrophotometer was used. The Fe concentrations and corresponding  $\text{CoFe}_2\text{O}_4$  contents were determined by a calibration series. Scanning electron microscopy images in the backscattered electron (BSE) mode and EDX spectra were recorded using a Philips ESEM XL 30 FEG. For impedance measurements an eutectic Ga–In alloy was coated as electrodes on top and bottom surfaces of the ceramic bodies. The temperature and frequency dependent impedance spectra (0 to 180 °C; 100 Hz to 13 MHz) were recorded using a Hewlett-Packard 4192A impedance analyzer. Magnetic measurements were carried out using the ACMS option of a Quantum Design PPMS 9. Hysteresis loops were measured at 300 K with a cycling of the magnetic field between +90 and –90 kOe. For the magnetoelectric investigations, 100 nm thick gold electrodes were sputtered onto the sample surfaces using a Cressington Sputter Coater 108auto. Electric poling was done applying an electric DC field of 4 kV  $\text{cm}^{-1}$  to the samples at room temperature. Then the samples were heated to 200 °C for 1 h (heating rate 10 K  $\text{min}^{-1}$ ) and the electric field was dynamically adjusted setting the current limit to 0.1 mA. Due to the increasing conductivity of the samples the field decreased to a few V  $\text{cm}^{-1}$  at 200 °C but again reached 4 kV  $\text{cm}^{-1}$  during cooling to room temperature. After poling, the samples were short circuited for 10 min. Immediately afterwards, the ME measurements were performed at 300 K in a Quantum Design PPMS 9 using a custom made setup based on the AC-Transport measurement option. A magnetic AC field of  $H_{\text{ac}} = 10$  Oe with different frequencies was applied by a solenoid with 1160 loops of copper wire and the ME voltage was measured in dependence of the magnetic DC field upon cycling between +10 and –10 kOe. Magnetic AC and DC fields were aligned parallel to the electric polarization. Raw data were corrected for eddy currents measured on an empty sample holder. The magnetoelectric coefficient was calculated as  $\alpha_{\text{ME}} = U/(H_{\text{ac}} \cdot h)$  with  $h$  being the sample height.

## 3. Results and discussion

### 3.1 Thermal analysis

Simultaneous thermogravimetric and differential thermal analyses were carried out on the samples to investigate calcination, sintering and reoxidation behavior. The results are discussed for 0.3CFO–0.7BTO exemplarily as follows.



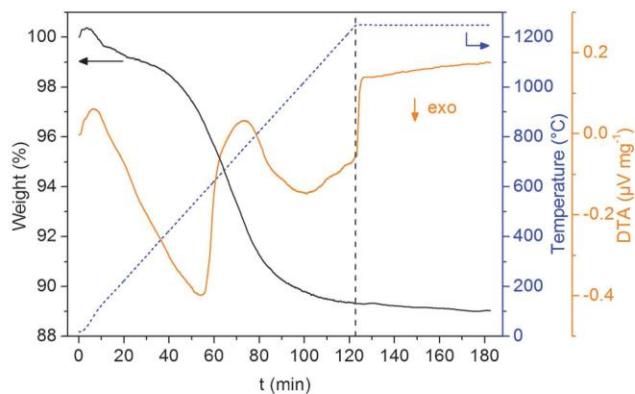


Fig. 2 TGA/DTA investigation of 0.3CFO–0.7BTO air-calcined powder under reductive sintering conditions in flowing forming gas.

Calcination of the dried composite precursor in air at 700 °C leads to a total weight loss of 45%. This weight change comprises the evaporation of residual solvent and adsorbed water, an exothermal combustion of organic residues and the endothermal decomposition of intermediately formed  $\text{BaO}_x(\text{CO}_3)_{1-x}$ .<sup>25–27</sup>

Following the path of preparation and representing the calcination and sintering steps under reducing conditions, an air-calcined sample was heated in the thermobalance in flowing forming gas to 1250 °C and kept at this temperature for 1 h. The corresponding weight change and DTA curves are shown in Fig. 2. The main weight loss of 9.0% occurs between 350 and 1000 °C and is accompanied by two distinct exothermal signals in the DTA curve. During this step, the reduction of  $\text{CoFe}_2\text{O}_4$  to an alloy of Co and Fe (expected weight loss: 7.7%), the decomposition of residual  $\text{BaCO}_3$  and the final formation of  $\text{BaTiO}_3$  take place. During the dwell time of 1 h at 1250 °C a further slight weight loss of about 2% was observed. This weight loss could be caused by a gradual generation of oxygen defects and the accompanied partial reduction of  $\text{Ti}^{4+}$  in the  $\text{BaTiO}_3$  matrix. Overall a weight loss of 11.0% occurred.

Afterwards, the resulting  $\text{CoFe}_2\text{-BaTiO}_3$  sample was heated in synthetic air up to 800 °C and kept at that temperature for 6 h to investigate the reoxidation behavior. As shown in Fig. 3, a weight gain accompanied by an exothermic DTA signal starts at

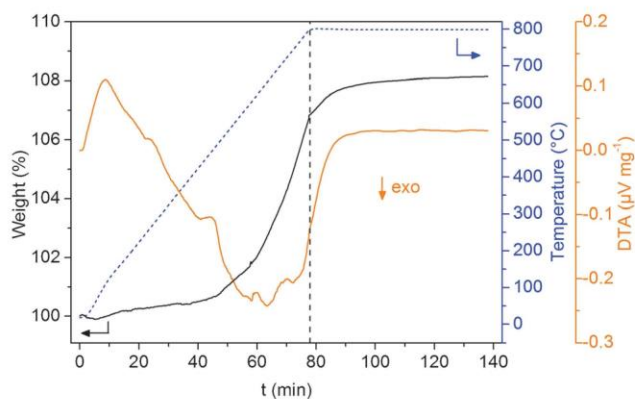


Fig. 3 TGA/DTA investigation in flowing air of 0.3CoFe<sub>2</sub>–0.7BTO under reoxidation conditions.

430 °C and is finished about 1 h after reaching 800 °C. This process leads to a total weight change of +8.2%. Longer heating at 800 °C did not lead to any significant additional weight change. For the complete oxidation of the  $\text{CoFe}_2$  alloy in the 0.3CFO–0.7BTO sample, a theoretical weight gain of 8.4% is expected. Thus, the observed change of +8.2% can be assigned completely to the reoxidation of the alloy to  $\text{CoFe}_2\text{O}_4$  as additionally supported by the XRD results discussed in the next paragraph.

### 3.2 X-ray diffraction

The course of the synthesis was monitored by X-ray powder diffraction as exemplarily shown for  $x_{\text{CFO}} = 0.5$  in Fig. 4. The diffractogram of the precursor obtained by precipitation without further temperature treatment (Fig. 4a) mainly shows crystalline  $\text{BaCO}_3$  and  $\text{CoFe}_2\text{O}_4$  implying that at least one Ti-containing amorphous phase is present. Calcination in air at 700 °C for 1 h leads to the formation of  $\text{BaTiO}_3$  although some  $\text{BaCO}_3$  is still detectable in the powder (Fig. 4b). Calcination or sintering in air at temperatures higher than 700 °C leads to reactions between the  $\text{BaTiO}_3$  matrix and the ferrite, *i.e.* the formation of impurities such as  $\text{Ti}^{4+}$ - and  $\text{Co}^{2+}$ -doped  $\text{BaFe}_{12}\text{O}_{19}$ , hexagonal  $\text{BaTiO}_3$  as well as increased  $\text{Co}^{2+}$  and  $\text{Fe}^{3+}$  doping of  $\text{BaTiO}_3$ . To avoid this, an additional calcination step in forming gas (10%  $\text{H}_2$ ) at 950 °C for 1 h was performed. Under these conditions residual  $\text{BaCO}_3$  decomposes and the X-ray diffraction pattern (Fig. 4c) indicates the formation of (pseudo-) cubic modification for  $\text{BaTiO}_3$ . In addition,  $\text{CoFe}_2\text{O}_4$  is reduced to an alloy of Co and Fe that does not react with  $\text{BaTiO}_3$  as the ferrite would. The resulting reduced powder was pressed into disks ( $\varnothing = 6$  mm,  $m = 100$  mg) and sintered at 1250 °C for 1 h in forming gas. The corresponding X-ray diffraction pattern shows a mixture of tetragonal  $\text{BaTiO}_3$  and the  $\text{CoFe}_2$  alloy (Fig. 4d). Afterwards, the ceramic body was reoxidized in air at 800 °C for 6 h resulting in an oxidation of the  $\text{CoFe}_2$  alloy to  $\text{CoFe}_2\text{O}_4$  (Fig. 4e).

As shown in Fig. 5, phase pure  $\text{CoFe}_2\text{O}_4\text{-BaTiO}_3$  composites were obtained for all investigated compositions with  $x_{\text{CFO}} = 0.1, 0.2, 0.3, 0.4, \text{ and } 0.5$ . By Rietveld refinement the cell parameters

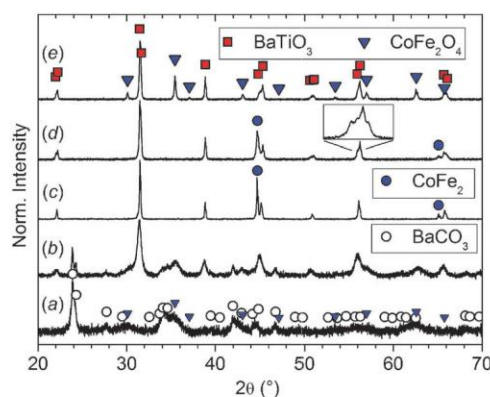


Fig. 4 X-ray diffraction patterns of 0.5CFO–0.5BTO: (a) precursor; (b) calcined in air at 700 °C for 1 h; (c) calcined in forming gas at 950 °C for 1 h; (d) sintered in forming gas at 1250 °C for 1 h, zoom: tetragonal splitting of  $\text{BaTiO}_3$  211 reflex; (e) reoxidized in air at 800 °C for 6 h.



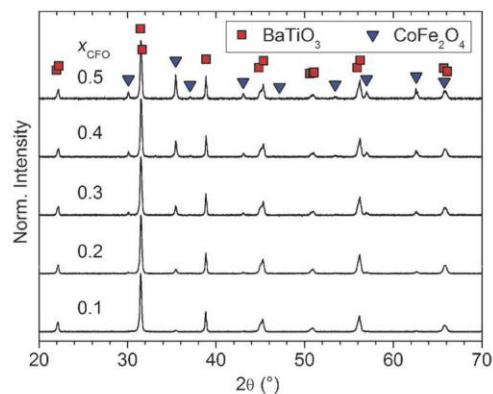


Fig. 5 X-ray diffraction patterns of composites with increasing  $\text{CoFe}_2\text{O}_4$  content.

of the  $\text{BaTiO}_3$  matrix were determined as  $a = 3.9997(6)$  and  $c = 4.0254(8)$  for all samples. Indicating a homogeneous composition independent of  $x_{\text{CFO}}$ . Thus, by reductive sintering and subsequent reoxidation, the formation of impurities as  $\text{BaFe}_{12}\text{O}_{19}$  can be prevented completely and the reaction of  $\text{BaTiO}_3$  with  $\text{Co}^{2+}$  and  $\text{Fe}^{3+}$  is minimized.

It was found that if the disks are too dense after the reductive sintering, the oxidation leads to cracks in the samples due to an increasing volume during the reaction of  $\text{CoFe}_2$  to  $\text{CoFe}_2\text{O}_4$ . The optimal relative densities for reoxidizing (65 to 80%) are dependent on  $x_{\text{CFO}}$  and decrease with higher  $\text{CoFe}_2\text{O}_4$  content. For the final samples relative densities, with respect to the (weighted) single crystal values,<sup>28</sup> between 80% and 90% were achieved.

### 3.3 Photometric $\text{CoFe}_2\text{O}_4$ assay

In Table 1 the results of the photometric  $\text{CoFe}_2\text{O}_4$  quantifications are listed. The uniform deficiency in the  $\text{CoFe}_2\text{O}_4$  content compared to the nominal values is most likely caused by a certain solubility of the Co- and Fe-containing precursors during precipitation and washing of the composite powder. On the other hand the deviation between the expected and measured  $\text{CoFe}_2\text{O}_4$  content is below 2 mol% in most cases and for simplification the nominal percentages are used throughout the text for describing the compositions. Nevertheless, for all calculations with respect to  $x_{\text{CFO}}$ , the experimentally determined contents were used.

### 3.4 SEM and EDX investigations

Scanning electron micrographs were taken from the polished surfaces of sintered samples as shown exemplarily in Fig. 6 for  $x_{\text{CFO}} = 0.1, 0.3$  and  $0.5$ . A minor porosity was observed for all

Table 1  $\text{CoFe}_2\text{O}_4$  contents calculated from photometric iron analysis

Sample	$\text{CoFe}_2\text{O}_4$ mole fraction (mol%)	
	Nominal	Determined
0.1CFO–0.9BTO	10	$8.7 \pm 0.4$
0.2CFO–0.8BTO	20	$18.4 \pm 0.5$
0.3CFO–0.7BTO	30	$28.2 \pm 0.9$
0.4CFO–0.6BTO	40	$37.9 \pm 1.4$
0.5CFO–0.5BTO	50	$46.3 \pm 1.4$

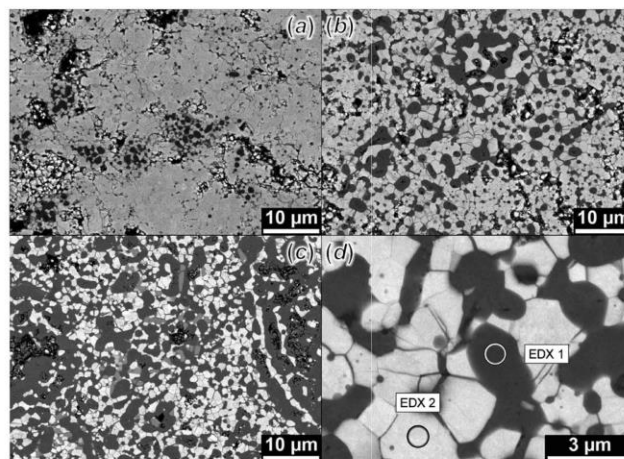


Fig. 6 Scanning electron microscopy images (BSE mode) of polished ceramics: (a)  $x_{\text{CFO}} = 0.1$ ; (b) 0.3; (c) 0.5; (d) position markers for EDX spectra of 0.3CFO–0.7BTO, roughly representing the irradiated surface area.

samples in accordance with the measured densities of 80% to 90%. The pores are distributed randomly throughout the samples. The  $\text{BaTiO}_3$  phase was found to consist of grains with sizes of 1–5  $\mu\text{m}$  independent of  $x_{\text{CFO}}$ . From Fig. 6a it can be seen that for 0.1CFO–0.9BTO isolated  $\text{CoFe}_2\text{O}_4$  grains (dark gray) are embedded in the  $\text{BaTiO}_3$  matrix (light gray) but most of the  $\text{CoFe}_2\text{O}_4$  is assembled in centers of partially interconnected grains separated and surrounded by  $\text{BaTiO}_3$ . With higher  $x_{\text{CFO}}$  values the amount of these  $\text{CoFe}_2\text{O}_4$  clusters increases. In 0.3CFO–0.7BTO only a small portion of the ferrite occurs as isolated particles completely surrounded by  $\text{BaTiO}_3$  (Fig. 6b and d). For  $x_{\text{CFO}} = 0.4$  and  $0.5$  (Fig. 6c), the  $\text{CoFe}_2\text{O}_4$  particles form irregular connected structures that permeate through wide areas, from several 10 to 100  $\mu\text{m}$  in diameter.

To assign the two distinguishable phases in the BSE mode, EDX measurements were carried out at representative sample areas (Fig. 6d). The EDX spectra confirm the formation of two phases, namely  $\text{CoFe}_2\text{O}_4$  and  $\text{BaTiO}_3$ , as can be seen in Fig. 7. The traces of barium and titanium, visible in the  $\text{CoFe}_2\text{O}_4$  spectrum, are due to the large interaction volume of the electron beam compared to the grain size.

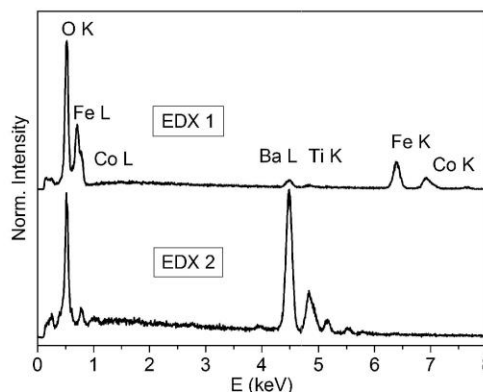


Fig. 7 EDX spectra of 0.3CFO–0.7BTO at the two positions marked in Fig. 6d.



In 0.5CFO–0.5BTO a third phase can be identified in the BSE images from its medium-gray contrast, although no additional reflexes show up in the corresponding X-ray diffraction pattern. EDX-line scans revealed this phase to be slightly oxygen-deficient  $\text{BaTiO}_{3-\delta}$ .

### 3.5 Impedance spectroscopy

In Fig. 8 the temperature dependence of the real part of the permittivities ( $\epsilon'$ ) and the corresponding loss tangents measured at 1 kHz are shown. The  $\epsilon'$  values at 0 °C vary between 476 for  $x_{\text{CFO}} = 0.1$  and 232 for  $x_{\text{CFO}} = 0.5$ . In the measured temperature range the permittivities of  $x_{\text{CFO}} = 0.1$  and 0.2 increase continuously, reaching 5610 and 5068 at 180 °C. For the composite with  $x_{\text{CFO}} = 0.3$  the formation of a broad shoulder at around 150 °C can be seen and  $\epsilon'$  reaches a value of about 4650 at 180 °C. For  $x_{\text{CFO}} = 0.4$  and 0.5, a maximum forms at 150 °C with  $\epsilon'$  values of 4402 and 4447. When measured at frequencies higher than 10 kHz, this maximum at 150 °C is also observed for the samples 0.1CFO–0.9BTO and 0.2CFO–0.8BTO as shown in Fig. 9 for  $f = 1$  MHz. The occurrence of the maximum is accompanied by an increase in the loss tangent and can be assigned to the ferroelectric–paraelectric transition of  $\text{BaTiO}_3$ .<sup>29–32</sup> For large-grained  $\text{BaTiO}_3$  this phase transition occurs at 120 °C.

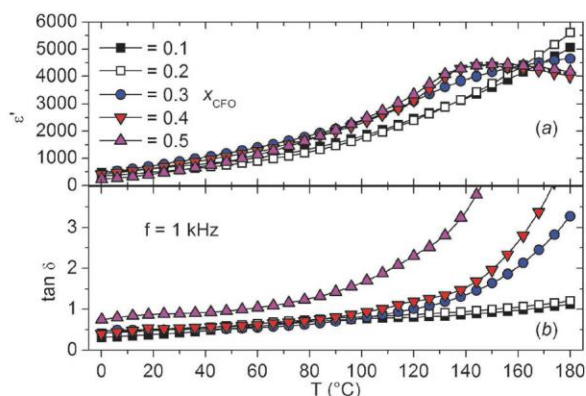


Fig. 8 (a) Temperature dependence of the real part of the permittivity and (b) corresponding loss tangents at 1 kHz.

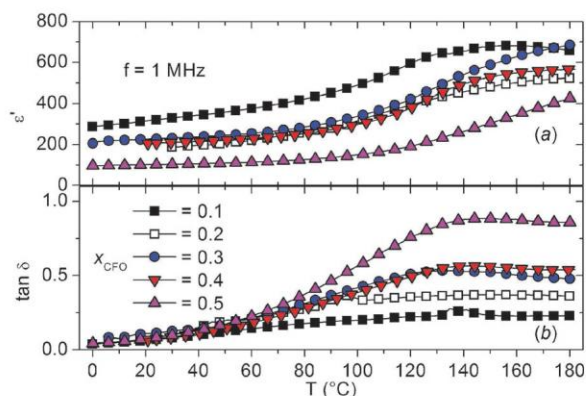


Fig. 9 (a) Temperature dependence of the real part of the permittivity and (b) corresponding loss tangents at 1 MHz.

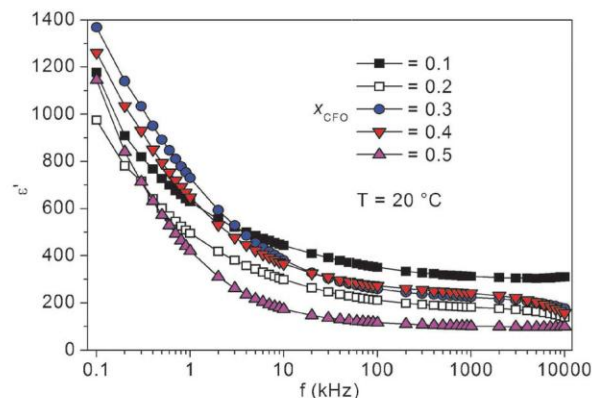


Fig. 10 Frequency dependence of the real part of the permittivities at room temperature.

According to Mitoseriu *et al.* the shift to 150 °C is due to the convolution of extrinsic defect-related dielectric relaxation with the intrinsic ferroelectric component.<sup>33</sup> The presence of the phase transition in the impedance data proves the formation of the tetragonal (ferroelectric)  $\text{BaTiO}_3$  modification in accordance with the XRD results discussed above. The consistent phase transition temperatures hint at a uniform composition of the  $\text{BaTiO}_3$ , indicating that no  $x_{\text{CFO}}$ -dependent doping of  $\text{Co}^{2+}$  or  $\text{Fe}^{3+}$  occurred for any of the samples. The loss tangents at room temperature are below 0.5 with the exception of 0.5CFO–0.5BTO and only slightly increase with temperature below the tetragonal–cubic phase transition of  $\text{BaTiO}_3$ .

Concerning the frequency dependence at room temperature,  $\epsilon'$  decreases rather strongly in the range of roughly 100 Hz–10 kHz and remains quite stable for higher frequencies for all samples, as can be seen in Fig. 10. This phenomenon is typical for electrically conducting particles embedded in an insulating matrix and is called Maxwell Wagner polarization.<sup>34</sup> A similar behavior has already been reported for various  $\text{CoFe}_2\text{O}_4$ – $\text{BaTiO}_3$  composites.<sup>13,35,36</sup>

### 3.6 Magnetic properties

The field dependent magnetization curves of the composites are depicted in Fig. 11. All samples show clear hystereses in accordance with the ferrimagnetism of the spinel component. The saturation magnetization values were determined by a linear extrapolation of the magnetization in the high field ranges (50–90 kOe) to  $H = 0$  Oe. As expected, saturation and remanent magnetization increase with  $\text{CoFe}_2\text{O}_4$  content.

Normalizing these magnetization values with respect to the ferrite content (*i.e.*  $\text{emu g}^{-1}$  of  $\text{CoFe}_2\text{O}_4$ ), as shown in Fig. 12, reveals a small maximum of  $M_{\text{R}}$  with a value of  $27.0 \text{ emu g}^{-1}$  for  $x_{\text{CFO}} = 0.3$ , while the  $M_{\text{S}}$  data show a general slight increase with higher  $\text{CoFe}_2\text{O}_4$  contents, reflecting the increasing ferrite particle sizes. Coercivity fields increase from 1060 Oe (0.1CFO–0.9BTO) to a maximum of 1230 Oe for  $x_{\text{CFO}} = 0.2$  and decreases with higher  $\text{CoFe}_2\text{O}_4$  contents down to a minimum of 970 Oe for  $x_{\text{CFO}} = 0.5$ . It is commonly known that coercivity values for  $\text{CoFe}_2\text{O}_4$  are dependent on its grain shape and structure. Therefore, the change in coercivity is probably due



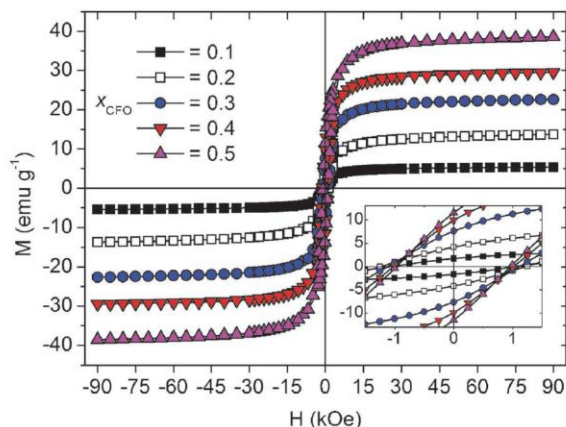


Fig. 11 Field dependent magnetization hysteresis curves measured at 300 K. The inset shows a magnification of the low field region.

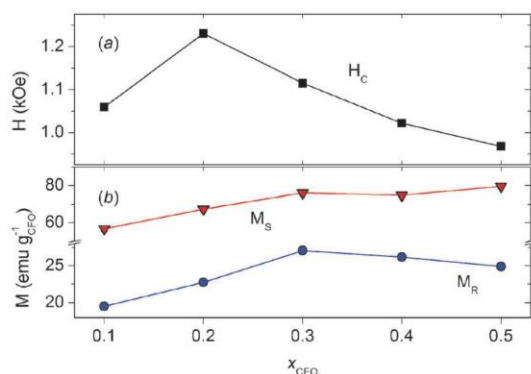


Fig. 12 (a) Magnetic coercive fields and (b) saturation and remanent magnetization at 300 K.

to the formation of  $\text{CoFe}_2\text{O}_4$  clusters and interconnected structures with increasing  $x_{\text{CFO}}$  values (see SEM part).

### 3.7 Magnetolectric coupling

An example of the magnetic DC field dependence of the magnetolectric coefficient  $\alpha_{\text{ME}}$  is shown in Fig. 13 for the composite with  $x_{\text{CFO}} = 0.4$ . For all samples, the  $\alpha_{\text{ME}}$  values show maxima/minima around  $\pm 2.5$  kOe and clear hysteretic behavior with coercive fields between  $\pm 400$  and  $\pm 600$  Oe as well as distinct remanent  $\alpha_{\text{ME}}$  values of  $\pm 7$  to  $\pm 150$   $\mu\text{V Oe}^{-1} \text{cm}^{-1}$ . Thus, the sign of  $\alpha_{\text{ME}}$  is switchable with the direction of the applied magnetic DC field.

It is remarkable that the maximum values of  $\alpha_{\text{ME}}$  at  $\pm 2.5$  kOe are dependent on the history of the magnetic DC field. Upon increasing the DC field strength (both in positive and negative direction), the  $\alpha_{\text{ME}}$  values are higher than for decreasing field strengths. For example, in the case of  $x_{\text{CFO}} = 0.4$  the maximum  $\alpha_{\text{ME}}$  value is  $420$   $\mu\text{V Oe}^{-1} \text{cm}^{-1}$  when the magnetic field is increased up to 10 kOe (red circles, Fig. 13), whereas  $\alpha_{\text{ME}(\text{max})}$  amounts to only  $337$   $\mu\text{V Oe}^{-1} \text{cm}^{-1}$  when the field strength is lowered down from 10 kOe (blue diamonds, Fig. 13). To the best of our knowledge, such an effect has not yet been described for  $\alpha_{\text{ME}}$  and its origin needs to be investigated in further experiments.

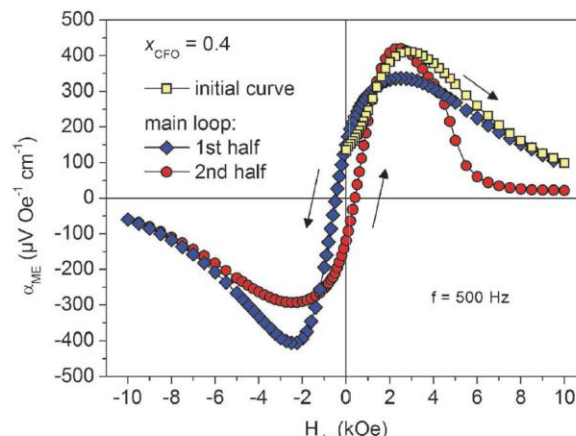


Fig. 13 Magnetic DC field dependent magnetolectric coefficient of  $0.4\text{CFO}-0.6\text{BTO}$ .

A comparison between the magnetic and ME hystereses (Fig. 14) reveals that the ME coercivities are about half the size of the magnetic coercivities, *i.e.* the ME voltage diminishes although magnetization still exists. It is noteworthy that the DC field at which the maximum  $\alpha_{\text{ME}}$  is observed ( $\pm 2.5$  kOe) shows no obvious relation to the characteristic points of the magnetic hysteresis. In particular, it is much smaller than the saturation field (roughly  $\pm 20$  kOe) and also significantly different from the inflection points of magnetization which occur at about  $\pm 1$  kOe. It seems that the ME effect is more affected by magnetostriction. For example, van Run *et al.* found the highest ME values at the maximum of the piezomagnetic strain per Oe.<sup>37</sup> In laminated PZT–Terfenol-D systems, ME maxima were found at the saturation point of the magnetostrictive strain<sup>38</sup> and at the maximum of the piezomagnetic coefficient.<sup>39</sup>

Our paper is one of the few examples in which a hysteretic behavior of the ME coefficient is reported for  $\text{CoFe}_2\text{O}_4$ – $\text{BaTiO}_3$  composites.<sup>37,40–43</sup> In the majority of articles (*e.g.* ref. 13 and 44–47),  $\alpha_{\text{ME}}$  values were found to be zero when the magnetic DC field was switched off, or only initial curves, *i.e.* without cycling of  $H_{\text{dc}}$ , were published.

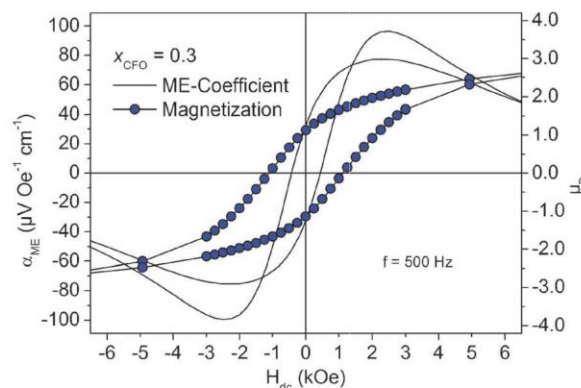


Fig. 14 Comparison of magnetic and magnetolectric hystereses of  $0.3\text{CFO}-0.7\text{BTO}$ .



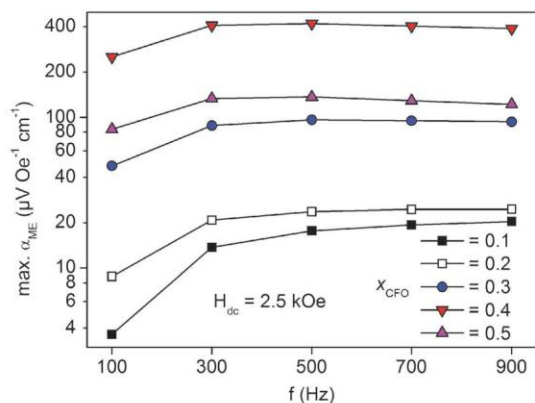


Fig. 15 Frequency dependence ( $H_{ac}$ ) of the maximal ME coefficients.

Fig. 15 shows the maximum  $\alpha_{ME}$  values for the investigated samples depending on  $x_{CFO}$  and the frequency of  $H_{ac}$ . The  $\alpha_{ME}$  values increase with higher  $CoFe_2O_4$  contents up to a maximum at  $x_{CFO} = 0.4$  with  $420 \mu V Oe^{-1} cm^{-1}$  at 500 Hz and decrease again for  $x_{CFO} = 0.5$  at all investigated frequencies. The magnetolectric remanences follow this trend and the sample 0.4CFO–0.6BTO shows the highest remanent  $\alpha_{ME}$  value with  $150 \mu V Oe^{-1} cm^{-1}$ . The maximum  $\alpha_{ME}$  values are within the typical range of a few  $\mu V Oe^{-1} cm^{-1}$  to some  $mV Oe^{-1} cm^{-1}$  reported for  $CoFe_2O_4$ – $BaTiO_3$  composites with 0–3 connectivity measured under similar conditions.<sup>13–15,41,43</sup>

ME measurements at five different  $H_{ac}$  frequencies showed that  $\alpha_{ME}$  is significantly lower for  $f = 100$  Hz than for higher frequencies, while for frequencies from 300 to 900 Hz the obtained  $\alpha_{ME}$  values show only little deviations. This is in contrast to previously reported frequency dependencies where  $\alpha_{ME}$  values increase more or less linearly up to 1 kHz.<sup>44,45</sup> Other articles show a giant increase of  $\alpha_{ME}$  (up to  $2.5 V Oe^{-1} cm^{-1}$ ) under resonance conditions in the range between 15 and 430 kHz.<sup>46–48</sup> Measurements at such higher frequencies are therefore planned for the future.

## 4. Conclusions

In multiferroic composites, the strength of the magnetolectric coupling depends on the quality of the interface and therefore an intimate contact between the two components is mandatory. Because of the low sintering activity of  $BaTiO_3$ , such high-quality interfaces require high sintering temperatures, which usually lead to the formation of secondary phases like  $BaFe_{12}O_{19}$  and/or ionic exchanges like the incorporation of iron or cobalt ions in  $BaTiO_3$ . To avoid these problems we describe a new approach starting with the polyol-assisted soft-chemistry preparation of a  $CoFe_2O_4$ – $BaTiO_3$  composite precursor consisting of submicrometer-sized particles. This composite powder is sintered under a reducing atmosphere, resulting in  $CoFe_2$ – $BaTiO_3$  composites. In a final reaction step these ceramics are reoxidized under mild conditions leading to the final dense  $CoFe_2O_4$ – $BaTiO_3$  composites ( $\geq 80\%$  of the crystallographic density), which according to XRD are completely free of secondary phases.

The presence of tetragonal  $BaTiO_3$  with lattice parameters independent of the ferrite fraction further indicates that no considerable amounts of  $Co^{2+}$  or  $Fe^{3+}$  are incorporated in  $BaTiO_3$ . This finding is additionally corroborated by dielectric measurements showing the occurrence of the ferroelectric–paraelectric phase transition, which is shifted to  $150^\circ C$  probably due to defect-related dielectric relaxations. EDX investigations gave no hints for secondary phases or detectable Ti/Fe/Co exchange between the two phases. All composites show ferrimagnetic behavior. Their (normalized) saturation magnetizations slightly increase with the  $CoFe_2O_4$  content, reflecting the increasing grain sizes of the ferrite. Field-dependent measurements of the magnetolectric coupling show a hysteresis of  $\alpha_{ME}$  with maxima at DC magnetic fields of  $\pm 2.5$  kOe and remanent  $\alpha_{ME}$  values in the order of  $10$ – $150 \mu V Oe^{-1} cm^{-1}$ . We observed distinct deviations between the coercivities of the magnetic moment and the ME effect, *i.e.* the magnetolectric coupling diminishes already at roughly  $\pm 500$  Oe while the required field to extinct the magnetization is about twice as high. Concerning the effect of the  $H_{ac}$  frequency, we found almost constant  $\alpha_{ME}$  values from 300 Hz to 900 Hz while the magnetolectric coupling is much smaller at 100 Hz. In addition, an increase of the ME effect with increasing  $CoFe_2O_4$  content was observed leading to a maximum in the order of  $400 \mu V Oe^{-1} cm^{-1}$  for  $x = 0.4$ . With a higher ferrite content,  $\alpha_{ME}$  decreases again. Most interestingly, for all samples we observed strong differences for the maximum  $\alpha_{ME}$  values depending on the direction of the magnetic dc-field sweep. When the field strength is increased (both in positive and negative directions) the maximum ME values are up to 20% larger than upon decreasing  $H_{dc}$ . Thus, the measured ME voltages of the  $CoFe_2O_4$ – $BaTiO_3$  composites not only depend on the  $H_{dc}$  field strength but also on its history. This ‘memory effect’ may give rise to additional future applications.

## Acknowledgements

The authors thank F. Syrowatka for the SEM investigations and Th. Müller for TGA experiments. Financial support by the German Research Foundation within the Collaborative Research Centre SFB 762 *Functionality of Oxide Interfaces* is gratefully acknowledged.

## References

- 1 N. A. Spaldin and M. Fiebig, *Science*, 2005, **309**, 391–392.
- 2 M. Bibes and A. Barthélémy, *Nat. Mater.*, 2008, **7**, 425–426.
- 3 J. Ma, J. Hu, Z. Li and C.-W. Nan, *Adv. Mater.*, 2011, **23**, 1062–1087.
- 4 N. Ortega, A. Kumar, J. F. Scott and R. S. Katiyar, *J. Phys.: Condens. Matter*, 2015, **27**, 504002.
- 5 W. Eerenstein, N. D. Mathur and J. F. Scott, *Nature*, 2006, **442**, 759–765.
- 6 J. van den Boomgaard, D. R. Terrell, R. A. J. Born and H. F. J. I. Giller, *J. Mater. Sci.*, 1974, **9**, 1705–1709.
- 7 C.-W. Nan, *Phys. Rev. B: Condens. Matter Mater. Phys.*, 1994, **50**, 6082–6088.



- 8 M. Avellaneda and G. Harshé, *J. Intell. Mater. Syst. Struct.*, 1994, **5**, 501–513.
- 9 M. I. Bichurin, V. M. Petrov and G. Srinivasan, *J. Appl. Phys.*, 2002, **92**, 7681–7683.
- 10 J. Ryu, S. Priya, K. Uchino and H.-E. Kim, *J. Electroceram.*, 2002, **8**, 107–119.
- 11 R. E. Newnham, D. P. Skinner and L. E. Cross, *Mater. Res. Bull.*, 1978, **13**, 525–536.
- 12 C.-W. Nan, M. I. Bichurin, S. Dong, D. Viehland and G. Srinivasan, *J. Appl. Phys.*, 2008, **103**, 031101.
- 13 R. P. Mahajan, K. K. Patankar, M. B. Kothale, S. C. Chaudhari, V. L. Mathe and S. A. Patil, *Pramana*, 2002, **58**, 1115–1124.
- 14 G. Schileo, *Prog. Solid State Chem.*, 2013, **41**, 87–98.
- 15 A. Baji, Y.-W. Mai, R. Yimnirun and S. Unruan, *RSC Adv.*, 2014, **4**, 55217–55223.
- 16 J. S. Andrew, J. D. Starr and M. A. K. Budi, *Scr. Mater.*, 2014, **74**, 38–43.
- 17 X. Chen and G. Tan, 2012, arXiv:1201.3963 [cond-mat.mtrl-sci].
- 18 T. Kimura, *Annu. Rev. Condens. Matter Phys.*, 2012, **3**, 93–110.
- 19 Z. Dong, Y. Pu, Z. Gao, P. Wang, X. Liu and Z. Sun, *J. Eur. Ceram. Soc.*, 2015, **35**, 3513–3520.
- 20 J. D. S. Guerra, S. Betal, M. Pal, J. E. Garcia, A. J. A. Oliveira, J.-C. M'Peko, A. C. Hernandez, R. Guo and A. S. Bhalla, *J. Am. Ceram. Soc.*, 2015, **98**, 1542–1547.
- 21 N. Koga and T. Tsutaoka, *J. Magn. Magn. Mater.*, 2007, **313**, 168–175.
- 22 T. Tsutaoka and N. Koga, *J. Magn. Magn. Mater.*, 2013, **325**, 36–41.
- 23 D. Caruntu, Y. Remond, N. H. Chou, M.-J. Jun, G. Caruntu, J. He, G. Goloverda, C. O'Connor and V. Kolesnichenko, *Inorg. Chem.*, 2002, **41**, 6137–6146.
- 24 M. Siemons, T. Weirich, J. Mayer and U. Simon, *Z. Anorg. Allg. Chem.*, 2004, **630**, 2083–2089.
- 25 S. Gablenz, H.-P. Abicht, E. Pippel, O. Lichtenberger and J. Woltersdorf, *J. Eur. Ceram. Soc.*, 2000, **20**, 1053–1060.
- 26 V. Ischenko, E. Pippel, R. Köferstein, H.-P. Abicht and J. Woltersdorf, *Solid State Sci.*, 2007, **9**, 21–26.
- 27 V. Ischenko, J. Woltersdorf, E. Pippel, R. Köferstein and H.-P. Abicht, *Solid State Sci.*, 2007, **9**, 303–309.
- 28 G. W. Marks and L. A. Monson, *Ind. Eng. Chem.*, 1955, **47**, 1611–1620.
- 29 A. Hanumaiah, T. Bhimasankaram, S. V. Suryanarayana and G. S. Kumar, *Bull. Mater. Sci.*, 1994, **17**, 405–409.
- 30 K. Raidongia, A. Nag, A. Sundaresan and C. N. R. Rao, *Appl. Phys. Lett.*, 2010, **97**, 062904.
- 31 A. Gupta and R. Chatterjee, *J. Eur. Ceram. Soc.*, 2013, **33**, 1017–1022.
- 32 R. Köferstein and S. G. Ebbinghaus, *RSC Adv.*, 2015, **5**, 71491–71499.
- 33 L. Mitoseriu and V. Buscaglia, *Phase Transitions*, 2006, **79**, 1095–1121.
- 34 K. W. Wagner, *Arch. Elektrotech.*, 1914, **2**, 371–387.
- 35 J. Nie, G. Xu, Y. Yang and C. Cheng, *Mater. Chem. Phys.*, 2009, **115**, 400–403.
- 36 L. M. Hrib and O. F. Caltun, *J. Alloys Compd.*, 2011, **509**, 6644–6648.
- 37 A. M. J. G. van Run, D. R. Terrell and J. H. Scholing, *J. Mater. Sci.*, 1974, **9**, 1710–1714.
- 38 S. Dong, J.-F. Li and D. Viehland, *J. Appl. Phys.*, 2004, **95**, 2625–2630.
- 39 C. P. Zhao, F. Fang and W. Yang, *Smart Mater. Struct.*, 2010, **19**, 125004.
- 40 J. van den Boomgaard, A. M. J. G. Van Run and J. Van Suchtelen, *Ferroelectrics*, 1976, **10**, 295–298.
- 41 M. E. Botello-Zubiate, D. Bueno-Baqués, J. de Frutos Vaquerizo, L. E. Fuentes Cobas and J. A. Matutes-Aquino, *Ferroelectrics*, 2006, **338**, 247–253.
- 42 G. V. Duong, R. Groessinger and R. Sato Turtelli, *J. Magn. Magn. Mater.*, 2007, **310**, 1157–1159.
- 43 G. V. Duong, R. S. Turtelli and R. Groessinger, *J. Magn. Magn. Mater.*, 2010, **322**, 1581–1584.
- 44 A. Khamkongkaeo, P. Jantaratana, C. Sirisathitkul, T. Yamwong and S. Maensiri, *Trans. Nonferrous Met. Soc. China*, 2011, **21**, 2438–2442.
- 45 H. Yang, G. Zhang and Y. Lin, *J. Alloys Compd.*, 2015, **644**, 390–397.
- 46 W. P. Wang, H. Yang, T. Xian and R. C. Yu, *Chem. Phys. Lett.*, 2015, **618**, 72–77.
- 47 R. A. Islam, M. Bichurin and S. Priya, in *Ferroelectrics – Characterization and Modeling*, ed. M. Lallart, InTech, 2011, pp. 61–78.
- 48 S. Q. Ren, L. Q. Weng, S.-H. Song, F. Li, J. G. Wan and M. Zeng, *J. Mater. Sci.*, 2005, **40**, 4375–4378.





**A3** Novel magnetoelectric composites of cobalt iron alloy and barium titanate

Reprinted with the permission of the American Ceramic Society and Blackwell Publishing.

## ORIGINAL ARTICLE

# Novel magnetoelectric composites of cobalt iron alloy and barium titanate

Till Walther  | Roberto Köferstein | Stefan G. Ebbinghaus

Institute of Chemistry, Martin Luther University Halle-Wittenberg, Halle/Saale, Germany

**Correspondence**

Stefan G. Ebbinghaus, Institute of Chemistry, Martin Luther University Halle-Wittenberg, Halle/Saale, Germany.  
Email: stefan.ebbinghaus@chemie.uni-halle.de

**Funding information**

Deutsche Forschungsgemeinschaft, Grant/Award Number: SFB 762

**Abstract**

Magnetoelectric barium titanate ceramics with embedded cobalt iron alloy particles  $(\text{Co}_{1/3}\text{Fe}_{2/3})_x-(\text{BaTiO}_3)_{(1-x)}$ , with  $x=0.2, 0.4,$  and  $0.6$ , were prepared by a polyol-mediated synthesis with subsequent sintering in a reducing forming gas atmosphere. The samples were characterized by XRD and SEM/EDX measurements. The sizes of the  $\text{Co}_{1/3}\text{Fe}_{2/3}$  grains increase with  $x$ . Impedance spectroscopy showed a behavior similar to pure  $\text{BaTiO}_3$ , in particular the occurrence of the ferroelectric-paraelectric phase transition, and high permittivities for the sample with  $x=0.6$ , that is, near the percolation threshold. The samples exhibit soft ferromagnetic properties with large saturation magnetizations of  $2.5 \mu_B/\text{atom}$  and narrow hystereses. Detailed magnetoelectric investigations revealed a unique DC-field dependence of  $\alpha_{\text{ME}}$  for all three compositions. Most remarkably, the sample with  $x=0.4$  possesses a broad ME hysteresis and an inversion of the sign of  $\alpha_{\text{ME}}$  at 5 kOe.

**KEYWORDS**

barium titanate, cobalt iron alloy, magnetoelectric effect, metal-ceramic composite, multiferroic

## 1 | INTRODUCTION

Materials that exhibit at least two ferroic order phenomena are called multiferroics.<sup>1</sup> Of these, magnetoelectrics with a coupling between magnetostrictive and piezoelectric properties are of special interest because they allow the manipulation of magnetization with electric fields and/or of the polarization by magnetic fields.<sup>2</sup> Since this field of science was initiated, the hunt for high or unusual magnetoelectric coupling effects is on. To date, many compositions and connectivities of compounds have been investigated both theoretically and experimentally. So far one of the most promising combinations are layered composites of ferro-/ferromagnetic metals/alloys with ferroelectric perovskites.<sup>3,4</sup> They exhibit magnetoelectric coefficients ( $\alpha_{\text{ME}}$ ) ranging from a few  $\text{mV Oe}^{-1} \text{cm}^{-1}$  at low  $H_{\text{AC}}$  frequencies up to several  $\text{V Oe}^{-1} \text{cm}^{-1}$  at resonance conditions (several kHz, depending on the system).<sup>5-9</sup> In addition, magnetoelectric effects of ferroelectric thin films with embedded metal particles have been investigated.<sup>10,11</sup> In contrast, no magnetoelectric investigations on 0-3 metal-perovskite ceramics have

been reported yet, although various synthesis routes for metal-ceramic composites are described in the literature.<sup>12-18</sup>

In this study, the first detailed magnetoelectric investigations on 0-3 composites of  $\text{Co}_{1/3}\text{Fe}_{2/3}$  in combination with  $\text{BaTiO}_3$  are reported. Samples with varying  $\text{Co}_{1/3}\text{Fe}_{2/3}$  content ( $x=0.2, 0.4$  and  $0.6$ ) were prepared by a polyol-mediated synthesis with subsequent calcination and sintering under reducing conditions.  $\text{BaTiO}_3$  is widely investigated for magnetoelectric composites and is used as piezoelectric matrix component. The alloy of cobalt and iron with a molar ratio of Co:Fe 1:2 was chosen as metallic component because it shows high magnetostriction and the highest saturation magnetization of 3d metal alloys.<sup>19-21</sup>

## 2 | EXPERIMENTAL SECTION

### 2.1 | Material preparation

Three composite samples  $(\text{Co}_{1/3}\text{Fe}_{2/3})_x-(\text{BaTiO}_3)_{(1-x)}$  with  $x=0.2, 0.4,$  and  $0.6$  were synthesized in a procedure similar to the one reported in Ref.<sup>22</sup>

In a first step, Co(II) and Fe(III) nitrates (molar ratio 1:2) were dissolved in water and diethylene glycol (DEG) with  $[\text{Co}^{2+}] = 40 \text{ mmol L}^{-1}$ . The solution was heated under reflux for 1 hour. After cooling to room temperature, acetone was added and the precipitate was centrifuged, washed with acetone and dried, resulting in a brown powder. Appropriate amounts of this precursor were suspended in stoichiometric solutions of titanium isopropoxide and barium hydroxide in DEG with  $[\text{Ba}^{2+}] = [\text{Ti}^{4+}] = 40 \text{ mmol L}^{-1}$ . After heating under reflux for 1 hour, the reaction mixture was cooled to room temperature. Addition of acetone produced a gray precipitate that was centrifuged, washed with acetone, and dried. This powder was calcined at  $700^\circ\text{C}$  in static air (1 hour), followed by a reduction in flowing forming gas ( $80 \text{ mL min}^{-1}$ , 10%  $\text{H}_2$ , 1 hour) at  $950^\circ\text{C}$ . The resulting gray powder was pressed into disks (100 mg,  $\varnothing = 6 \text{ mm}$ ). Sintering under reducing conditions in forming gas at  $1300^\circ\text{C}$  for 1 hour led to black ceramic bodies with relative densities (with respect to the weighted single crystal values<sup>23</sup>) of  $\rho \approx 85\%$ .

## 2.2 | Characterization

Room-temperature X-ray diffraction patterns of crushed samples were recorded on a Bragg-Brentano diffractometer (D8 Advance, Bruker Corporation, Billerica, MA, USA) operating with  $\text{CuK}\alpha$  radiation. Scanning electron microscope images in backscattered electron (BSE) mode and EDX spectra were recorded with 15 kV acceleration voltage (Phenom ProX, Phenom-World B.V., Eindhoven, the Netherlands). Grain sizes were derived from SEM images of several areas of each ceramic. The values given below are the lower and upper limits and the average grain sizes. For impedance measurements, GaIn alloy was coated on top and bottom surfaces of the ceramic bodies as electrodes. The temperature- and frequency-dependent impedance spectra ( $0^\circ\text{C}$ - $180^\circ\text{C}$ ;  $10^2$ - $10^7 \text{ Hz}$ ) were recorded with an impedance analyzer (4192A, Hewlett-Packard, Palo Alto, CA, USA). Magnetic measurements were carried out using the ACMS option (PPMS 9, Quantum Design Inc., San Diego, CA, USA). Hysteresis loops were measured at 300 K with a cycling of the magnetic DC field between +90 and -90 kOe. For magnetoelectric investigations, 100 nm gold electrodes were sputtered onto the sample surfaces (Sputter Coater 108auto, Cressington Scientific Instruments Ltd., Watford, UK). Electric poling was done applying a DC field of  $6.5 \text{ kV cm}^{-1}$  at room temperature. The samples were heated to  $200^\circ\text{C}$  (i.e., above  $T_C$  of  $\text{BaTiO}_3$ ) for 1 hour (heating rate  $10 \text{ K min}^{-1}$ ). During heating and cooling the electric field was maintained but adjusted dynamically to a current limit of 0.1 mA. After poling, the samples were short circuited for 10 minutes. The ME measurements were performed at 300 K using a

custom-made setup based on the AC-transport measurement option (PPMS 9, Quantum Design Inc., San Diego, CA, USA). A magnetic AC field of  $H_{AC} = 10 \text{ Oe}$  with different frequencies was applied by a solenoid with 1160 loops of copper wire. The ME voltage was measured in dependence of the magnetic DC field upon cycling between +10 and -10 kOe. Magnetic AC and DC fields were aligned parallel to the electric polarization direction as shown in Figure S1. Raw data were corrected for eddy currents measured on an empty sample holder. Since voltages caused by induction show a  $90^\circ$  phase shift with respect to  $H_{AC}$ , only the real part of the measured voltage was considered. The magnetoelectric coefficient was calculated as  $\alpha_{ME} = U_{ME} / (H_{AC} \cdot h)$  with  $h$  being the sample height.

## 3 | RESULTS AND DISCUSSION

### 3.1 | Composition and morphology

X-ray diffraction was used to investigate the reaction products at different stages of the synthesis as shown exemplarily for  $0.6\text{Co}_{1/3}\text{Fe}_{2/3}$ - $0.4\text{BaTiO}_3$  in Figure S2. Directly after precipitation  $\text{BaCO}_3$  is the sole crystalline component. Calcination in air at  $700^\circ\text{C}$  leads to the formation of  $\text{CoFe}_2\text{O}_4$  and  $\text{BaTiO}_3$  but a significant amount of  $\text{BaCO}_3$  remains in the powder.

An additional reducing step in forming gas was introduced because the direct sintering of the air-calcined powder leads to porous ceramic bodies owing to the release of  $\text{CO}_2$  from the residual  $\text{BaCO}_3$ . The temperature of  $950^\circ\text{C}$  was chosen to completely decompose  $\text{BaCO}_3$  while preserving a high sintering activity of the powder. The corresponding diffractogram (Figure S2 c) reveals that only  $\text{Co}_{1/3}\text{Fe}_{2/3}$  and  $\text{BaTiO}_3$  are present in the reduced powder.

The reducing forming gas atmosphere was also used during sintering. At  $1300^\circ\text{C}$  the samples reach a relative density of 85% after 1 hour. As depicted in Figure 1, phase pure  $(\text{Co}_{1/3}\text{Fe}_{2/3})_x - (\text{BaTiO}_3)_{(1-x)}$  composites were obtained for all three compositions and the tetragonal modification of  $\text{BaTiO}_3$  is formed.

For morphological investigations, SEM images of the final samples were taken and EDX spectra were recorded. The results are depicted in Figure 2.

In all samples the sizes of the  $\text{BaTiO}_3$  grains range from  $0.5 \mu\text{m}$  to  $5 \mu\text{m}$ , with the majority of grains being about  $2 \mu\text{m}$  in diameter. There are two types of  $\text{Co}_{1/3}\text{Fe}_{2/3}$ -particle distributions in the composites. In all samples isolated grains with a size of 1-2  $\mu\text{m}$  are present. These are completely surrounded by the  $\text{BaTiO}_3$  matrix. The second sort of  $\text{Co}_{1/3}\text{Fe}_{2/3}$  particles form larger interconnected areas. With increasing  $x$ , the fraction of the latter becomes larger: while for  $x = 0.2$  most of the  $\text{Co}_{1/3}\text{Fe}_{2/3}$  consists of isolated grains, for  $x = 0.6$  almost the entire alloy grains are merged

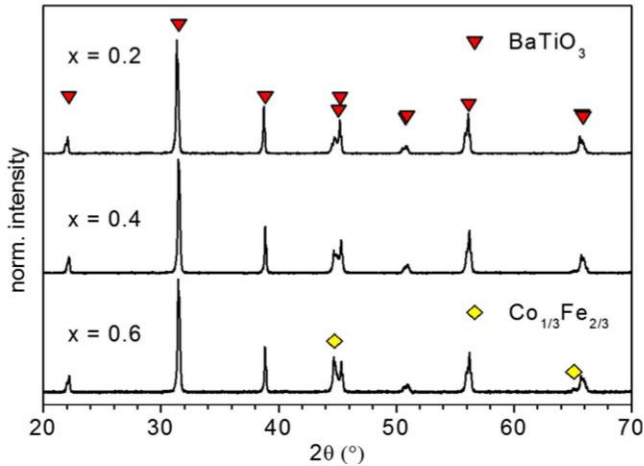


**FIGURE 1** XRD patterns of  $(\text{Co}_{1/3}\text{Fe}_{2/3})_x(\text{BaTiO}_3)_{(1-x)}$  composites sintered at  $1300^\circ\text{C}$  with increasing  $\text{Co}_{1/3}\text{Fe}_{2/3}$  content [Color figure can be viewed at [wileyonlinelibrary.com](http://wileyonlinelibrary.com)]

and form structures of up to  $4\ \mu\text{m}$  in width and  $>10\ \mu\text{m}$  in length.

EDX measurements clearly show the formation of the two distinct phases. No traces of Co or Fe were found in

the  $\text{BaTiO}_3$  matrix. On the other hand, small Ba and Ti signals appear in the  $\text{Co}_{1/3}\text{Fe}_{2/3}$  spectra because of the large interaction volume of the electron beam compared to the size of the  $\text{Co}_{1/3}\text{Fe}_{2/3}$  grains.

### 3.2 | Dielectric measurements

The dielectric properties of  $\text{BaTiO}_3$  ceramics depend on their densities and (more important) on the grain sizes. As mentioned above, these parameters are very similar for all three compositions allowing a meaningful comparison. The general behavior of the real parts of the permittivity ( $\epsilon_r$ ) resembles the one of pure  $\text{BaTiO}_3$  in the entire frequency range ( $10^2$  to  $10^7$  Hz). In Figure S3 of the supplementary, the temperature dependence of  $\epsilon_r$  and the dissipation factor of the composites are shown exemplarily for  $f=1$  kHz. The  $\epsilon_r$  graphs exhibit maxima at the transition from the ferro- to the paraelectric phase of  $\text{BaTiO}_3$  around  $T_C \approx 125^\circ\text{C}$ . At  $20^\circ\text{C}$ , the  $\epsilon_r$  values for  $x=0.2$  and  $0.4$  are very similar and almost constant over a wide frequency range (see Figure S4). In contrast, for  $0.6\text{Co}_{1/3}\text{Fe}_{2/3}-0.4\text{BaTiO}_3$  the permittivity at low frequencies is up to five times higher than

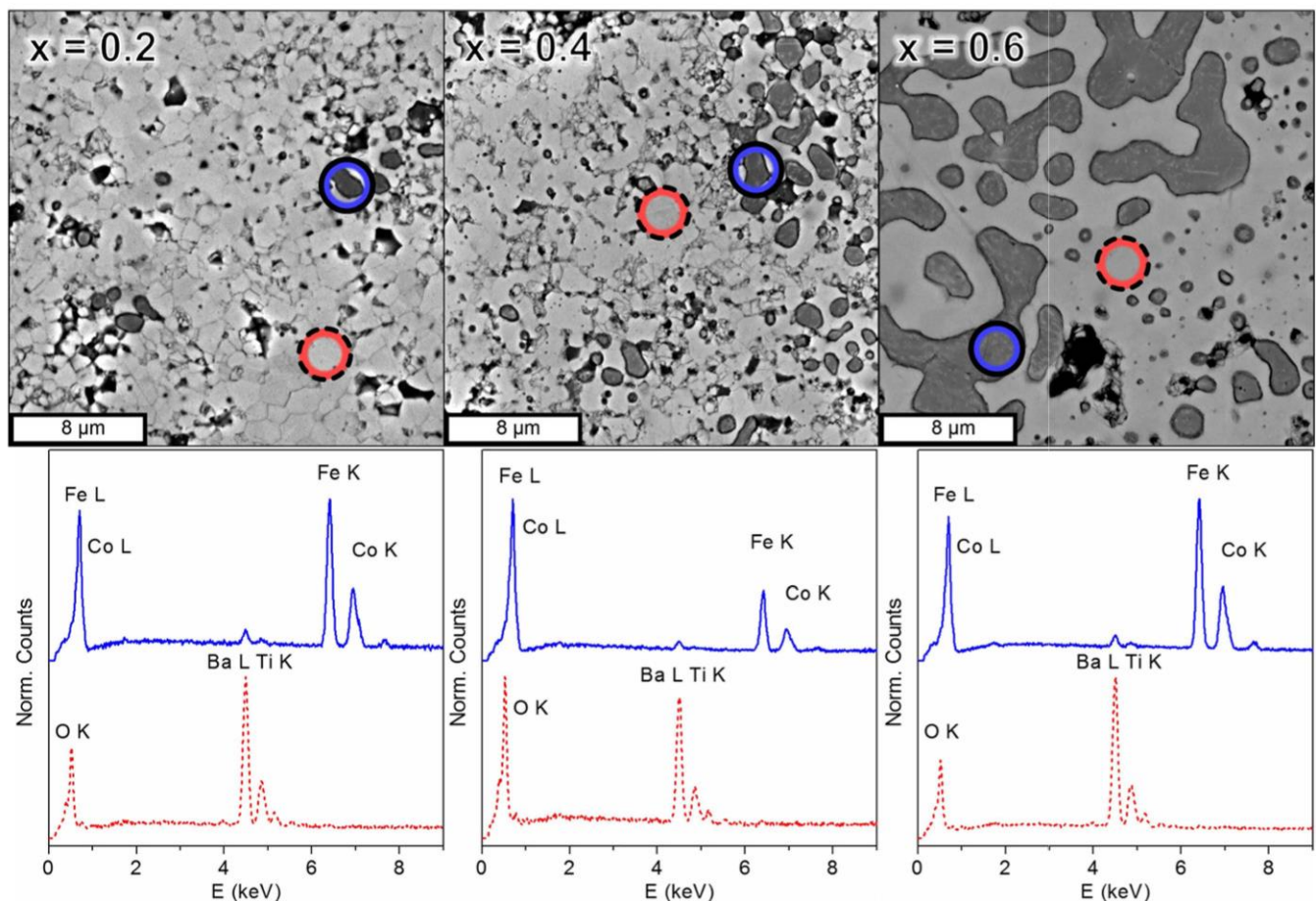


**FIGURE 2** SEM images in BSE mode with position markers of the corresponding EDX spectra of  $(\text{Co}_{1/3}\text{Fe}_{2/3})_x(\text{BaTiO}_3)_{(1-x)}$  composites with increasing  $x$  [Color figure can be viewed at [wileyonlinelibrary.com](http://wileyonlinelibrary.com)]

for the other two samples. In addition,  $\epsilon_r$  shows a pronounced frequency dependence and strongly decreases above  $10^6$  Hz. The enhancement of the dielectric constant at low frequencies is known for metal-BaTiO<sub>3</sub> ceramics with compositions close to the percolation threshold.<sup>14,18</sup> A theoretical description is given in.<sup>24</sup>

Up to  $T_C$  the dissipation factors increase only slightly with temperature, whereas above  $130^\circ\text{C}$  the samples get more conductive and  $\tan \delta$  increases. At room temperature, the  $\tan \delta$  values are quite stable up to  $f=100$  kHz but increase considerably with higher frequencies. Over the measured temperature and frequency ranges, the dissipation factors for  $x=0.2$  and  $0.4$  are roughly of the same magnitude, whereas  $\tan \delta$  is remarkably higher for  $x=0.6$ .

In contrast to composites of BaTiO<sub>3</sub> with ferrite spinels, the influence of the Co<sub>1/3</sub>Fe<sub>2/3</sub> alloy on the dielectric properties is comparatively low.<sup>22</sup> Usually, ferrite-BaTiO<sub>3</sub> composites show Maxwell-Wagner-like frequency and temperature dependencies of  $\epsilon_r$  that are distinctively different from pure BaTiO<sub>3</sub>.<sup>25–27</sup> The Co<sub>1/3</sub>Fe<sub>2/3</sub>-BaTiO<sub>3</sub> composites, on the other hand, show only little deviations compared to pure BaTiO<sub>3</sub>. A similar behavior has already been reported for Ni-BaTiO<sub>3</sub> composites.<sup>14</sup>

### 3.3 | Magnetic properties

As shown in Figure 3, all three samples show soft ferromagnetic behavior. The saturation magnetization ( $M_S$ ) of the composites increases linearly with the Co<sub>1/3</sub>Fe<sub>2/3</sub> content. When normalized to  $x$ ,  $M_S$  values of  $2.5 \mu_B/\text{atom}$  are found for all three compositions, which is the maximum saturation magnetization a Co/Fe alloy can reach.<sup>20,28,29</sup> The coercivities ( $H_C$ ) decrease with increasing Co<sub>1/3</sub>Fe<sub>2/3</sub> content (50, 12, 3 Oe for  $x=0.2, 0.4,$  and  $0.6$ ), most likely

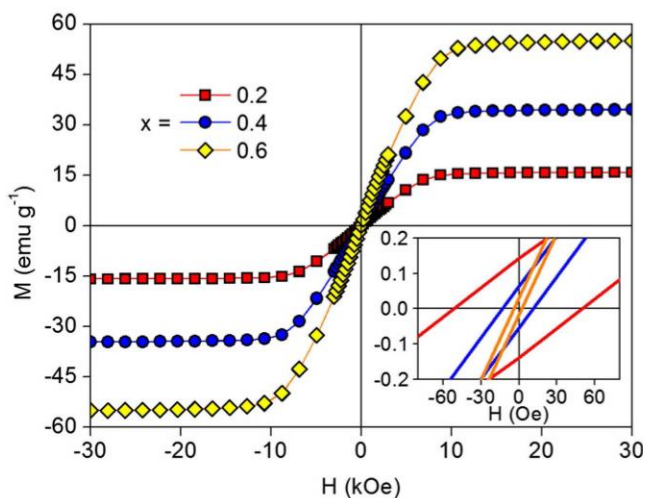


**FIGURE 3** Magnetic field-dependent magnetization hystereses of  $(\text{Co}_{1/3}\text{Fe}_{2/3})_x(\text{BaTiO}_3)_{(1-x)}$  composites [Color figure can be viewed at [wileyonlinelibrary.com](http://wileyonlinelibrary.com)]

because of the larger Co<sub>1/3</sub>Fe<sub>2/3</sub> grain sizes (see SEM part).<sup>30,31</sup> Overall, the composites exhibit the expected magnetic behavior.

### 3.4 | Magnetolectric properties

In this work, the magnetic DC field dependence of the magnetolectric coefficient  $\alpha_{\text{ME}}$  is investigated for the first time for CoFe-BaTiO<sub>3</sub> 0-3 composites. The ME measurements of the three compositions were done at 300 K. The corresponding graphs are shown in Figure 4. Upon increasing  $H_{\text{DC}}$  for  $x=0.2$   $\alpha_{\text{ME}}$  reaches a maximum of  $-100 \mu\text{V Oe}^{-1} \text{cm}^{-1}$  at 5.5 kOe and then decreases to  $-5 \mu\text{V Oe}^{-1} \text{cm}^{-1}$  at 10 kOe. For  $H_{\text{DC}}$  higher than  $\pm 2$  kOe, the courses of  $\alpha_{\text{ME}}$  are identical for both directions of the field sweep. Surprisingly, between  $-2$  and  $+2$  kOe an inverted hysteresis is formed, that is, upon decreasing the (positive) field strength a ME voltage of zero is found already for a positive coercive field, whereas at  $H_{\text{DC}}=0$   $\alpha_{\text{ME}}$  with an opposite sign is observed. As described later this behavior is remarkably different from the one of CoFe<sub>2</sub>O<sub>4</sub>-BaTiO<sub>3</sub> composites.

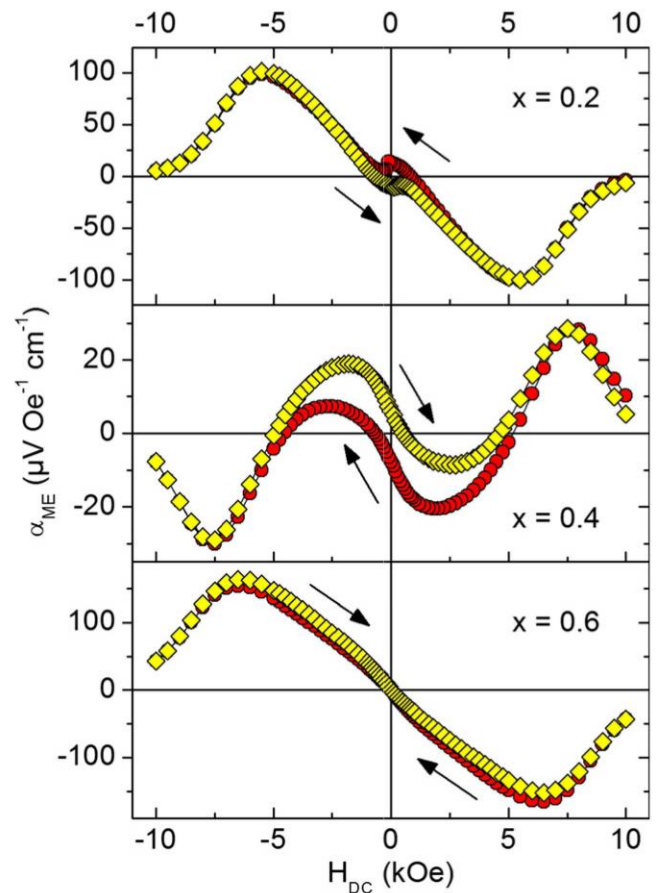


**FIGURE 4** Magnetic field-dependent magnetolectric coefficients  $\alpha_{\text{ME}}$  of  $(\text{Co}_{1/3}\text{Fe}_{2/3})_x(\text{BaTiO}_3)_{(1-x)}$  composites measured at  $f_{\text{AC}}=900$  Hz [Color figure can be viewed at [wileyonlinelibrary.com](http://wileyonlinelibrary.com)]

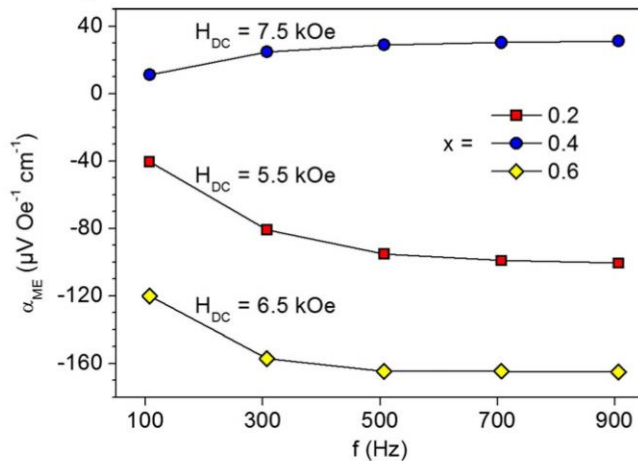


**FIGURE 5** Frequency dependence  $f(H_{AC})$  of the maximal ME coefficients of  $(\text{Co}_{1/3}\text{Fe}_{2/3})_x-(\text{BaTiO}_3)_{(1-x)}$  composites [Color figure can be viewed at [wileyonlinelibrary.com](http://wileyonlinelibrary.com)]

Even more astonishing is the magnetoelectric behavior of  $0.4\text{Co}_{1/3}\text{Fe}_{2/3}-0.6\text{BaTiO}_3$ , which turned out to be completely different from the other two samples as shown in Figure 4. Upon increasing the field to 10 kOe, the magnetoelectric coefficient first exhibits a minimum at 2.5 kOe with  $\alpha_{ME}=-8.5 \mu\text{V Oe}^{-1} \text{cm}^{-1}$ , followed by a maximum of  $+29 \mu\text{V Oe}^{-1} \text{cm}^{-1}$  at 7.5 kOe. The  $\alpha_{ME}$  values at 7.5 kOe are independent of the field sweep direction. In contrast,  $\alpha_{ME}$  at 2.5 kOe is significantly larger ( $-20.5 \mu\text{V Oe}^{-1} \text{cm}^{-1}$ ) when  $H_{DC}$  is decreased from 10 kOe to zero. As a consequence, a broad hysteresis is formed between  $+5$  and  $-5$  kOe.

In the bottom panel of Figure 4, the magnetoelectric behavior for the sample with  $x=0.6$  is shown. The course of  $\alpha_{ME}$  is similar to the one of  $x=0.2$ . The maximum of  $-165 \mu\text{V Oe}^{-1} \text{cm}^{-1}$  at 6.5 kOe observed for  $0.6\text{Co}_{1/3}\text{Fe}_{2/3}-0.4\text{BaTiO}_3$  is the highest  $\alpha_{ME}$  value of the investigated samples. It is noteworthy that no hysteresis occurs for this composition and that the DC field at which the maximum  $\alpha_{ME}$  is reached is about 1 kOe higher than for  $x=0.2$ .

We emphasize that the DC field dependence of the magnetoelectric effect is completely different from composites of  $\text{BaTiO}_3$  in combination with  $\text{CoFe}_2\text{O}_4$  as shown exemplarily in Figure S5 of the supplementary for the composition  $0.5\text{CoFe}_2\text{O}_4-0.5\text{BaTiO}_3$  (please note that the sample was obtained from oxidation of a  $\text{Co}_{1/3}\text{Fe}_{2/3}-\text{BaTiO}_3$  composite as described in<sup>22</sup>). In particular the sign of  $\alpha_{ME}$  is inverted, although both samples were electrically poled in the same direction. This can be explained taking into account the different magnetostrictions of  $\text{Co}_{1/3}\text{Fe}_{2/3}$  and  $\text{CoFe}_2\text{O}_4$ . While  $\text{Co}_{1/3}\text{Fe}_{2/3}$  has a positive magnetostriction,<sup>19</sup>  $\lambda$  of  $\text{CoFe}_2\text{O}_4$  is negative.<sup>32</sup>

From Figure 5 it can be seen that the ME coefficient slightly increases with frequency up to 500 Hz. At higher frequencies only minimal changes were observed. Again,

the different behavior of the sample with  $x=0.4$  becomes evident. While the other two samples exhibit negative ME voltages at positive fields, positive maximum values were observed for this composition.

## 4 | CONCLUSIONS

We report the first magnetoelectric investigations on particulate composites of  $\text{BaTiO}_3$  in combination with a Co/Fe alloy.  $(\text{Co}_{1/3}\text{Fe}_{2/3})_x-(\text{BaTiO}_3)_{(1-x)}$  samples with  $x=0.2$ , 0.4 and 0.6 were prepared by sintering in a reducing atmosphere. The samples possess a uniform  $\text{BaTiO}_3$  matrix with embedded  $\text{Co}_{1/3}\text{Fe}_{2/3}$  particles. In contrast to cobalt ferrite-barium titanate composites, the dielectric properties are comparable to the ones of pure  $\text{BaTiO}_3$ . Soft ferromagnetic hystereses with large saturation magnetizations of  $2.5 \mu_B/\text{atom}$  were observed for all three compositions. Magnetoelectric investigations of the  $\text{Co}_{1/3}\text{Fe}_{2/3}-\text{BaTiO}_3$  system revealed surprising  $H_{DC}$  dependencies. Compared to  $\text{CoFe}_2\text{O}_4-\text{BaTiO}_3$  composites, an inversed sign and a completely different course of  $\alpha_{ME}$  was observed. In addition, significant deviations in the magnetoelectric behavior for the three  $\text{Co}_{1/3}\text{Fe}_{2/3}-\text{BaTiO}_3$  ratios were found. For  $x=0.2$  and 0.6 negative maximum values of  $\alpha_{ME}$  occur at positive  $H_{DC}$  but both the values of  $\alpha_{ME(\max)}$  and of the corresponding magnetic fields are distinctively different. Even more surprising is the ME behavior of the intermediate composition  $0.4\text{Co}_{1/3}\text{Fe}_{2/3}-0.6\text{BaTiO}_3$ . For this sample a broad ME-hysteresis between  $+5$  and  $-5$  kOe was found and shows an unusual change in sign from a negative maximum at  $H_{DC}\approx 2.5$  kOe to a positive one at 7.5 kOe.

In summary this paper describes a new synthesis route to magnetoelectric metal/alloy- $\text{BaTiO}_3$  composites with 0-3 connectivity and the first ME measurements of this system. The unique behavior of the samples opens the door to a completely uninvestigated field of new composites with fascinating magnetoelectric properties.

## ACKNOWLEDGMENTS

Financial support by the German Research Foundation within the Collaborative Research Centre SFB 762, Functionality of Oxide Interfaces, is gratefully acknowledged.

## REFERENCES

- Schmid H. Multi-ferroic magnetoelectrics. *Ferroelectrics*. 1994;162:317-338.
- Spaldin NA, Fiebig M. The renaissance of magnetoelectric multiferroics. *Science*. 2005;309:391-392.
- Zhai J, Xing Z, Dong S, Li J, Viehland D. Magnetoelectric laminate composites: an overview. *J Am Chem Soc*. 2008;91:351-358.

4. Srinivasan G. Magnetolectric composites. *Annu Rev Mater Res*. 2010;40:153–178.
5. Shen HQ, Wang YG, Xie D, Cheng JH. Magnetolectric effect in FeCo/PMN-PT/FeCo trilayers prepared by electroless deposition of FeCo on PMN-PT crystals with various orientations. *J Alloys Compd*. 2014;610:11–14.
6. Xie D, Wang YG, Cheng JH. Zero-biased and resonant magneto-electric effect in magnetostrictive/piezoelectric multilayered composites. *J Mater Sci: Mater Electron*. 2015;26:3545–3549.
7. Filippov DA, Laletin VM, Firsova TO. Nonlinear magnetolectric effect in composite multiferroics. *Phys Solid State*. 2014;56:980–984.
8. Okazaki T, Mikami K, Furuya Y, Kishi Y, Yajima Z, Kubota T. Magnetic properties of thin-film Fe–Pd alloy and magnetolectric coupling in Fe–Pd/Ag/PZT/Ag/Fe–Pd laminate composites. *J Alloys Compd*. 2013;577S:S300–S304.
9. Nair SS, Pookat G, Saravanan V, Anantharaman MR. Lead free heterogeneous multilayers with giant magneto electric coupling for microelectronics/microelectromechanical systems applications. *J Appl Phys*. 2013;114:064309.
10. Park JH, Jang HM, Kim HS, Park CG, Lee SG. Strain-mediated magnetolectric coupling in BaTiO<sub>3</sub>-Co nanocomposite thin films. *Appl Phys Lett*. 2008;92:062908.
11. Gojdka B, Hrkac V, Xiong J, et al. A critical evaluation of the 0-3 approach for magnetolectric nanocomposites with metallic nanoparticles. *J Appl Phys*. 2012;112:044303.
12. Hyuga H, Hayashi Y, Sekino T, Niihara K. Fabrication process and electrical properties of BaTiO<sub>3</sub>/Ni nanocomposites. *Nanostruct Mater*. 1997;9:547–550.
13. Hwang HJ, Toriyama M, Sekino T, Niihara K. In-situ fabrication of ceramic/metal nanocomposites by reduction reaction in barium titanate-metal oxide systems. *J Eur Ceram Soc*. 1998;18:2193–2199.
14. Pecharrómán C, Esteban-Betegón F, Bartolomé JF, López-Esteban S, Moya JS. New percolative BaTiO<sub>3</sub>-Ni composites with a high and frequency-independent dielectric constant ( $\epsilon_r \approx 80000$ ). *Adv Mater*. 2001;13:1541–1544.
15. Huang Y-C, Chen S-S, Tuan W-H. Process window of BaTiO<sub>3</sub>-Ni ferroelectric-ferromagnetic composites. *J Am Ceram Soc*. 2007;90:1438–1443.
16. Yoon S, Pithan C, Waser R, et al. Electronic conduction mechanisms in BaTiO<sub>3</sub>-Ni composites with ultrafine microstructure obtained by spark plasma sintering. *J Am Ceram Soc*. 2010;93:4075–4080.
17. Yoon S, Dornseiffer J, Schneller T, et al. Percolative BaTiO<sub>3</sub>-Ni composite nanopowders from alkoxide-mediated synthesis. *J Eur Ceram Soc*. 2010;30:561–567.
18. Sánchez-Jiménez PE, Pérez-Maqueda LA, Diáñez MJ, Perejón A, Criado JM. Mechanochemical preparation of BaTiO<sub>3</sub>-Ni nanocomposites with high dielectric constant. *Compos Struct*. 2010;92:2236–2240.
19. Williams SR. The joule magnetostrictive effect in a group of cobalt-iron alloys. *Rev Sci Instrum*. 1932;3:675–683.
20. Bardos DI. Mean magnetic moments in bcc Fe–Co alloys. *J Appl Phys*. 1969;40:1371–1372.
21. Felser C, Fecher GH, Balke B. Spintronik: eine Herausforderung für Materialwissenschaften und Festkörperchemie. *Angew Chem*. 2007;119:680–713.
22. Walther T, Straube U, Köferstein R, Ebbinghaus SG. Hysteretic magnetolectric behavior of CoFe<sub>2</sub>O<sub>4</sub>-BaTiO<sub>3</sub> composites prepared by reductive sintering and reoxidation. *J Mater Chem C*. 2016;4:4792–4799.
23. Marks GW, Monson LA. Effect of certain group IV oxides on dielectric constant and dissipation factor of barium titanate. *Ind Eng Chem*. 1955;47:1611–1620.
24. Efros AL, Shklovskii BI. Critical behaviour of conductivity and dielectric constant near the metal-non-metal transition threshold. *Phys Status Solidi B*. 1976;76:475–485.
25. Mitoseriu L, Buscaglia V. Intrinsic/extrinsic interplay contributions to the functional properties of ferroelectric-magnetic composites. *Phase Transitions*. 2006;79:1095–1121.
26. Gupta A, Chatterjee R. Dielectric and magnetolectric properties of BaTiO<sub>3</sub>-Co<sub>0.6</sub>Zn<sub>0.4</sub>Fe<sub>1.7</sub>Mn<sub>0.3</sub>O<sub>4</sub> composite. *J Eur Ceram Soc*. 2013;33:1017–1022.
27. Köferstein R, Ebbinghaus SG. BaGeO<sub>3</sub> as sintering additive for BaTiO<sub>3</sub>-MgFe<sub>2</sub>O<sub>4</sub> composite ceramics. *RSC Adv*. 2015;5:71491–71499.
28. Ghosh S, Sanyal B, Chaudhuri CB, Mookerjee A. Electronic structure and magnetism of disordered bcc Fe alloys. *Eur Phys J B*. 2001;23:455–461.
29. Ohnuma I, Enoki H, Ikeda O, et al. Phase equilibria in the Fe–Co binary system. *Acta Mater*. 2002;50:379–393.
30. Kuhrt C, Schultz L. Formation and magnetic properties of nanocrystalline mechanically alloyed Fe-Co and Fe-Ni. *J Appl Phys*. 1993;73:6588–6590.
31. Yu RH, Basu S, Ren L, et al. High temperature soft magnetic materials: FeCo alloys and composites. *IEEE Trans Magn*. 2000;36:3388–3393.
32. Nlebedim IC, Snyder JE, Moses AJ, Jiles DC. Dependence of the magnetic and magnetoelastic properties of cobalt ferrite on processing parameters. *J Magn Magn Mater*. 2010;322:3938–3942.

## SUPPORTING INFORMATION

Additional Supporting Information may be found online in the supporting information tab for this article.

**How to cite this article:** Walther T, Köferstein R, Ebbinghaus SG. Novel magnetolectric composites of cobalt iron alloy and barium titanate. *J Am Ceram Soc*. 2017;100:1502–1507. doi:10.1111/jace.14744.

## List of publications

### Articles in peer reviewed journals

- 12 T. Walther, R. Köferstein, S.G. Ebbinghaus, Novel magnetoelectric composites of cobalt iron alloy and barium titanate, *J. Am. Ceram. Soc.* 100 (2017) 1502-1507. doi: 10.1111/jace.14744.
- 11 H. T. Langhammer, T. Müller, T. Walther, R. Böttcher, D. Hesse, E. Pippel, S.G. Ebbinghaus, Ferromagnetic properties of barium titanate ceramics doped with cobalt, iron and nickel, *J. Mater. Sci.* 51 (2016) 10429. doi: 10.1007/s10853-016-0263-3.
- 10 G. Seiffarth, M. Steimecke, T. Walther, M. Kühhirt, S. Rümmler, M. Bron, Mixed transition metal oxide supported on nitrogen doped carbon nanotubes – a simple bifunctional electrocatalyst studied with scanning electrochemical microscopy, *Electroanalysis* 28 (2016) 2335-2345. doi: 10.1002/elan.201600254.
- 9 T. Walther, U. Straube, R. Köferstein, S.G. Ebbinghaus, Hysteretic magnetoelectric behavior of  $\text{CoFe}_2\text{O}_4\text{-BaTiO}_3$  composites prepared by reductive sintering and reoxidation, *J. Mater. Chem. C.* 4 (2016) 4792–4799. doi: 10.1039/C6TC00995F.
- 8 T. Walther, N. Quandt, R. Köferstein, R. Roth, M. Steimecke, S.G. Ebbinghaus,  $\text{BaTiO}_3\text{-CoFe}_2\text{O}_4\text{-BaTiO}_3$  trilayer composite thin films prepared by chemical solution deposition, *J. Eur. Ceram. Soc.* 36 (2016) 559–565. doi: 10.1016/j.jeurceramsoc.2015.10.009.
- 7 G. Ludwig, T. Ruffer, A. Hoppe, T. Walther, H. Lang, S.G. Ebbinghaus, D. Steinborn, Lithiated sulfoxides:  $\alpha$ -sulfinyl functionalized carbanions, *Dalton Trans.* 44 (2015) 5323–5330. doi: 10.1039/C4DT02238F.
- 6 H.T. Langhammer, R. Böttcher, T. Müller, T. Walther, S.G. Ebbinghaus, Defect properties of cobalt-doped hexagonal barium titanate ceramics, *J. Phys.: Condens. Matter.* 27 (2015) 295901. doi: 10.1088/0953-8984/27/29/295901.
- 5 R. Köferstein, T. Walther, D. Hesse, S.G. Ebbinghaus, Fine-grained  $\text{BaTiO}_3\text{-MgFe}_2\text{O}_4$  composites prepared by a Pechini-like process, *J. Alloys Compd.* 638 (2015) 141–147. doi: 10.1016/j.jallcom.2015.03.082.



- 4 R. Köferstein, T. Walther, D. Hesse, S.G. Ebbinghaus, Crystallite-growth, phase transition, magnetic properties, and sintering behaviour of nano-CuFe<sub>2</sub>O<sub>4</sub> powders prepared by a combustion-like process, *J. Solid State Chem.* 213 (2014) 57–64. doi: 10.1016/j.jssc.2014.02.010.
- 3 S. Haffer, C. Lüder, T. Walther, R. Köferstein, S.G. Ebbinghaus, M. Tiemann, A synthesis concept for a nanostructured CoFe<sub>2</sub>O<sub>4</sub>/BaTiO<sub>3</sub> composite: Towards multiferroics, *Microporous Mesoporous Mater.* 196 (2014) 300–304. doi: 10.1016/j.micromeso.2014.05.023.
- 2 R. Köferstein, T. Walther, D. Hesse, S.G. Ebbinghaus, Preparation and characterization of nanosized magnesium ferrite powders by a starch-gel process and corresponding ceramics, *J. Mater. Sci.* 48 (2013) 6509–6518. doi: 10.1007/s10853-013-7447-x.
- 1 S. Haffer, T. Walther, R. Köferstein, S.G. Ebbinghaus, M. Tiemann, Nanostructure-Related Magnetic Properties of Various Mesoporous Cobalt Oxide and Cobalt Ferrite Spinel Phases, *J. Phys. Chem. C.* 117 (2013) 24471–24478. doi: 10.1021/jp409058t.

## Reports

- 9 S.G. Ebbinghaus, N. Quandt, T. Walther, Spin coating of multiferroic composite thin films, 18. Conference of the GDCh Division of Solid State Chemistry and Materials Research, Innsbruck (20.09.2016).
- 8 S. G. Ebbinghaus, R. Köferstein, N. Quandt, T. Walther, Solution-processed thin films an nanostructured multiferroic BaTiO<sub>3</sub>/CoFe<sub>2</sub>O<sub>4</sub> composites, European Materials Research Society spring meeting, Lille (03.06.2016).
- 7 G. Seiffarth, M. Steimecke, M. Kühhirt, T. Walther, M. Bron, Ni<sub>x</sub>Co<sub>y</sub>Fe<sub>2</sub>O<sub>4</sub> on carbon supports as bifunctional electrocatalysts an active material for both oxygen evolution and oxygen reduction reaction, 18<sup>th</sup> topical meeting of the International Society of Electrochemistry, Gwangju (11.03.2016).
- 6 H. T. Langhammer, T. Müller, T. Walther, R. Böttcher, S. G. Ebbinghaus, Cobalt doped hexagonal BaTiO<sub>3</sub> ceramics, Electroceramics XIV Conference, Bucharest (18.06.2014).

- 5 T. Walther, N. Quandt, R. Köferstein, S. G. Ebbinghaus, Multiferroische  $\text{CoFe}_2\text{O}_4$  /  $\text{BaTiO}_3$  Komposite, 11. Mitteldeutsches Anorganiker Nachwuchssymposium, Dresden (19.09.2013).
- 4 S. G. Ebbinghaus, D. Hesse, R. Köferstein, T. Walther, N. Quandt, Multiferroische 0-3, 2-2 und 1-3 Komposite, SFB 762 Klausurtagung, Grimma (27.06.2013).
- 3 S. Haffer, C. Lüder, M. Tiemann, T. Walther, S.G. Ebbinghaus, Mesoporous Cobalt spinels with structure-related magnetic properties, 8<sup>th</sup> international mesostructured materials symposium, Hyogo (21.03.2013).
- 2 S. Haffer, C. Lüder, R. Köferstein, T. Walther, S. G. Ebbinghaus, Mesoporous cobalt spinels: synthesis by nanocasting and magnetic properties, 25. Deutsche Zeolith-Tagung-Jubiläumstagung, Hamburg (06.03.2013).
- 1 S. G. Ebbinghaus, R. Köferstein, T. Walther, N. Quandt, S. Haffer, M. Tiemann, Multiferroic composites with different dimensionality, 16. Conference of the GDCh Division of Solid State Chemistry and Materials Research, Darmstadt (17.09.2012).

### Posters

- 3 T. Walther, R. Köferstein, N. Quandt, M. Breitenbach, S. Ebbinghaus, Multiferroic 0-3, 2-2 and 1-3 Composites, SFB 762 International Workshop 2014, Irsee (10.–14.03.2014).
- 2 T. Walther, R. Köferstein, N. Quandt, S. Ebbinghaus, Multiferroic 0-3 and 2-2 Composites, 6<sup>th</sup> European School on Multiferroics, Wittenberg (22.–26.07.2013).
- 1 S. Haffer, C. Lüder, S. Ebbinghaus, R. Köferstein, T. Walther, M. Tiemann, Porous Metal Oxides and Composites with Ferroic Properties, 16. Conference of the GDCh Division of Solid State Chemistry and Materials Research, Darmstadt (17.–19.09.2012). doi:10.1002/zaac.201204022.

## **Danksagung**

An dieser Stelle möchte ich besonders Herrn Prof. Dr. Stefan Ebbinghaus meinen tiefsten Dank aussprechen.

Danke dafür, dass Sie mir die Möglichkeit gaben in Ihrer Arbeitsgruppe so viele Jahre zu arbeiten, zu forschen und Lehre zu betreiben. Danke dafür, dass ich große Freiheit in der Gestaltung meiner Forschung und der Kooperationen mit verschiedensten anderen Wissenschaftlern hatte. Danke für Ihre Unterstützung in kritischen Phasen meiner Zeit als wissenschaftlicher Mitarbeiter bei Ihnen. Danke ebenso für Ihre Hilfe bei der Erstellung der Publikationen und der Dissertationsschrift.

Der gesamten Arbeitsgruppe Festkörperchemie danke ich für die schöne Zeit, gefüllt mit fachlichen und auch nicht so fachlichen Diskussionen und gegenseitiger Unterstützung.

Ich danke den Mitarbeitern der anderen Arbeitsgruppen an unserem Institut für viele wechselseitige geistige Anregungen und Entspannungen.

Ich danke meinen Eltern und meiner Familie dafür, dass sie mir die nötige Grundeinstellung mitgegeben haben um diese Sache anzufangen und zu Ende zu bringen.

Vielen Dank an alle meine Freunde. Ohne euch wäre ich nicht so weit gekommen!

## **Lebenslauf**

### **Persönliche Daten**

---

Name: Till Walther  
geboren: 23.02.1986 in Stendal  
Anschrift: 06122 Halle (Saale), Fuhneweg 9

### **Beruflicher Werdegang**

---

seit 09.2017 Assistent für Qualitätssicherung, Omnisal GmbH Wittenberg  
04.2012 – 01.2017 Wissenschaftlicher Mitarbeiter - Institut für Chemie,  
Anorganische Chemie, AG Prof. S. Ebbinghaus,  
Martin-Luther-Universität Halle-Wittenberg  
09.2005 – 05.2006 Zivildienstleistender - Kinderheim Julianenhof, Havelberg

### **Praktika**

---

01.2012 – 03.2012 Projektmitarbeiter Arbeitsgruppe Festkörperchemie,  
Prof. S. Ebbinghaus  
Institut für Chemie, Anorganische Chemie  
Martin-Luther-Universität Halle-Wittenberg

### **Studium und Weiterbildung**

---

04.2012 – 08.2017 Promotion zum Thema: Magnetoelectric composite ceramics of barium  
titanate and cobalt-iron compounds  
Martin-Luther-Universität Halle-Wittenberg  
10.2009 – 09.2011 Master of Science Chemie  
Martin-Luther-Universität Halle-Wittenberg  
Spezialisierung: Anorganische Chemie  
10.2006 – 09.2009 Bachelor of Science Chemie  
Martin-Luther-Universität Halle-Wittenberg

### **Schulbildung**

---

09.1992 – 07.2005 Allgemeine Hochschulreife - Pestalozzi-Gymnasium, Havelberg

Halle (Saale), den 25.06.18

## **Erklärung an Eides statt**

Hiermit erkläre ich, dass ich diese Arbeit selbständig und ohne fremde Hilfe verfasst habe. Es wurden keine anderen als die angegebenen Quellen und Hilfsmittel verwendet. Die inhaltlich oder wörtlich entnommenen Stellen der benutzten Werke wurden als solche kenntlich gemacht. Zusätzlich erkläre ich, dass ich noch keinen vergeblichen Promotionsversuch unternommen habe und dass die Dissertation weder in der gegenwärtigen noch in einer anderen Fassung einer anderen Fakultät vorgelegen hat.

Till Walther

Halle (Saale), den 25.06.18